

Precision mass measurements of
neutron-deficient strontium and
commissioning of an HPGe array for in-trap
decay spectroscopy at the TITAN EBIT

Zachary Hockenbery



Department of Physics
McGill University
Montréal, Québec, Canada

April, 2024

A thesis submitted to McGill University in partial fulfillment of the requirements of the degree of

Doctor of Philosophy

© Zachary Hockenbery, 2024

Abstract

Nuclear physics research at radioactive ion beam (RIB) facilities has greatly benefited from the introduction of techniques and devices used in atomic physics. Among these are ion traps which are now regularly used at RIB facilities worldwide as accelerator infrastructure and as precision measurement devices. The focus of this thesis centers on two different ion traps used as measurement devices for nuclear structure research: a multiple-reflection time-of-flight mass spectrometer (MR-ToF-MS) and an electron beam ion trap (EBIT). One part of this thesis reports new mass measurements of neutron-deficient strontium ions using the MR-ToF-MS at TRIUMF's Ion Traps for Atomic and Nuclear science (TITAN) facility. MR-ToF-MS devices provide an excellent balance of mass resolving power and background reduction to access exotic regions in the table of isotopes, which are otherwise difficult to access because of low production cross sections and overwhelming background contamination. With the new mass measurements, we extend the isobaric multiplet mass equation and resolve a staggering anomaly previously observed in the 2020 Atomic Mass Evaluation. We also study the impact that these new mass values have on the rapid proton capture pathway in Type I X-ray bursts using a single-zone model simulation. The second part of this thesis reports on progress towards using TITAN's EBIT to perform in-trap decay spectroscopy on radioactive highly charged ions (HCI). The EBIT has been retrofitted with a new decay spectroscopy

array and auxiliary equipment to perform the experiment. This includes an array of high purity germanium γ -ray detectors, a low-energy X-ray detector, a new liquid nitrogen autofill system, and the associated electronics for operating the detectors and acquiring data. The detector setup has been commissioned as a step towards proposed in-trap decay spectroscopy measurements.

Abrégé

La recherche en physique nucléaire dans les installations de faisceaux d'ions radioactifs (RIB) a grandement bénéficié de l'introduction de techniques et d'appareils utilisés en physique atomique. Parmi ceux-ci se trouvent les pièges à ions, désormais couramment utilisés dans les installations RIB du monde entier en tant qu'infrastructures d'accélération et dispositifs de mesure de précision. Cette thèse se concentre sur deux pièges à ions différents utilisés comme dispositifs de mesure pour la recherche sur la structure nucléaire : un spectromètre de masse à temps de vol à réflexions multiples (MR-ToF-MS) et un piège à ions par faisceaux d'électrons (EBIT). Une partie de cette thèse rend compte de nouvelles mesures des masses des ions de strontium déficients en neutrons en utilisant le MR-ToF-MS dans l'installation pour pièges à ions pour la science atomique et nucléaire de TRIUMF (TITAN). Les dispositifs MR-ToF-MS offrent un excellent compromis entre la puissance de résolution de masse et la réduction du bruit de fond pour accéder à des régions exotiques dans le tableau des isotopes, ce qui serait sinon difficile d'accès en raison de faibles sections efficaces de production et d'une contamination en bruit de fond prohibitive. Grâce aux nouvelles mesures de masse, nous étendons l'équation de masse de multiplet isobare et résolvons une anomalie stupéfiante précédemment observée dans l'évaluation de masses atomiques par l'AME en 2020. Nous étudions également l'impact que ces nouvelles valeurs de masse ont sur la voie de capture

rapide de protons dans les explosions de rayons X de type I en utilisant une simulation de modèle à zone unique. La deuxième partie de cette thèse rend compte des progrès réalisés dans l'utilisation de l'EBIT de TITAN pour effectuer une spectroscopie de désintégration en piège sur des ions radioactifs fortement chargés (HCI). L'EBIT a été réaménagé avec un nouvel ensemble de spectromètres de désintégration et un équipement auxiliaire pour réaliser l'expérience. Cela comprend un ensemble de détecteurs de rayons γ en germanium de haute pureté, un détecteur de rayons X à basse énergie, un nouveau système de remplissage automatique d'azote liquide et l'électronique nécessaire pour faire fonctionner les détecteurs et acquérir des données. La configuration du détecteur a été mise en service comme étape vers les mesures proposées en spectroscopie de désintégration en piège.

Acknowledgements

As I move on from my PhD, there are a great many people who supported me and to whom I would like to express my gratitude.

First, I would like to thank my McGill supervisor Thomas Brunner. Thank you for your guidance, mentorship, and support throughout the research process. While you were not always locally at TITAN, your past experience with the in-trap decay spectroscopy setup at TITAN served as important guidance to help us to move forward with the project. During thesis writing, your feedback and suggestions have been a key part to helping the thesis come together as a cohesive work. Thank you for taking a chance on an engineer who decided very late that he wanted to become a physicist.

Next I would like to thank my local TRIUMF supervisor Ania Kwiatkowski. A large step for me in this process was becoming a senior graduate student within the TITAN group and this would not have been possible without your encouragement, guidance and trust. Whether it was encouraging me to reach out to leading experts on a topic or to take ownership of a specific task within the group, you gave great feedback to any concerns or questions that I had. TITAN is a fantastic research group to be a part of and you have been instrumental in making it that way. One of the most difficult times during this work was navigating the myriad of uncertainties presented by the Covid-19 pandemic. Thank you to Thomas and

Ania for your compassion and flexibility during these times.

I would like to express my gratitude to the entire decay spectroscopy and EBIT team. This work was not possible without the students and post docs Jon Ringuette, John Ash, Stefan Paul, Fernando Maldonado, Jaime Cardona, Rane Simpson, Yilin Wang, Kilian Dietrich and Akshay Ramasubramanian, as well as the principle investigators supporting the decay spectroscopy program, Iris Dillmann, Kyle Leach, Thomas Brunner, Annika Lennarz, and Corina Andreoiu.

Thank you to the entire MR-ToF-MS team and the TITAN members who were present during the mass measurement beamtime performed in this thesis. During the mass analysis, I am grateful to the guidance and suggestions given by Tobias Murboeck, Stefan Paul, Pascal Reiter, Ali Mollaebrahimi, Andrew Jacobs, and Erich Leistenschneider. Many thanks to Jason Holt and Baishan Hu who ran VS-IMSRG calculations and to Hendrik Schatz who ran X-ray burst simulations.

Thank you to the mechanical technician assigned to TITAN, Mel Good. Your designs are robust, safe, practical, and necessary to keep the high-performing TITAN experimental setup going strong. Thank you Shaun Georges for always being available to answer questions about liquid nitrogen and offering tools or materials to help us out in a pinch. Thank you Chris Pearson, Ben Smith, and Gelo Remon for your support on the setting up the data acquisition and liquid nitrogen systems.

As I look back on my time with TITAN, I will greatly miss contributing beamtime shifts to the various experiments we performed. TITAN has a wealth of diversity not only in ion traps, but people as well, and beamtime experiments were the best opportunities to experience both. I will miss the enthusiasm of the students and post docs, the great conversations, and the general camaraderie of pushing through a night shift together.

I cannot thank enough my friends, family and loved ones who supported me through the ups and downs of this work. Thank you Kitsilano beach volleyball community for being a place for me to recharge, unwind, and enjoy some sunshine. Thank you Mom and Dad and Sister for always showing interest and excitement in the work that I do despite it being a bit arcane. Thank you Tara for being understanding and supportive throughout the different phases of this journey.

Statement of contributions

Science is hard, and without specific contributions from many people, this thesis work would not have been possible. This statement is meant to acknowledge the specific contributions that were made by individuals. All chapters in this thesis were written by myself. I tried to create as many of the figures as I could myself, but when this was not possible, the caption acknowledges from where or whom it was sourced. The mass measurements in Chapter 4 were performed by the TITAN collaboration, with each of us contributing daily 8-hour shifts for the duration of the experiment. The analysis of the data presented in Chapter 4 was performed by me. The emgfit software used for peak fitting was written by Stefan Paul. In Chapter 5, the impact of the data on the IMME and rp-process X-ray bursts is explored. The results reported in both Sections 5.1 and 5.2 were fuelled by discussions with both former and current TITANs including Tobias Murboeck, Stefan Paul, and Pascal Reiter. I performed the analysis of the data as well as the TALYS calculations of astrophysical reaction rates. The single-zone X-ray burst calculation was performed by Hendrik Schatz.

The majority of the work in Chapter 6 to procure the materials, write the software, and test and install the detectors was performed by Jon Ringuette and myself. Design of the detector mounting system and calibration stands was performed by the TITAN mechanical technician, Mel Good. For much of the data acquisition and electronics, we were helped by

TRIUMF staff Chris Pearson, Ben Smith, and Gelo Remon. For tests that required the EBIT in Section 6.6, this was a collaborative effort between the EBIT and Decay Spectroscopy teams. Scanning of the electron beam energy for argon DR lines was performed by John Ash and Stefan Paul. The two experiments that are currently envisioned for the in-trap decay spectroscopy setup are S2175 (Nuclear two-photon emission unveiled through suppression of first-order decay processes) and S2128 (Controlled stimulation of nuclear excitation via electron capture in the TITAN EBIT). During this thesis, I drafted, submitted, and successfully defended S2175 at TRIUMF's Nuclear Physics Experimental Evaluation Committee (NP-EEC). Both proposals have been granted 8 high priority beamtime shifts (8 hours per shift). These proposals are available through TRIUMF's experiments database¹.

¹<https://mis.triumf.ca/science/experiment/list.jsf>

Contents

1	Mass matters: probing nuclear structure with precise measurements	1
1.1	Introduction	2
1.2	The goal of this thesis work	9
2	Physics review and fundamentals of time-of-flight mass spectrometry	11
2.1	Isospin symmetry breaking in nuclei	12
2.1.1	Fundamentals of isospin	12
2.1.2	The isobaric multiplet mass equation	17
2.1.3	Mass measurements to extend the IMME	21
2.1.4	Alternatives to the IMME	27
2.2	The rp-process in Type I X-ray bursts	28
2.2.1	Type I X-ray bursts	28
2.2.2	Observational features of thermonuclear X-ray bursts	30
2.2.3	X-ray burst modelling	32
2.2.4	Nuclear masses for burst modelling of the rp-process	34
2.2.5	Uncertainties in the vicinity of the ^{72}Kr waiting point	38
2.3	Time-of-flight mass spectrometry	39

2.3.1	Basics of time of flight mass spectrometry	39
2.3.2	Multiple reflection time of flight mass spectrometry	46
3	Overview of the experimental facilities	51
3.1	The TRIUMF cyclotron and the ISAC facility	52
3.2	The TITAN facility	55
3.2.1	Radiofrequency quadrupole cooler-buncher	57
3.3	The multiple-reflection time-of-flight mass spectrometer	58
3.3.1	Ion transport system	61
3.3.2	Mass analyzer	63
3.3.3	MR-ToF-MS Operation	63
4	Mass measurements of neutron-deficient strontium and lanthanides	67
4.1	Introduction	68
4.2	Measurement procedure	69
4.3	Analysis	72
4.3.1	Time-resolved mass calibration	72
4.3.2	Peak shape models for curve fitting	75
4.3.3	Calculation of final mass values	77
4.3.4	Evaluation of measurement uncertainties	78
4.4	Final values and discussion	83
4.4.1	Strontium	86
4.4.2	Lanthanides	90
5	Neutron-deficient Sr masses for nuclear structure and astrophysics	98
5.1	Scientific impact on the isobaric multiplet mass equation	99

5.1.1	The $T = 1/2$ doublets	100
5.1.2	The $T = 1$ triplets	102
5.2	Scientific Impact on the rp-process and Type-I X-ray Bursts	106
6	Installing and commissioning a new HPGe array at the TITAN EBIT	109
6.1	Decay spectroscopy with radioactive highly charged ions	110
6.2	Introduction to the Electron Beam Ion Trap (EBIT)	112
6.3	The TITAN EBIT	114
6.3.1	Electron gun and collector	115
6.3.2	Ion trap	118
6.3.3	EBIT Operation	122
6.4	In-trap decay spectroscopy at the EBIT	124
6.5	The new HPGe detector array for in-trap decay spectroscopy	126
6.5.1	HPGe γ -ray detectors	128
6.5.2	HPGe X-ray detectors	129
6.5.3	Mounting the detectors onto the EBIT	130
6.5.4	Liquid nitrogen filling system	133
6.5.5	Electronics	141
6.5.6	Data Acquisition	145
6.6	Detector tests	148
6.6.1	Detector resolution	148
6.6.2	Ambient background in the EBIT	152
6.6.3	Studying the space charge of the electron beam	152
7	Conclusion	159

List of Figures

2.1	A comparison of the low-lying level structure in ^{23}Na and ^{23}Mg mirror pairs	15
2.2	The doublet b coefficients extracted from the AME 2020.	23
2.3	The triplet b coefficients extracted from the AME 2020.	25
2.4	The triplet c coefficients extracted from the AME 2020.	26
2.5	The light curve of the X-ray burster GS 1826-24 observed by the Swift X-ray telescope.	31
2.6	Simulated X-ray burst reaction flow.	35
2.7	An illustration of a simple linear time-of-flight mass spectrometer.	42
2.8	An illustration of an electrostatic ion mirror.	45
2.9	An illustration of the “closed path” design for a time-of-flight mass analyzer	48
3.1	An illustration of the target and ion source geometry using the hot cavity surface ionization source.	54
3.2	A schematic overview of the ISAC-I and ISAC-II facilities.	55
3.3	An illustration of the TITAN facility showing the four ion traps.	57
3.4	An illustration of TITANs RFQ cooler-buncher	59
3.5	The important components of TITANs MR-ToF-MS	62
3.6	The dynamic time-focus shift method used by TITAN MR-ToF-MS	64

3.7	The separate stages of MR-ToF-MS operation.	66
4.1	The mass-selective re-trapping technique demonstrated at $A/Q = 76$	71
4.2	Resonant laser ionization of ^{74}Sr	73
4.3	Drift correction using the time resolved calibration (TRC) procedure	74
4.4	Mass deviation of determined strontium masses against the AME 2020	85
4.5	Mass spectrum at $A/Q = 76$	87
4.6	Mass spectrum at $A/Q = 75$	88
4.7	Mass spectrum at $A/Q = 74$	89
4.8	Lanthanide mass spectrum at $A/Q = 72.5$	93
4.9	Lanthanide mass spectrum at $A/Q = 73$	94
4.10	Lanthanide mass spectrum at $A/Q = 74$	95
5.1	The staggering behaviour of the doublet b coefficients with the new TITAN mass data included.	101
5.2	A plot of the triplet b coefficients using b_{dev}	104
5.3	The c coefficients extracted from $A = 4n + 2$ triplets.	105
5.4	An illustration of the rp-process path showing the masses measured during this work.	107
6.1	How an EBIB uses electron impact ionization to create HCl.	113
6.2	A sectioned view of the TITAN EBIT.	115
6.3	A sectioned view of the TITAN EBIT electron gun.	117
6.4	A sectioned view of the EBIT collector.	118
6.5	A sectioned view of the EBIT drift tube (DT) assembly.	120

6.6	A cross-section of the EBIT ion trap showing the access that photon detectors have to the trap center.	121
6.7	An illustration of the axial electrostatic potential during EBIT operation. . .	123
6.8	An illustration of the EBIT multiple injection scheme.	126
6.9	A diagram showing the basic signal processing chain of TITANs HPGe detectors.	128
6.10	TITANs γ -ray detectors.	129
6.11	TITANs X-ray detectors.	131
6.12	The HPGe detector array mounted onto the EBIT.	132
6.13	The detector stands for γ -ray detector maintenance and calibrations.	134
6.14	An illustration of the components of the liquid nitrogen autofill system. . . .	135
6.15	A comparison between the old (bottom) and new (top) LN2 injectors used with TITAN's γ -ray detectors.	139
6.16	Temperature sensitive LED's for the LN2 system.	140
6.17	The EPICS LN2 system control software.	142
6.18	The electronics used to power and operate the detectors, and digitize the signals.	143
6.19	Web interfaces for controlling the TITAN Decay Spectroscopy digitizers. . .	144
6.20	An illustration showing the setup of the DAQ system for decay spectroscopy at the EBIT.	146
6.21	The Spectrum Viewer for viewing online data is shown.	147
6.22	γ -ray detector calibrations.	149
6.23	A calibration spectrum of ^{133}Ba using the X-ray detector.	151
6.24	A 2D histogram of a 24 hour background spectrum recorded with the X-ray detector.	153

6.25 A schematic of KLL dielectronic recombination.	155
6.26 KLL DR lines in highly charged argon.	156
6.27 The time dependence of argon DR lines as the EBIT trap fills up with argon.	157

List of Tables

1.1	Relative mass precision required for different nuclear physics motivations.	6
2.1	A table showing the experimental nucleon-nucleon scattering lengths.	12
4.1	The uncertainty budget of the strontium mass measurements.	84
4.2	The uncertainty budget of the lanthanide mass measurements.	84
4.3	Summary of strontium masses determined as a part of this thesis	85
4.4	Lanthanide masses determined as a part of this thesis.	91
6.1	The photopeak resolution of detectors N50RB and N1370B at the two ^{60}Co photopeak energies measured with the detectors in a test stand. When installed on the EBIT, the resolution degrades due to vibrations. Uncertainties are shown as one standard deviation in parentheses.	150
6.2	The photopeak resolution of our GUL0110P determined with a ^{133}Ba calibration source. Uncertainties are shown as one standard deviation in parentheses.	152

Chapter 1

**Mass matters: probing nuclear
structure with precise measurements**

1.1 Introduction

To take part in a physics doctorate program is to join a global scientific endeavour to disentangle the mysteries of the universe, expand the boundaries of human knowledge, and contribute valuable insights that will shape the future of technology. A shining example of the physics community's success in this endeavour is the theory of quantum electrodynamics (QED) which describes the electromagnetic force through a quantum field theory. Before QED, our understanding of electromagnetism was based in Maxwell's equations which struggled to explain phenomena observed at the atomic scale. Perhaps the most important experiment that helped to secure the success of QED is that of the Lamb shift, a small energy shift in the spectral lines of hydrogen $^2S_{1/2}$ and $^2P_{1/2}$ orbitals due to interaction of the orbital electron with small vacuum fluctuations in the electromagnetic field [1]. Today, modern precision experiments continuously validate QED predictions with remarkable accuracy [2, 3]. While QED has elegantly predicted the behaviour and properties of atoms and molecules, the story is starkly different when our gaze is turned towards the atomic nucleus and the force that binds it. The atomic nucleus was discovered over one century ago during Rutherford's famous gold foil experiment [4], but still today a comprehensive explanation of the nucleus in all of its forms has remained elusive to the physics community.

Our struggle to describe the nucleus is rooted in an inherent difficulty to fully characterize the nuclear force that binds the nucleons together to a separation distance of ~ 1 fm. The earliest model of the nuclear force was the Yukawa potential which explained the binding of the nucleons despite the presence of Coulomb repulsion between the protons [5]. Later models of the nuclear force used hierarchical models where different interaction regimes occur at different length scales of the interaction. For example, Taketani *et al.* used three

different regions to describe a long distance attraction via one-pion exchange (region I), an intermediate distance attraction via two-pion exchange (region II) and an a short distance repulsion (region III) parameterized by empirical data on nucleon-nucleon scattering [6]. However, since the discovery of the quark content of nucleons, the nuclear force is known as a residual interaction of the strong force between quarks. The strong force is considerably more complex than the Coulomb interaction and requires the non-linear, non-Abelian gauge quantum theory known as Quantum Chromodynamics (QCD) to describe. While QCD theory and the quark model have enjoyed much success [7, 8], QCD theory does not yet provide a way to derive the nuclear force. Recent advancements in modern effective field theories (EFT) like chiral perturbation theory have demonstrated much success in modelling low-energy two-nucleon (NN) and three-nucleon (3N) interactions [9].

Beyond the challenge of understanding the nature of the strong force is the challenge of capturing the complexity of the nucleus in our theoretical modelling. A basic comparison against the atomic orbital illustrates why this is: the electrons in the atomic orbital are bound to a central potential with the electromagnetic interaction while protons and neutrons are bound to each other through the strong force but also interact via electromagnetic forces. The term often used to describe this situation is that the nucleus is a “many-body system” which indicates that the particles in the system not only obey quantum mechanics but are also strongly interacting with each other. These coherent motions and interactions of the nucleons give rise to many emergent phenomena observed in the structure and properties of nuclei. In other words, the nuclear phenomena bear little resemblance to the underlying elementary laws of the individual particles and instead arise from the quantum many-body behaviour of the system. A key challenge of these systems is that phenomenological models with effective degrees of freedom are not always able to reproduce the emergent phenomena.

On the other hand, a system-level description which accounts for every nucleon-nucleon interaction is usually beyond the limits of available computing powers because the dimension of the quantum many-body system increases as $N!$ (N factorial), where N is the number of interacting particles.

In studying the atomic nucleus, it is particularly useful to identify how nuclear properties change as a function of the nucleon number A (isobars), the proton number Z (isotones) and the neutron number N (isotopes). However, as we already know, the addition of protons or neutrons to a stable nucleus generally creates nuclear states that are of finite stability and will radioactively decay back to stability. Therefore the production of radioactive and short-lived nuclei requires that experimental facilities utilize fast production and delivery methods and that experiments are able to be quickly performed. The methods for the production and delivery of radioactive nuclei were essentially pioneered in the 1950s and 60s with the advent of the isotope separation on-line (ISOL) technique [10] and the subsequent commissioning of ISOLDE at CERN [11]. Later in the 1980s, developments for the in-flight method of isotope production were made at Lawrence Berkley National Laboratory [12]. With these techniques, modern nuclear physics research has seen the commissioning of radioactive ion beam (RIB) facilities using both in-flight and on-line production methods worldwide [13]. Access to RIB increases the number of nuclei that can be studied from the ~ 300 stable nuclei up to over 3000 nuclei. Not only have these facilities opened the door to studying the variation of nuclear structure and properties along isobaric, isotonic and isotopic lines, they also give access to unique areas of the chart that are well suited to study specific nuclear phenomena. This includes regions where the rapid proton (rp) capture process powers astronomical X-ray bursts [14], regions where useful concepts like isospin symmetry can be exploited to study nuclear structure [15], and regions where the stable existence of nuclei falls off (proton and

neutron drip lines) [16].

A property of the nucleus which is the central focus of this thesis is the nuclear mass excess, which is determined from the difference between the experimentally measured mass of the nucleus and the mass of its constituent nucleons:

$$\text{ME}(N, Z) \equiv M_{\text{exp}}(N, Z) - (N + Z)m_{\text{u}}, \quad (1.1)$$

where m_{u} is the atomic mass unit. The mass excess is particularly sensitive to the underlying interactions between the nucleons and can provide unique structural information if measured with sufficient precision. In fact, the discovery of the nuclear magic numbers was enabled by $\sim 500 - 1000$ keV precision mass measurements which uncovered abnormalities in the general trend of nuclear mass excesses at specific proton and neutron numbers. The identification of these magic numbers eventually led to the development of the very successful nuclear shell model that we know today. Because the nucleon masses are well known, the mass excess is well constrained by mass measurements of the nucleus. Due to the high mass precision available with most modern mass spectrometers, mass spectrometry has emerged as a reliable tool to study nuclear structure, nuclear astrophysics, and even test fundamental physics symmetries [17]. Today, essentially every RIB facility in operation hosts an experimental setup dedicated to providing mass measurements of exotic radioactive nuclei.

Many types of mass spectrometers are used in nuclear physics research and each is specialized for different experimental purposes. For example, devices with low mass resolving power but quick measurement speeds are ideal for the purposes of isotope discovery, but not for resolving low-lying nuclear isomeric states. This thesis is particularly interested in providing empirical mass data in the neutron-deficient $A = 60 - 80$ region for the purposes of nuclear structure and nuclear astrophysics research. Table 1.1 gives the

Physics case	Required relative mass precision
Nuclear structure	$\sim 1 \times 10^{-7}$
Nuclear astrophysics	$\sim 1 \times 10^{-7/-8}$
Tests of fundamental symmetries and neutrino physics	$\sim 1 \times 10^{-8/-9}$

Table 1.1: The relative mass precision required for different nuclear physics motivations. Table reproduced from [17].

general relative mass precision $\Delta m/m$ that is required for these physics cases. In the case of nuclear structure, the required relative mass precision is largely determined by the current mass precision of measured nuclei and the scale at which structural deviations are expected to be uncovered. In the case of nuclear astrophysics, the required relative mass precision is determined such that empirical mass data would not be a leading uncertainty contributor in computational astrophysical models.

The neutron-deficient medium mass region between $A = 60 - 80$ is marked by an intersection of the proton drip line with the $N = Z$ line. This is largely due to Coulomb repulsion between protons preventing the formation of bound nuclear states with large proton excess. At ISOL facilities the production and study of these isotopes is hampered by low cross-sections for isotope production as well as significant background contamination from nuclear isobars and doubly-charged heavy lanthanides. Therefore, beyond just the mass resolving power, we must consider our mass spectrometer's ability to tolerate in-beam contamination and perform mass measurements quickly.

For the case of nuclear structure, our interest lies in studying the effects of isospin symmetry breaking at the scale of the nuclear many-body system. While isospin symmetry was devised almost one century ago by Heisenberg to explain the similarities between protons and neutrons [18], this symmetry is also manifest on the nuclear scale between

nuclear isobars. A specific phenomenon related to isospin symmetry in nuclei is the Nolen-Schiffer anomaly [19], which arose from studying the difference in binding energies between two members of an isobaric multiplet. An isobaric multiplet is formed from nuclear configurations that lie along an isobaric line¹, have the same total isospin T , and spin-parity J^π , but different values of the isospin projection $T_z = (N - Z)/2$. Essentially, the difference in binding energies between these states should be accounted for by correcting for the difference in proton/neutron content between these states. This includes the Coulomb interaction between the protons and the proton-neutron mass difference, which are well-known violators of isospin symmetry. The anomalous behaviour arises because these corrections consistently underestimate the difference in binding energies [20–22]. Later work revealed that better estimates could be produced by considering contributions from an isospin non-conserving interaction of nuclear origin [23]. It is therefore important to extend the set of experimentally evaluated isobaric multiplets with nuclear mass data to better understand the sources of isospin symmetry breaking in nuclei [23, 24]. The specific vehicle with which we aim to explore nuclear structure is with an equation known as the isobaric multiplet mass equation (IMME), which is derived and discussed in Chapter 2.

The second case for mass measurements in this region is to study the rp-process pathway in Type I X-ray bursts. The rp-process is one of several reaction sequences that occur in hot, dense astronomical environments and have been studied as important sources of nucleosynthesis [14, 25]. The primary site where the rp-process has been identified to exist is in Type I X-ray bursts which are periodic thermonuclear explosions that occur on the surfaces of accreting neutron stars [26]. In our galaxy alone there are over one hundred identified

¹i.e. have the same atomic mass A

Type I X-ray bursters [27] which are being observed by new generation space-based telescopes such as NuSTAR (Nuclear Spectroscopic Telescope Array) [28], AstroSat [29] and NICER (Neutron star Interior Composition Explorer) [30]. The systems being observed are binary star systems composed of a neutron star and a light companion star which donates hydrogen- and helium-rich matter. The burst events begin as the hot and dense hydrogen-helium fuel mixture ignites with trace amounts of carbon, nitrogen and oxygen isotopes and energy is generated via the HCNO cycle [25]. Eventually the right temperature and density conditions can push the reaction flow towards the proton-rich region where the rp-process begins as a series of proton captures and β^+ decays which climb the nuclear chart towards heavier masses. While it is currently unclear whether rp-process X-ray bursts provide a source of galactic nucleosynthesis [31, 32], their study is being exploited to probe the fundamental properties of neutron stars and the accretion and ignition mechanisms in binary systems [33–35].

Due to the exotic and often short-lived nature of the nuclei involved in the rp-process and X-ray bursts, many of the reactions cannot be directly observed using terrestrial experiments. Therefore the most effective method to better understand this phenomenon is comparisons between numerical models and X-ray burst light curves [36]. While the burst events occur on extreme scales that require incredible spatiotemporal resolution to accurately model, numerical models with reduced degrees of freedom have taught us a great deal about rp-process involvement in X-ray bursts. For example, single-zone models mark the natural endpoint of the rp-process as the region of α -emitting nuclei near $A = 104$ [37]. Because of this we also know that the rp-process can involve a large reaction network of nuclei ranging from several hundred isotopes up to a few thousand. Other simulations have revealed that specific isotopes act as “waiting points” and delay the rp-process reaction flow to have a strong effect on the shape of the observable light curve [25, 38, 39].

Nuclear masses have a direct impact on X-ray burst models because proton capture rates depend exponentially on the mass difference (also known as the Q-value) between the reacting nuclei [25]. This means that the mass precision of all nuclei along the rp-process reaction path can have an effect on the accuracy of model predictions. Through systematic studies of the sensitivity of these models to mass and reaction input values, it has been shown that mass precision is especially important near rp-process waiting points [40, 41]. While much progress has been made to fill the experimental nuclear database, some mass and structure data for medium and high mass neutron-deficient nuclei is not measured or is not known with a sufficient precision (~ 10 keV) [41–43].

1.2 The goal of this thesis work

This thesis is divided into two main topics which were both performed at TRIUMF’s Ion Traps for Atomic and Nuclear science (TITAN) facility [44, 45] in Vancouver, British Columbia, Canada. The first part of this thesis consists of experiment S1615LOI to measure the masses of neutron-deficient $^{74-76}\text{Sr}$ and heavy lanthanides ^{145}Tb , ^{146}Tb , and ^{148}Ho using TITAN’s multiple-reflection time-of-flight mass spectrometer (MR-ToF-MS) [46, 47]. TITAN’s MR-ToF-MS provides an excellent balance of mass resolving power, quick measurement cycles, and background reduction to access this region of the nuclear chart. The data analysis and final results are provided as well as a study into the impact these new masses have for the two science cases presented earlier.

The second part of this thesis involves the assembly and commissioning of a new high-purity germanium (HPGe) detector array with auxiliary equipment onto TITAN’s Electron Beam Ion Trap (EBIT). The HPGe array is destined to perform nuclear decay spectroscopy

experiments with highly charged radioactive ions using the EBIT's unique charge evolving capabilities and access to TRIUMF's ISAC facility. Two experiments are currently envisioned for the setup: S2175 (Nuclear two-photon emission unveiled through suppression of first-order decay processes) and S2128 (Controlled stimulation of nuclear excitation via electron capture in the TITAN EBIT). During this thesis, I drafted, submitted, and successfully defended S2175 at TRIUMF's Nuclear Physics Experimental Evaluation Committee (NP-EEC).

This thesis is organized as follows. Chapter 2 provides a review of the relevant physics and literature to understand the mass measurement and the impact it has for nuclear structure and nuclear astrophysics. Chapter 3 gives an overview of the experimental facilities required to perform the mass measurement. This includes the TRIUMF-ISAC facility for RIB production and the TITAN ion trapping facility for the mass measurements. Chapter 4 presents the RIB experiment for precision mass measurements of $^{74-76}\text{Sr}$, ^{145}Tb , ^{146}Tb , and ^{148}Ho performed with the TITAN MR-ToF-MS. The data analysis as well as the final numbers are also presented in this chapter. Chapter 5 studies the impact that the strontium mass measurements have on the IMME and also explores their impact to the rp-process pathway in Type I X-ray burst using a single-zone model simulation. Chapter 6 covers the second main part of this thesis, which is the assembly and commissioning of the decay spectroscopy array at TITAN EBIT. This chapter introduces the EBIT and then describes the work that was performed to assemble the in-trap spectroscopy system onto the EBIT. We briefly look at some commissioning tests that are being performed as preparation towards the proposed experiments. Chapter 7 gives a final conclusion to this work and an outlook for future developments.

Chapter 2

Physics review and fundamentals of time-of-flight mass spectrometry

2.1 Isospin symmetry breaking in nuclei

2.1.1 Fundamentals of isospin

To understand how mass measurements can be used to study nuclear structure in this work, we need to review isospin in nuclei, introduce the Isobaric Multiplet Mass Equation (IMME), and review the current status of empirical data on the IMME.

The concept of isospin symmetry was first devised by Heisenberg in the early 1930s to explain the astonishing symmetry between protons and neutrons [18]. Protons and neutrons are both spin 1/2 particles, they are both constituents of the nucleus, and their mass ratio is very nearly unity¹. Furthermore, as shown in Table 2.1, scattering experiments to determine the distance scale of the strong nuclear force between these particles have shown that they are incredibly similar. The agreement between the proton-proton and neutron-neutron interactions is known as the charge symmetry of the nuclear force, while the agreement between the proton-neutron interaction and the average of the proton-proton and neutron-neutron interactions is known as the charge independence of the nuclear force.

Interaction	Scattering length [fm]
proton-proton	-17.3(4)
neutron-neutron	-18.9(4)
proton-neutron	-23.74(2)

Table 2.1: A table showing the experimental nucleon-nucleon scattering lengths. For the values reported here, the Coulomb component of the interaction is removed. Data from [15].

This prompted Heisenberg to suggest that protons and neutrons are different manifestations of the same fundamental entity, i.e. different states of the nucleon. The

¹As of 2021, the neutron-proton mass ratio is $m_n/m_p = 1.001\,378\,419\,31(49)$ [48].

isospin concept is quite successful because it provides a simple framework for understanding complex nuclear interactions. Today, most undergraduate physics textbooks will discuss that isospin is a broken symmetry. The primary source of isospin symmetry breaking is due to the different electrical charges that the proton and neutron carry. Symmetry breaking can also be seen by the difference in proton and neutron masses and the slight difference in nucleon-nucleon scattering lengths given in Table 2.1. However, just because it is a broken symmetry does not mean it is useless. By studying nuclear many-body systems which deviate from the idealized isospin framework, we can learn about what components contribute to this deviation, i.e. we can learn about nuclear structure.

Isospin is considered an intrinsic property of protons and neutrons, both being assigned a total isospin of $T = 1/2$. The particles are distinguished with isospin projections $T_z = -1/2$ for the proton and $T_z = +1/2$ for the neutron². Because the mathematics of isospin are analogous to that of intrinsic spin, for a many-body quantum system consisting of $A = N + Z$ nucleons, the total isospin projection is,

$$T_z = \frac{1}{2}(N - Z), \tag{2.1}$$

while the total isospin of the state adheres to,

$$T = |T_z|, |T_z| + 1, |T_z| + 2, \dots, A/2. \tag{2.2}$$

For each value of T , we can find as many as $2T + 1$ eigenstates of the \vec{T}^2 operator denoted by their value of T_z . These states form what are known as isobaric multiplets and are usually referred to by their size: doublets ($T = 1/2$), triplets ($T = 1$), quadruplets

²Note that this is the convention used in nuclear physics. High energy physicists use the reversed convention!

($T = 3/2$), quintets/quintuplets ($T = 2$), sextets ($T = 5/2$), and septets ($T = 3$). In principle the list could go on, but to my knowledge, empirical data has only been provided up to the septets [49]. The states within an isobaric multiplet are known as isobaric analog states. Note that because isobaric analog states are a nuclear configuration, they are not restricted to being only nuclear ground states. In fact, many nuclei have excited states which are isobaric analogs of the ground state in another nucleus. Therefore, more often than not, identifying all of the isobaric analog states in a multiplet requires data on both the mass and level structure of the nuclei.

Even at the scale of many-body nuclear systems, we still see evidence that isospin is a very good approximation. This is possibly best demonstrated by showing the low-lying level structure of a mirror nuclei pair; nuclei which are mirrored about the $N = Z$ line because their proton and neutron content are exchanged. A good example is the ^{23}Na - ^{23}Mg mirror pair which has binding energies of 8111.494(5) keV per nucleon and 7581.25(14) keV per nucleon, respectively. The difference in binding energy can be attributed to the extra proton that ^{23}Mg carries (12 protons) which lowers the overall binding energy through increased Coulomb repulsion. Despite the different binding energies, the level structure of these nuclei with reference to the ground state are very similar, which can be seen in Figure 2.1. Because exchanging the proton and neutron content means we are also exchanging the proton-proton and neutron-neutron pairing forces, this shows that the charge symmetry of the nuclear force holds well at the scale of the many-body system.

If isospin were a perfect symmetry in nature, the isobaric analog states in a multiplet would exhibit exact degeneracy. However, as we know that isospin is not a perfect symmetry, any isospin non-conserving interaction will remove the degeneracy. The two most-well understood violators of isospin symmetry are Coulomb repulsion between

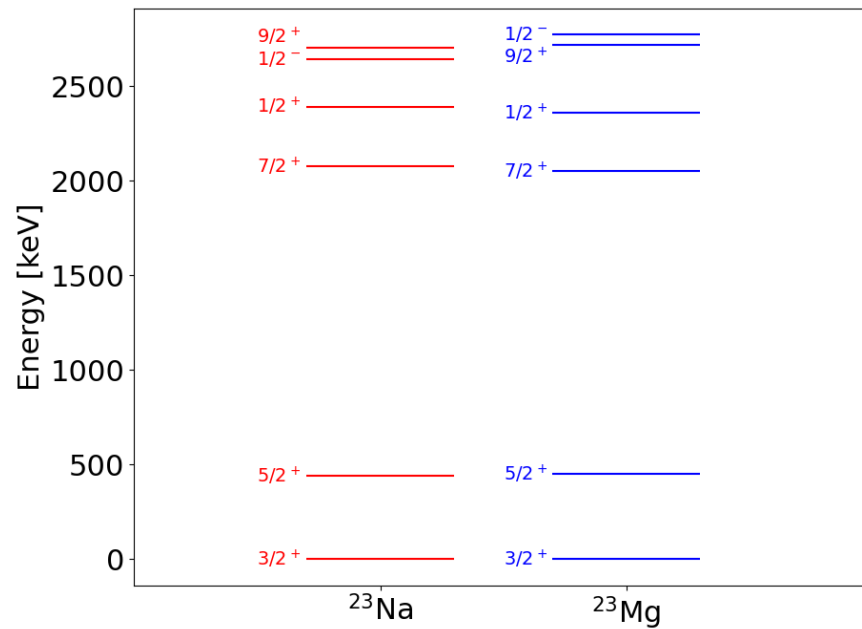


Figure 2.1: A comparison of the low-lying level structure of ^{23}Na and ^{23}Mg which are known as mirror nuclei because their proton and neutron numbers are exchanged. For levels of the same J^π , the excitation energies are nearly the same but clearly not degenerate. We can see that isospin symmetry breaking effects reverse the order of the $1/2^-$ and $9/2^+$ levels. Data obtained from the National Nuclear Data Center at Brookhaven National Laboratory [50].

protons and the small difference in mass between the proton and neutron. In Chapter 1 we briefly mentioned the early work into studying the Nolen-Schiffer anomaly and the realization that an additional contribution to isospin violation is through the isospin non-conserving parts of the nuclear force [19, 23].

While the effects of isospin symmetry breaking beyond the Coulomb interaction are small on the scale of nuclear structure and properties, it is important to understand their contributions for a number of different reasons. One major interest stems from the implication that isospin symmetry has in the transmutation of protons into neutrons and vice-versa, known as β -decay. A special case of these transitions known as superallowed Fermi decays occur between isobaric analog states solely through the vector component of the hadronic weak interaction. The ft -value is a measurable parameter that characterizes the rate at which a particular β -decay occurs. The ft -values for these particular transitions can be made nucleus-independent through radiative and isospin symmetry breaking corrections. As it currently stands, the nucleus-independent ft -values (also called $\mathcal{F}t$ -values) have been evaluated for fifteen different superallowed Fermi transitions [51]. If these $\mathcal{F}t$ -values remain constant, this would serve as confirmation for the conserved vector current (CVC) hypothesis [52]. Furthermore, these values can be used to extract the weak-interaction coupling constant which is an important factor in testing the top-row unitarity of the Cabibo-Kobayashi-Maskawa (CKM) quark mixing matrix [53]. Recent re-evaluations of these radiative corrections have led to a tension in the unitarity test of the first row in the CKM matrix. A significant uncertainty contribution is due to the isospin symmetry breaking correction [54–56].

In addition to the impact on fundamental interactions, a precise determination of the isospin symmetry breaking contribution to nuclear structure is important for other isospin-

related processes such as β -delayed proton emission [57], astrophysical applications such as the rp-process [58–60], and can even be used to predict the masses of unmeasured neutron-deficient nuclei to 10 keV precision [49].

2.1.2 The isobaric multiplet mass equation

To study isospin symmetry breaking effects in nuclei, it is necessary to develop a system to quantify the binding energy (or mass) difference within multiplets. The classic way to do this is using the Isobaric Multiplet Mass Equation (IMME) which is a straight forward prediction derived from the isospin symmetry concept. It is pertinent to provide an outline of the derivation here so that the reader can appreciate its impact.

The effect of a small isospin-violating interaction can be treated using perturbation theory to determine the energy splitting within a multiplet. We start with the isospin-independent Hamiltonian H_{II} , which has eigenstates $|\alpha, T, T_z\rangle$, where α contains the other quantum numbers that define the state. Because this Hamiltonian conserves isospin, the eigenvalues are independent of T_z and therefore there is no energy splitting between isobaric analog states. To induce splitting, we include an isospin-violating interaction H_{IV} which we assume to only consist of two-body forces such that they can be written as a tensor of rank two³:

$$H_{IV} = \sum_{k=0}^2 H_{IV}^{(k)}, \quad (2.3)$$

which is expanded as a sum of the isoscalar ($k = 0$), isovector ($k = 1$), and isotensor ($k = 2$) components [23]. These components are related to the nucleon-nucleon interactions v as

³The Coulomb interaction, for example, is a scalar field but can be written as a rank 2 tensor through the use of the Kronecker delta.

follows [15, 23]:

$$H_{IV}^{(0)} = \frac{v_{pp} + v_{nn} + v_{np}}{3}, \quad (2.4)$$

$$H_{IV}^{(1)} = v_{pp} - v_{nn}, \quad (2.5)$$

$$H_{IV}^{(2)} = v_{pp} + v_{nn} - 2v_{np}. \quad (2.6)$$

We see that the isovector component gives a measure of the charge symmetry breaking of the nuclear force and the isotensor component gives a measure of the charge independence breaking of the nuclear force. The energy splitting between isobaric analog states is determined with the expectation value of the isospin-violating interaction:

$$E(\alpha, T, T_z) = \langle \alpha, T, T_z | \sum_{k=0}^2 H_{IV}^{(k)} | \alpha, T, T_z \rangle. \quad (2.7)$$

The T_z dependence can be pulled out using the Wigner-Eckart theorem [61], and further simplifications yield the energy splitting in a recognizable form:

$$E(\alpha, T, T_z) = \frac{1}{\sqrt{2T+1}} \left[M^{(0)} + \frac{T_z}{\sqrt{T(T+1)}} M^{(1)} + \frac{3T_z^2 - T(T+1)}{\sqrt{T(T+1)(2T+3)(2T-1)}} M^{(2)} \right], \quad (2.8)$$

where the $M^{(k)}$ are the reduced matrix elements which are independent of T_z and would be written as $\langle \alpha, T | H_{IV}^{(k)} | \alpha, T \rangle$ in full form. The final step is to organize the equation into terms of T_z which yields a quadratic:

$$E(\alpha, T, T_z) = a + bT_z + cT_z^2, \quad (2.9)$$

where the a , b , and c coefficients are functions of T and the reduced matrix elements. Equation (2.9) is the famed IMME and it gives us a remarkably simple prediction that the

energy splitting within an isobaric multiplet follows a quadratic behaviour in T_z .

The a coefficient depends on the isoscalar interaction and the isotensor interaction. The b and c coefficients are purely dependent on the isovector and isotensor interactions, respectively. As such, the b and c coefficients are used to study the charge symmetry breaking and the charge independence breaking effects of the nuclear force. While the IMME was originally derived with the Coulomb interaction, it is valid for any isospin violating interaction. This means that only the *values* of the IMME coefficients would be affected by the presence of additional isospin non-conserving forces. The Coulomb interaction is largely able to reproduce the strength of the isovector interaction, but not the isotensor interaction. This observation is the manifestation of the Nolen-Schiffer anomaly, which was first observed in $T = 1/2$ mirror nuclei [19], and later in $T = 1$ analog states [62], and showed that parts of the nucleon-nucleon interaction also violate isospin symmetry.

In deriving the IMME, higher-order perturbations and three body forces are not considered. In the case that these effects are strong, the quadratic nature of the IMME would no longer be an appropriate description for the energy splitting within isobaric multiplets. Another assumption of the IMME is that the nuclear states exist as isospin pure states. Because the *total* nuclear Hamiltonian will not conserve isospin, the eigenstates of this Hamiltonian will be a mixture of isospin states. This is known as isospin mixing and is an active field of research in the study of nuclear structure. The presence of such fragmented isospin states will also result in deviations from the quadratic form of the IMME [63, 64].

Experimentally, the a coefficient defines the bulk mass which is on the scale of 10 – 100 MeV/c², the b coefficient is the scale of 1 – 10 MeV/c², and the c coefficient is on the scale of 100 keV/c². Coefficients for a cubic dT_z^3 and even a quartic eT_z^4 term have been

added to the IMME as a method to test its validity [49, 63]. However, these coefficients can only be uniquely determined with the appropriate size isobaric multiplet. The cubic d coefficient requires a four-member quadruplet ($T = 3/2$ or greater) and the quartic e coefficient requires a five-member quintet ($T = 2$ or higher). The presence of a non-zero d coefficient suggests that the quadratic form of the IMME is insufficient to describe member energy splitting which could be due to isospin mixing, higher order perturbations, or three-body interactions [63]. Recent evaluations of the IMME in the $A = 10 - 60$ range suggest the quadratic form holds quite well even for larger multiplets. The majority of evaluated d coefficients are considered zero within uncertainty, but there are a few non-zero cases standing out such as the $T = 3/2$ multiplets at $A = 9, 35$ [49, 63]. In many of these cases the presence of a non-zero d coefficient can be better determined with more precise mass measurements. The validity of the IMME is beyond the scope of the measurements performed in this thesis so it is not further discussed.

A simple theoretical approximation of the IMME coefficients can be derived by assuming the nucleus to be a homogeneously charged sphere. The total Coulomb energy due to the Z protons in the nucleus can be calculated as the sum of stored energy per proton pair:

$$E_{\text{coulomb}} = \frac{3e^2}{5R}Z(Z - 1), \quad (2.10)$$

where the radius of the nucleus is related to the total nucleon content by $R = r_0A^{1/3}$. Equation (2.10) can be used to derive an approximation of the IMME coefficients [15]:

$$a_{\text{hcs}} = \frac{3e^2A(A - 2)}{20r_0A^{1/3}}, \quad (2.11)$$

$$b_{\text{hcs}} = -\frac{3e^2(A - 1)}{5r_0A^{1/3}}, \quad (2.12)$$

$$c_{\text{hcs}} = \frac{3e^2}{5r_0A^{1/3}}, \quad (2.13)$$

where e is the elementary charge and $r_0 \approx 1.2$ fm. Equations (2.11), (2.12), and (2.13) provide a global estimation of the coefficients and are useful for studying the basic trends of IMME coefficients. These equations can be extended to include additional terms for the quantum mechanical Coulomb exchange term [65], and proton pairing effects [66, 67].

2.1.3 Mass measurements to extend the IMME

Providing new IMME coefficients requires mass measurements and precise knowledge of level structures to determine the correct members of a multiplet. In this thesis we perform precision mass measurements of $^{74-76}\text{Sr}$, but the level structure of these nuclei is not well-known due to their proximity to the proton dripline [68]. However, some low-lying multiplets such as the $T = 1/2$ doublets and the $T = 1$ triplets can be completed with only ground state masses [49, 63]. These ground state mass measurements can provide the first foray into extending the IMME coefficients to higher masses.

The $T = 1/2$ doublets

The $T = 1/2$ doublets are created from isobaric analog states in odd- A nuclei. The lowest set of isobaric analog states that can be used to create the doublets require no level structure knowledge because they are the nuclear ground states [63]. As a two-member multiplet, only the b coefficient is required to describe the energy splitting between the isobaric analog states. Because these are ground state masses of mirror nuclei, the b coefficient effectively describes the difference in binding energy of the mirror nuclei. If indirect mass measurements are included, the recent AME 2020 evaluation [69] provides mass data to complete the lowest-

lying doublets up to $A = 75$. The b coefficients extracted from these doublets are shown in the top panel of Figure 2.2 where we can see a negatively sloped trend line that is steadily increasing. This trend line can be understood as due to the general increase in Coulomb repulsion in the nucleus as Z increases.

Although it is difficult to see at the resolution of the plot, there is a subtle oscillation of the b coefficients superimposed onto the trend line. The oscillations are much smaller than the slope of the line, therefore they are best seen by plotting a derivative of b :

$$\Delta b \equiv b(A) - b(A - 2). \tag{2.14}$$

The bottom panel of Figure 2.2 shows a plot of Δb where the oscillatory effect is now much more pronounced. It is very important to note here that this oscillation is often called a staggering pattern and can be interpreted in two ways, both of which are shown in the bottom panel of Figure 2.2. If we draw a trend line between neighboring points (dashed black line), we see a staggering pattern. However, we can also view the pattern as a separation of the high values and the low values into different multiplet subgroups (red and blue solid lines). All of the high values occur at masses where $A = 4n + 1$ (where n is a positive integer), while all of the low values occur at masses where $A = 4n + 3$.

What this staggering pattern suggests is that energy splitting between mirror nuclei is slightly above average for $A = 4n + 1$ nuclei and slightly below average for $A = 4n + 3$ nuclei. This staggering pattern was first studied by Feenberg and Goertzel [71] and explained as due to an increase in Coulomb repulsion between spin-antialigned protons which exist closer together in space. Therefore the Coulomb repulsion is stronger in nuclei with fully-paired protons. Other analytical models have also been used to explain the staggering effect [66,67,72,73].

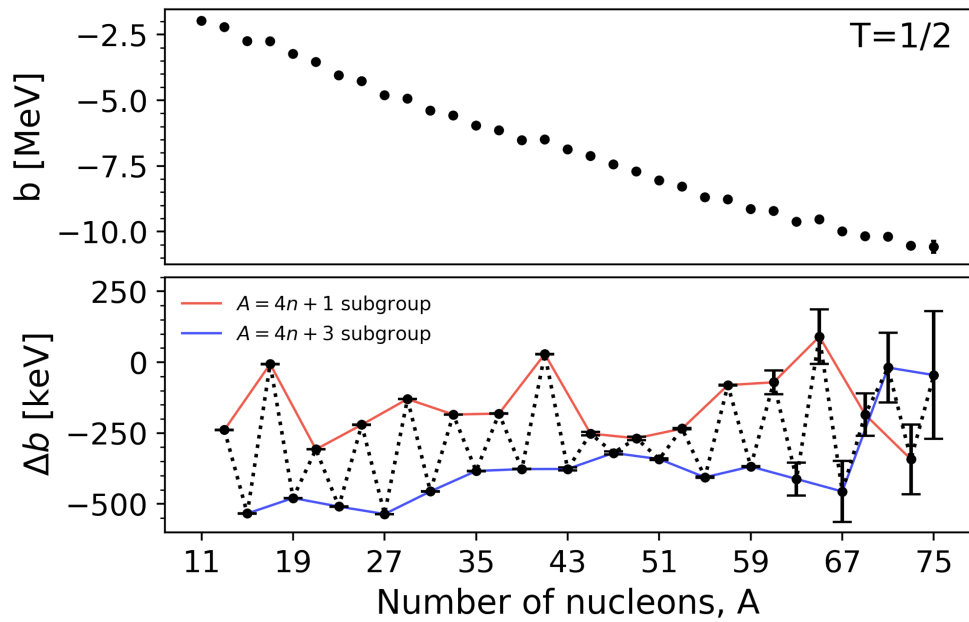


Figure 2.2: The top panel shows the b coefficients for the $T = 1/2$ doublets. For a better look at the non-trivial structure of the b coefficients, the bottom panel shows Δb . Two distinct trend lines are seen along the $A = 4n + 1$ and $A = 4n + 3$ multiplet sub-families. The staggering anomaly at $A = 69 - 75$ sees these trend lines cross. The mass data is obtained from the AME 2020 [69] and the excitation energies from ENSDF [70].

Multiple theoretical approaches have successfully reproduced the doublet b coefficients including the staggering pattern up into the medium mass range [24, 60, 74–76]. However there exists an anomaly in the data beginning in the upper fp-shell at $A = 69$, which shows that the staggering phase of the doublet b coefficients actually changes. This has been dubbed a “staggering anomaly” because the regular high-low oscillation inverts to a low-high oscillation. Shown in Figure 2.2, this can also be viewed as a crossing of the trend lines along the $A = 4n + 1$ and $A = 4n + 3$ multiplet subgroups. The presence of this staggering anomaly was first mentioned in a paper by Kaneko *et al.* [74], where the experimental data deviated from their modern shell model predictions. Other theoretical predictions such as a density function theory approach [75], and an *ab initio* VS-IMSRG approach [76] are also not able to reproduce this anomaly. It has been suggested that the staggering anomaly could be reconciled if the current mass value of ^{69}Br in the AME2020 mistakenly measured an isomeric state [77].

This brings us to an important point which is that the mass uncertainty of the doublet b coefficient ranges from less than 1 keV in the low and medium mass range, to more than 100 keV in the $A > 60$ range. The mass uncertainty suffers especially for $T_z = -1/2$ nuclei such as ^{69}Br [78, 79] and ^{73}Rb [80, 81] which are proton-unbound and must be measured using indirect methods. In addition to the proton-unbound ^{69}Br and ^{73}Rb , increased mass precision for both ^{71}Kr and ^{75}Sr can have an impact and possibly resolve this anomaly.

It should be noted here that two related phenomena known as continuum coupling [82] and the Thomas-Ehrman effect [83, 84] could cause an isospin-dependent shift of analog states in weakly-bound and unbound nuclei near driplines. The first phenomenon is due to the coupling of a weakly bound nuclear state to the continuum which results in an energy shift of the nuclear state. The Thomas-Ehrman effect is an isospin-dependent energy shift due

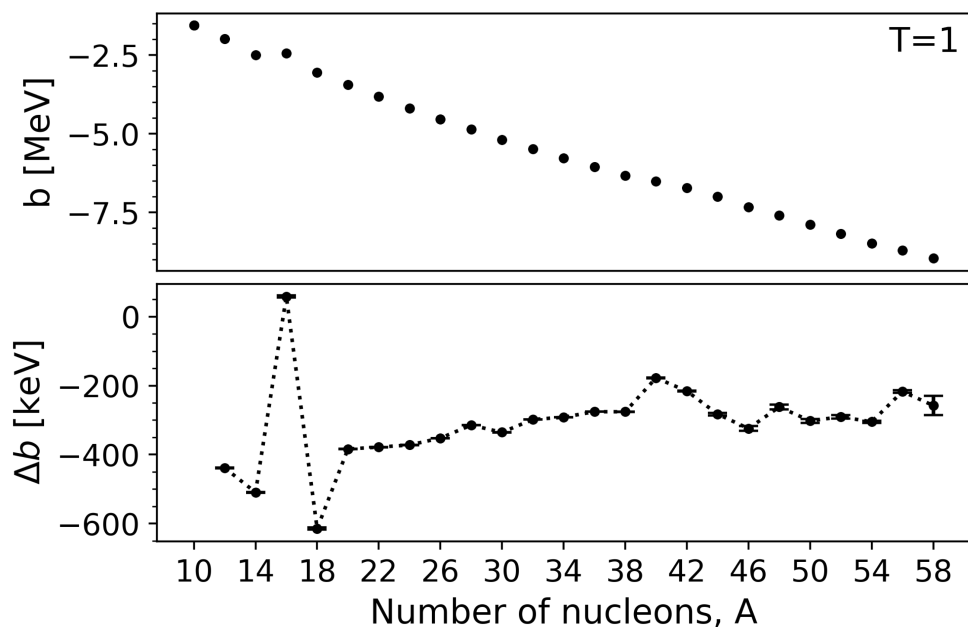


Figure 2.3: The b coefficients are shown for the $T = 1$ triplets. The mass data is obtained from the AME 2020 [69] and excitation energies from ENSDF [70].

to a distortion of the spatial wavefunction of an unbound nuclear state. Because the proton and neutron driplines are asymmetric, both of these energy shifts are isospin dependent. Systematic studies of the Thomas-Ehrman effect have suggested that the shift is rather small for heavier nuclides [85, 86]. Both of these phenomena are beyond the scope of the work presented in this thesis.

The $T = 1$ triplets

The $T = 1$ triplets are constructed from mass and level structure data of even- A nuclei. In the case of the lowest-lying triplets, it is common that the $T_z = \pm 1$ isobaric analog states are nuclear ground states and that the $T_z = 0$ analog state is an excited state. At masses higher than $A = 40$, the $T_z = 0$ state tends to be a nuclear ground state if $A = 4n + 2$ (where

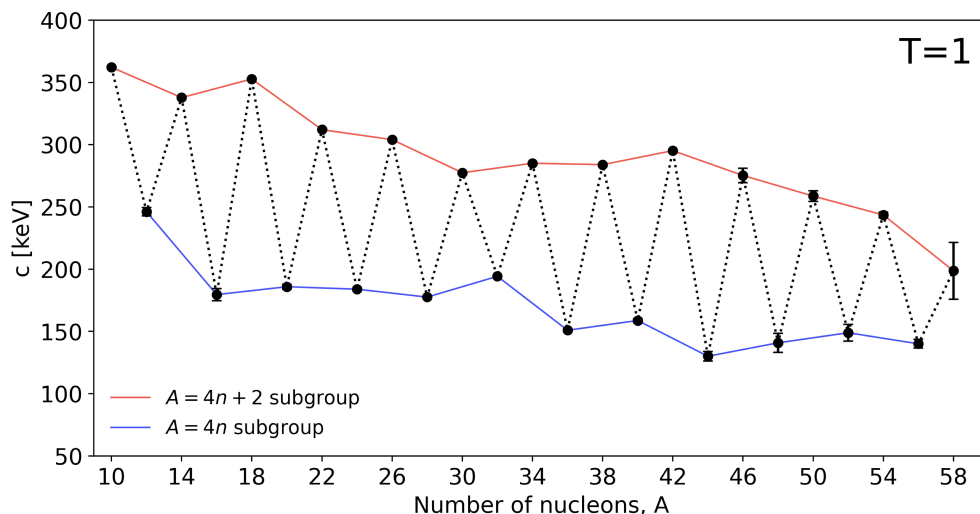


Figure 2.4: The c coefficients are shown for the $T = 1$ triplets. The mass data is obtained from the AME 2020 [69] and excitation energies from ENSDF [70].

n is a positive integer) but an excited state if $A = 4n$. The details of these isobaric analog states are well documented by MacCormick and Audi [49], who evaluated the triplets up to $A = 58$. Recent mass measurements of ^{60}Ga [87] and ^{66}Se [88] have extended the list of fully experimentally evaluated triplets, but progress into higher masses has remained an elusive goal. ^{60}Ga is part of a $A = 4n$ triplet while ^{66}Se is part of a $A = 4n + 2$ triplet.

The triplets are the smallest multiplet that allows us to extract a c coefficient in addition to the b coefficient, which allows us to study the isotensor nature of the nucleon-nucleon interaction. It is interesting to note that the presence of a staggering pattern in the triplet coefficient data is not the same as for the doublets. As can be seen in Figure 2.3, the triplet b coefficients do not show any sort of clearly resolved staggering pattern even when plotting Δb . However, as can be seen in Figure 2.4, the triplet c coefficients do indeed show a staggering pattern. Because the triplets are constructed from even- A nuclei, the staggering pattern exists between $A = 4n$ (n is a positive integer) and $A = 4n + 2$ nuclei. While the

level structure of ^{74}Sr is not well studied, a mass measurement would complete the $A = 74$ triplet because the $T_z = -1$ isobaric analog state is expected to be the ground state for the $A = 4n + 2$ multiplet families [49, 63]. While this will provide newly evaluated b and c coefficients, analysis of the staggering pattern in the c coefficients is not possible because there is no neighboring coefficient data. However, comparison with a simple model such as the homogeneously charged sphere model (Equations (2.11), (2.12) and (2.13)) would allow us to verify if the coefficients are indeed following general trend lines.

2.1.4 Alternatives to the IMME

Before moving to the next section, it is important to briefly note some of the other methods to organize experimental data to study isospin symmetry breaking in nuclei. In addition to the IMME, some of the references used in this thesis use what are known as Coulomb Energy Differences (CED) and Coulomb Displacement Energies (CDE) [75, 76, 89]. When referring to the CED of a specific isospin multiplet, it is common to use alternative terms such as Mirror Energy Differences and Triplet Energy Differences.

CEDs look specifically at the differences in excitation energies between isobaric analog states within a multiplet. These values are also sensitive to the isospin symmetry breaking effects in nuclei and due to their use of excitation energies, they do not require ground state mass measurements. This can be extremely useful in the cases of nuclei near the proton drip line when high mass resolution is difficult to achieve but fast spectroscopy methods can be performed to elucidate level structure [68]. In contrast to the IMME coefficients which are built from nuclear mass excess (see Eq 1.1), CDEs are built from nuclear binding energy which is defined as

$$\text{BE}(N, Z) \equiv ZM_{\text{H}} + NM_{\text{n}} + M(N, Z), \quad (2.15)$$

where M_{H} is the mass of the hydrogen atom, and M_{n} is the mass of the neutron. Therefore, while they follow a different convention than the IMME, the information carried by both is exactly the same and a conversion between the values is quite easy to perform.

2.2 The rp-process in Type I X-ray bursts

Chapter 1 briefly introduced the physics motivation for mass measurements of $^{74-76}\text{Sr}$ with respect to the rp-process in Type I X-ray bursts. This section dives into the reasoning in more detail by giving an overview of Type I X-ray bursts, how we observe them, how we use model-observation comparisons to learn more about them, why masses are a critical input for the accuracy of these models and why the specific region around $^{74-76}\text{Sr}$ is of importance. Much of the information in this section is, unless otherwise stated, sourced from the excellent articles by Galloway and Keek [26] and Parikh *et al.* [36].

2.2.1 Type I X-ray bursts

Binary star systems are a class of astronomical systems in which two stars exist interacting and orbiting around a common center of mass. A subset of these binary star systems are named X-ray binaries because they continuously emit a flux of X-rays due to the accretion of matter from one star (the donor) onto the surface of the other star (the accretor). The persistent flux of X-rays is largely due to the conversion of the material's gravitational potential energy into kinetic energy and heat. Typically, the accretor is a neutron star or a black hole, and the donor is a relatively light star in comparison. A subset of these X-ray binaries are known as X-ray bursters because they exhibit periodic, transient increases in X-ray luminosity followed by a slow relaxation. The most commonly observed and well

studied X-ray burst is the Type I X-ray burst in which the burst mechanism is caused by a thermonuclear runaway.

The burst event begins with the accretion of hydrogen and helium rich material taken from the outer layers of a low mass companion star similar in mass to the mass of the Sun. This companion star loses its outer layers by Roche Lobe overflow which is when its size exceeds its gravitational “sphere of influence” into the gravitational influence of the neutron star. As the material falls onto the neutron star, strong lateral pressure gradients disperse it across the surface and a layer of fuel starts to accumulate. Compression of the fuel increases its temperature and pressure until conditions suitable for nuclear fusion are reached. Under normal circumstances, this layer would thermally expand leading to a decrease in density and a cooling effect. However, the well-known thin-shell instability prevents the layer from cooling by thermal expansion and allows the temperature to continue increasing [90, 91]. At least three fusion processes are identified to be important for burst ignition including the CNO-cycle, the 3α process, and $^{12}\text{C}+^{12}\text{C}$ fusion. Each of these processes contribute to energy generation within the layer and further increase the temperature leading to thermonuclear runaway.

Burst properties are strongly dependent on the overall mass accretion rate \dot{M} as well as the initial hydrogen mass fraction of the fuel. The presence of hydrogen in the fuel will push the thermonuclear runaway into higher masses through (α, p) reactions and proton capture reactions. The specific process that we are interested in is known as the rapid proton capture process (rp-process) [14, 25] and it is the primary source of energy for the burst event. The total amount of energy released during the burst event is approximately 10^{39-40} erg^4 [43]. To give an idea of the magnitude, the eruption of mount St. Helens in

⁴Erg is a unit of energy typically used in astrophysics. 1 erg is 100 nJ

1980 released approximately 10^{24} erg [92]. While the burst does release immense amounts of energy, this is not enough to destroy the accreting star or the donor star. Furthermore, the ashes resulting from the burst are not expected to escape the gravitational influence of the neutron star. While mechanisms to facilitate the escape of burst ashes into the interstellar medium are under investigation [31, 32], it is currently unclear whether thermonuclear X-ray bursts contribute to galactic nucleosynthesis. The periodicity of X-ray bursts is due to this repeated re-accumulation of burst ashes back onto the neutron star surface causing re-ignition. Because the burst ashes are replacing the original neutron star crust, the bursts have direct impact on neutron star properties [34, 93]. Therefore it is important to constrain what ashes are produced during the bursts because the neutron star crust plays an important role not only in the accretion and ignition mechanisms but also the general equation of state of the neutron star.

2.2.2 Observational features of thermonuclear X-ray bursts

Bursts appear as brief flashes in the X-ray spectrum that stand above the persistent X-ray flux contributed by the accreting matter. The X-ray burst profile is typically known as a “light curve” and is sensitive to the underlying physics mechanisms involved in the burst. Some of the basic characteristics of the light curve are the rise time, peak luminosity, fall time, burst duration, and recurrence time. Also observed is the spectral evolution and absorption lines of the light curve which can provide important information on the underlying physical processes involved in the burst. For example, the initial phase of the burst exhibits high-energy X-rays characteristic of the thermonuclear reactions responsible for the burst ignition. As the burst proceeds, the X-ray emission shifts to a lower energy in what is known as a spectral softening which reflects the cooling atmosphere of the neutron star.

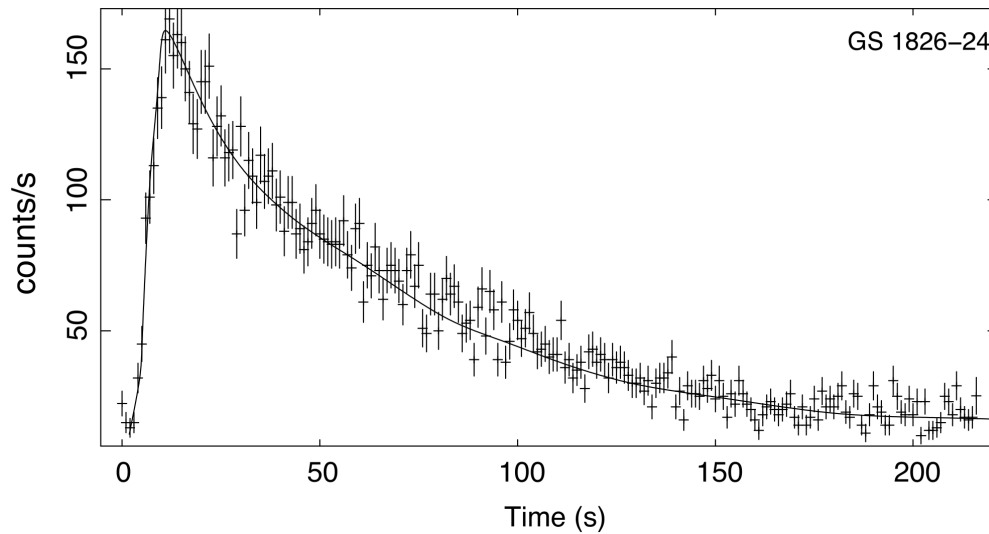


Figure 2.5: The light curve of GS 1826-24 shows the intensity of X-rays observed over the duration of an X-ray burst. This burst event was observed by the Swift X-ray telescope [98]. This image is modified from [36].

Generally, the shape of the light curve shows a rapid rise in luminosity on the order of 1–10 seconds followed by an exponential decrease on the order of 100 seconds. However, it is important to point out that light curve characteristics will vary quite a bit depending on the system being studied. The burster 4U 1636-536 is known for frequent and intense bursts but also exhibits unique characteristics such as doubly- and triply-peaked light curves [36]. MXB 1659-29 displays highly irregular burst behaviour and can often be quiescent for long periods of time between burst events [94]. Figure 2.5 shows the light curve of the well studied thermonuclear burster GS 1826-24 in the Sagittarius constellation which has been named the “clocked burster” due to its extremely predictable recurrence time [95]. Because of this, GS 1826-24 is somewhat of a “textbook” burster and is often used for model-observation comparisons [33, 96, 97].

2.2.3 X-ray burst modelling

Because it is difficult to study the reaction sequence of an X-ray burst using terrestrial experiments, we are left to observe the phenomena from afar. Luckily, a wide variety of X-ray burster systems are observed and this allows us to explore how different initial conditions might be connected to the observed light curve. A critical task for this is the development of computational models to simulate the X-ray burst events. In fact, much of the information provided above has been deduced from comparisons of observed burst light curves with computational models of the burst events. These model-observation comparisons allow a better understanding for how fuel composition, accretion rate and other physical quantities can affect and be responsible for the observed light curves. Before we explicitly discuss experimental input for computational models, we review some of the major milestones in understanding X-ray bursts through model-observation comparisons.

The first observations of the transient burst behaviour on accreting neutron stars came from several different satellite observations of the Norma constellation in the early 1970's [99–101]. Not shortly after, unstable accretion-powered thermonuclear burning was already being studied as a source for the X-ray flashes [90]. During this time, many new burst sources were being discovered mostly with observations from SAS-3 and OSO-8 X-ray observatories. It was also around this time when physicists realized that unstable thermonuclear burning could not account for all of the observed burst characteristics and bursts were separated into Type I (thermonuclear) and Type II (accretion instabilities) [102]. In 1981, Wallace and Woosley first proposed explosive hydrogen burning and the rp-process as mechanisms for the extended exponentially decaying tail seen in some burst light curves [25]. This ground breaking paper also introduced the concept of a “waiting point nucleus”; a bottleneck along the rp-process where the reaction flow is significantly stalled.

The extreme scale of the parameters of an X-ray burst presents a significant challenge for computational models and therefore a balance between capturing the relevant degrees of freedom and managing computational resources must be struck. However, with the basic groundwork for burst modelling complete, the field began to see the incorporation of more detailed nuclear reaction networks and multi-zone calculations into X-ray burst models. Every model that is currently used applies some sort of restriction to reduce the complexity of the problem and make a solution relatively tractable. The models can be categorized as single-zone models, one-dimensional multi-zone models, and multi-dimensional models.

Advancements began with single-zone burst models which involve reaction networks and ignition conditions, but restrict the model space of the neutron star surface to a single homogeneous zone where the reactions occur. While these models have a limited ability to capture complex mechanisms of the burst, they have demonstrated usefulness for investigating basic model parameters of the burst such as ignition conditions, energy sources for the burst, and key reaction rates. For example, Schatz *et al.* used a single-zone model and included over 600 different isotopes in the reaction network to map out the full extent of rp-process involvement in X-ray bursts [37]. They concluded that the rp-process has a natural termination point at $A \approx 104$ because α -emitting Te isotopes form a SnSbTe cycle. These models have also been used to evaluate nuclear reaction rate uncertainties and their impact on the light curve and burst ashes [40, 43, 103]. The role that single-zone models currently occupy is for investigating large parameter spaces of X-ray bursts with the intention using follow-up multi-zone calculations if a notable deviation is found.

A step up from the single-zone burst models is to assume spherical symmetry and simulate one dimension along the radial coordinate of the neutron star. Along the radial coordinate, different zones can be defined which represent the different layers of the

neutron star such as the core, crust, ocean and atmosphere. With these models the spatial variation of properties such as temperature, density, and composition can be included into the simulation. Most models assume a hydrostatic equilibrium but apply some implicit schemes to include convective and turbulent mixing between the layers [26]. These models have done quite well to realistically reproduce burst observations such as the GS 1826-24 “textbook burster” mentioned earlier [97]. They have also helped to discover new phenomena such as “compositional inertia” which is the reduction in down-time between bursts due to mixing of previous burst ashes with freshly accreted hydrogen and helium fuel [104]. Convective mixing in the neutron star layer and the rate of flame spreading across the neutron star surface are two important mechanisms that need to be further investigated to understand how they affect the bursts. These are studied with multi-dimensional burst models that include latitudinal and longitudinal directions in addition to the radial coordinate. For the purposes of this thesis, we focus on the single-zone model because new mass values allow one to investigate important reaction sequences within the rp-process.

2.2.4 Nuclear masses for burst modelling of the rp-process

Figure 2.6 shows the nuclear reaction flow path of a simulated X-ray burst approximately 1 ms after the burst began. The line thickness is indicative of the degree of mass flow through the specific reaction. Also highlighted are the different nuclear reaction pathways involved. The reaction pathway is heavily influenced by fuel composition and mass accretion rate, but generally speaking we have three reaction sequences that build up towards the rp-process. The triple- α process fuses three ^4He nuclei to produce carbon. This carbon is used by the catalytic hot CNO cycle which converts hydrogen into helium. An interplay between these

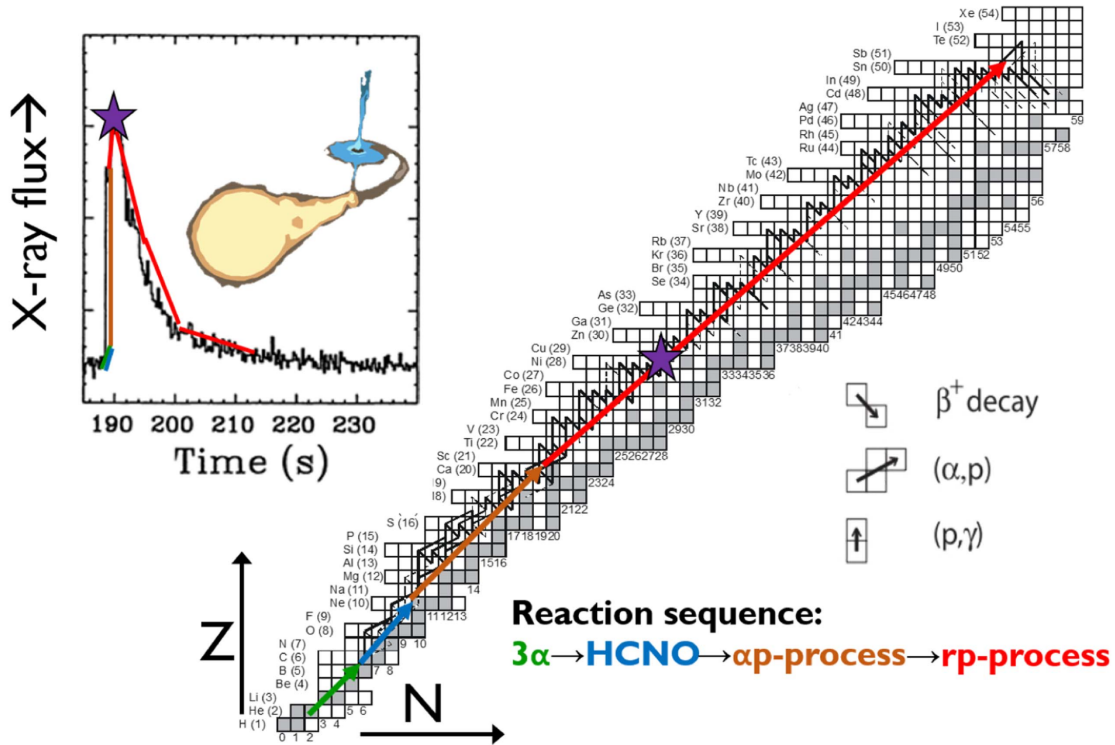


Figure 2.6: A plot illustrating the reaction flow of a simulated X-ray burst and the produced light curve. The black lines indicate the reaction flow predicted by the simulation. Underlying reaction sequences and their connections to the light curve are indicated with colored lines. The purple star indicates the reaction flow through the ^{56}Ni region which drives the peaking of the light curve. Figure from [34].

two processes increases helium abundance and temperature until the reaction flow can break out into the αp -process using $^{15}\text{O}(\alpha, \gamma)$ and $^{18}\text{Ne}(\alpha, p)$ reactions [34]. The (α, p) process is a series of (α, p) and (p, γ) reactions which push the reaction flow towards higher mass nuclei as well as more proton-rich nuclei. This releases a significant amount of energy in the form of X-rays and is responsible for the sharp initial rise of the light curve. Eventually the (α, p) reaction weakens and the reaction flow must proceed by the rp-process.

The rp-process involves a competition between proton capture (p, γ) , reverse photo

disintegration (γ, p), and β -decay. At the high temperatures and densities present during the burst event, the (p, γ) reaction strongly supports upwards movement along isotonic lines. When the reaction flow begins to reach the proton drip line, the cross section for (γ, p) becomes competitive with the diminishing (p, γ) reaction and the reaction flow must proceed via β -decay onto the next isotonic chain. Thus we can understand the general zig-zag pattern shown by the rp-process in Figure 2.6. Because the (p, γ) and (γ, p) reactions are much faster than β -decay, there tend to exist local equilibrium conditions between neighboring isotones. As a result, the β -decay half-life can have a significant effect on the overall reaction flow. At a waiting point nucleus, a local (p, γ) - (γ, p) equilibrium has developed between neighboring isotones and cannot proceed to the next isotonic chain because it is limited by a slow β -decay. Because the rp-process is the main source of energy generation, the effects of waiting point nuclei can strongly influence the light curve. Some well-known waiting point nuclei include ^{56}Ni , ^{64}Ge , ^{68}Se , ^{72}Kr , ^{76}Sr and ^{100}Sn [34].

The experimental nuclear physics community has dedicated a significant amount of resources towards providing empirical data for X-ray bursts. However, only a small fraction of these data are direct measurements of nuclear reactions involved in X-ray bursts. What has been measured includes reaction rates relevant to breakout from the hot CNO (carbon-nitrogen-oxygen) cycle into the rp-process such as $^{14}\text{O}(\alpha, p)$ [105], $^{15}\text{O}(\alpha, \gamma)$ [106], and $^{18}\text{Ne}(\alpha, p)$ [107]. Above the hot CNO cycle, reaction studies near low-mass waiting point nuclei such as ^{30}S have also been performed [108, 109]. However, because the rp-process proceeds at higher masses along the proton drip line and contains thousands of reactions which cannot be directly observed, the majority of these reactions are calculated using nuclear reaction models.

The most widely used model for estimating nuclear reaction rates is the statistical

Hauser-Feshbach model [110]. Nuclear reaction rates are calculated by considering the interaction of a projectile such as a proton, neutron or alpha particle with a target nucleus. Rather than considering the detailed nuclear structure of the target nucleus, the simplified Hauser-Feshbach approach assumes the level structure follows a statistical ensemble through which the reaction can proceed. This greatly simplifies the process of determining reaction rates because detailed structural information of the target nucleus beyond level densities and transmission coefficients is not required. While the Hauser-Feshbach approach performs reliably well along most of the rp-process path [14], it is important to note that the assumption of a statistical ensemble of the target nucleus does not always hold. This can be a particular problem when calculating reaction rates with proton unbound nuclei along the proton drip line which can be dominated by a few resonances [111].

Through the use of these reaction rate models, the accuracy of X-ray burst network calculations is strongly dependent on the accuracy of the nuclear mass values provided as input [14, 41]. Nuclear mass values determine the reaction Q -values for β -decay, proton-capture, and other reactions. For example, the proton capture Q -value is determined as,

$$Q_{(p,\gamma)} = m(Z, A) + m_p - m(Z + 1, A + 1), \quad (2.16)$$

for mass number A , proton number Z and proton mass m_p . Because the proton-capture rate is often in a local equilibrium with the reverse photodisintegration rate, the photodisintegration rate can be calculated using the principle of detailed balance [14]:

$$\lambda_{(\gamma,p)} = \frac{2G_f}{G_i} \left(\frac{\mu k_b T}{2\pi \hbar^2} \right) \exp \left(-\frac{Q_{(p,\gamma)}}{k_b T} \right) \langle \sigma \nu \rangle_{(p,\gamma)}. \quad (2.17)$$

The G are the partition functions of the initial (i) and final (f) states, μ is the reduced mass,

$k_b T$ is the thermal energy scale, and $\langle \sigma \nu \rangle_{(p,\gamma)}$ is the proton-capture rate. We can see that because of the Boltzmann factor, the reaction rate depends exponentially on the nuclear mass values that are provided as input. In order to limit the uncertainty of calculated reaction rates, the mass uncertainty should be at least on a similar scale as the thermal energy. The thermal energy scale of an X-ray burst is $k_b T \approx 50 - 150$ keV, therefore a mass uncertainty of ~ 10 keV is needed to ensure burst model accuracy is not limited by uncertainties in Q -values [42, 112].

Providing mass values near the waiting point nuclei is a particularly effective way to pin down the reaction flow. For example, mass measurements by Schury *et al.* [113] and Tu *et al.* [114] provided the first experimental value of the proton separation energy $S_p(^{65}\text{As}) = -90(85)$ keV, showing that ^{65}As is proton unbound. This established that the effective lifetime of ^{64}Ge is reduced to less than 50% of the β -decay lifetime due to an increase in the $^{64}\text{Ge}(p, \gamma)^{65}\text{As}$ branch. For the hydrogen-rich bursts that they explored in their model, 89 – 90% of the reaction flow passed through ^{64}Ge , thereby highlighting the importance of studying the heavier waiting points at ^{68}Se , ^{72}Kr and ^{76}Sr .

2.2.5 Uncertainties in the vicinity of the ^{72}Kr waiting point

As it currently stands, some but not all of the masses relevant to the rp-process in the ^{72}Kr and ^{76}Sr region have been measured. Rodriguez *et al.* measured the mass of the waiting point nucleus ^{72}Kr with an uncertainty of 8 keV and provided calculations to determine the significance of the waiting point [115]. To determine the strength of the ^{72}Kr waiting point, they needed to address the possibility of a local (p, γ) - (γ, p) equilibrium between ^{72}Kr , ^{73}Rb and ^{74}Sr . Because the masses of ^{73}Rb and ^{74}Sr were not measured, the authors used the Coulomb displacement energy method with mirror nuclei to provide an estimate [39].

The authors determined the proton separation energies $S_p(^{73}\text{Rb}) = -0.71(10)$ MeV and $S_p(^{73}\text{Sr}) = 2.18(10)$ MeV. Their calculations further showed that in the temperature range of X-ray bursts, the local (p, γ) - (γ, p) equilibrium is established between ^{72}Kr and ^{73}Rb but not ^{74}Sr , and that ^{72}Kr is reinforced as a strong waiting point.

However, because the masses of ^{73}Rb and ^{74}Sr were extrapolated values, they should be tested with experimental measurements to validate the findings. Recently, a measurement of the β -delayed proton emission spectrum of ^{73}Sr was used to determine $S_p(^{73}\text{Rb}) = -640(40)$ keV and give more support to the strength of the ^{72}Kr waiting point [80]. However, as pointed out by Rodriguez *et al.* [115], the mass of ^{74}Sr is unmeasured and a 100-fold increase in the $^{73}\text{Rb}(p, \gamma)^{74}\text{Sr}$ reaction rate could lower the effective lifetime of ^{72}Kr . A mass measurement of ^{74}Sr will help to pin down the role of the ^{72}Kr waiting point.

2.3 Time-of-flight mass spectrometry

2.3.1 Basics of time of flight mass spectrometry

The two physics questions discussed in the previous sections provide the motivation for high precision mass measurements. TITAN has two mass spectrometers, a measurement Penning trap (MPET) [116, 117] and a multiple-reflection time-of-flight mass spectrometer (MR-ToF-MS). The MR-ToF-MS was used for the experiment performed in this thesis. This section introduces the basic concepts and principles of time-of-flight mass spectrometry using a simple linear time-of-flight model and then discusses the addition of multiple reflections. More detailed descriptions of this topic can be found for time-of-flight mass analyzers [118] and for multiple-reflection time-of-flight mass analyzers [119, 120].

The basic function of a mass spectrometer is to perform a mass measurement analysis of a sample that typically contains an unknown composition of masses. In the case of measurements of radioactive nuclei, this sample is the RIB which can contain any number of contaminants in addition to the species of interest. Most mass spectrometers use specific methods to spatially separate the sample components so that they may be individually identified. The time-of-flight mass spectrometer measures the time-of-flight of ions with mass m that are given a kinetic energy E_k and drifted along a field-free distance L . Using basic conservation of energy principles, we can derive the time-of-flight of the ions:

$$t = L\sqrt{\frac{m}{2E_k}}. \quad (2.18)$$

Hence, ions with different masses will be separated along the flight path and will arrive at a detector at different times. These different flight times can be used to build a time-of-flight spectrum where the different components of the sample are separately identified. As long as a well-known mass is also in the time-of-flight spectrum, the unknown mass or masses can be calibrated based on proximity to the calibrant.

The figure of merit of the mass spectrometer is the mass resolving power,

$$R_m \equiv \frac{m}{\Delta m} = \frac{t}{2\Delta t} \quad (2.19)$$

where the second equality is determined by substituting Equation (2.18) into the definition resulting in the mass resolving power in terms of the ion flight times. Δm and Δt are the smallest resolvable mass and time difference in the spectra, which are typically taken as the full width at half maximum (FWHM) of a peak. From Equation (2.19) we can see that the mass resolving power of a device is maximized when the flight time of the ions are maximized

but Δt is minimized.

At this point it is diligent to outline the four principle stages to time-of-flight mass spectrometry. The outline is made in the context of a discussion of a simple linear time-of-flight mass spectrometer shown in Figure 2.7. The ions begin at the stage of **sample preparation** where they are loaded into the acceleration region of the spectrometer between an electrode and a grid. The **acceleration** uses a uniform electric field E to accelerate the ions a distance L_{acc} through the grid and into the field-free region often known as the “mass analyzer”. The ions enter the **drifting** stage with a kinetic energy E_k and drift along the field-free flight path. The final **detection** stage releases the ions onto a detector where the total time-of-flight can be recorded for the subsequent building of a time-of-flight spectrum.

Some slight modifications must be made to Equation (2.18) to obtain the correct ion time-of-flight. Because the ions are given their kinetic energy by acceleration through an electrical potential, we can use $E_k = QEL_{\text{acc}}$, where Q is the ion charge state. The total ion time-of-flight is a combination of the time during acceleration and the time drifting in the field-free region:

$$t_{\text{tof}} = t_{\text{acc}} + t_{\text{drift}} = L_{\text{acc}} \sqrt{\frac{2m}{QEL_{\text{acc}}}} + L \sqrt{\frac{m}{2QEL_{\text{acc}}}}. \quad (2.20)$$

We can see that the time-of-flight of the ions is proportional to the square root of the mass-to-charge ratio m/Q . An ideal spectrometer would perfectly separate the RIB components by m/Q with an infinite mass resolving power R_m . However, there are a number of aberrations that occur in a real system. The two main culprits are small deviations in the initial position of the ion ΔL_{acc} and small deviations in the initial kinetic energy of the ions ΔE_k . Some of these aberrations can of course be compensated through specific design choices.

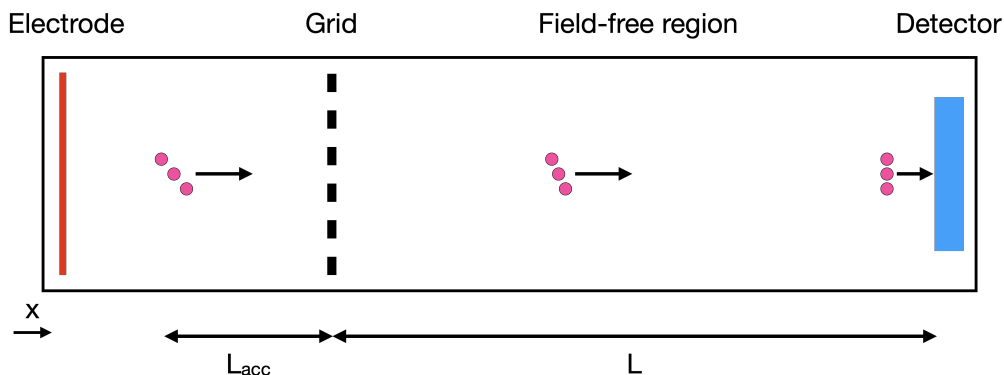


Figure 2.7: An illustration of a simple linear time-of-flight mass spectrometer.

Deviations in ion starting position

To see what happens if there is a small deviation in the initial position of an ion, we consider that,

$$L_{\text{acc}} \rightarrow L_{\text{acc}} + \Delta L_{\text{acc}}. \quad (2.21)$$

If ΔL_{acc} is positive then the ion is “a little behind the starting line” and therefore must travel a further total distance than the other ions. But while the total distance is longer, the distance increased is in the acceleration region so the ion will also experience a greater acceleration potential. To put some numbers on this, Equation (2.20) can be modified to account for the position shift $L_{\text{acc}} \rightarrow L_{\text{acc}} + \Delta L_{\text{acc}}$:

$$t_{\text{tof}} = \sqrt{\frac{2m}{QE L_{\text{acc}}}} \left(L_{\text{acc}} \sqrt{(1 + \delta)} + \frac{L}{2} \sqrt{\frac{1}{(1 + \delta)}} \right), \quad (2.22)$$

where $\delta \equiv \Delta L_{\text{acc}}/L_{\text{acc}}$. Taylor expanding this about $\delta = 0$ and keeping the first two terms gives us an approximation of t_{tof} . If we enforce the condition that t_{tof} does not vary with

respect to small values of δ , we find that:

$$L_{\text{acc}} = L/2. \tag{2.23}$$

This is known as a first-order time focus and it mitigates the effects of small deviations in starting position as long as the spectrometer is designed so that the length of the accelerating region is approximately half of the length of the drift region.

If a spectrometer is designed according to this condition, an ion slightly behind the starting line will arrive at $L = 2L_{\text{acc}}$ at the same time as an ion that started slightly ahead of the starting line. This is illustrated in Figure 2.7 where, if $L = 2L_{\text{acc}}$, three ions with different starting positions arrive at the time at the detector. Higher order time focus conditions can be derived by keeping more terms in the Taylor expansion, but this increases the complexity of the spectrometer design.

Deviations in ion velocity

The velocities of a group of ions follow a statistical distribution dictated by thermodynamics. The effect of a non-zero velocity along this axis will contribute spatial and temporal deviations. To see why this is, consider that an ion starts with a small velocity $v(t = 0) = v_0$ along the axis of the spectrometer. If v_0 is negative, the ion decelerates in the electric field until it reaches a turn-around point where the velocity is zero. At this point, the ion will behave as a normal ion but it will have a spatial shift as well as a temporal shift. If we compare it to a reference ion that started at rest, the spatial shift can be written as (the spectrometer axis is the x -axis) [118]:

$$\Delta x_0 = -\frac{mv_0^2}{2EQ}. \tag{2.24}$$

The effect of a spatial shift was already discussed above and can be mitigated using a time focusing design. Similarly, the temporal shift of the ion from the starting time of the reference ion would be [118],

$$\Delta t_0 = -\frac{mv_0}{EQ}. \quad (2.25)$$

The time shift can also be represented as measure of the time width of a statistical distribution of ions. Ion velocity follows a Maxwell-Boltzmann distribution where each component of the velocity vector has a normal distribution. Therefore the standard deviation of the time shift of a thermalized group of ions can be written as [121],

$$\Delta t_0^{(\text{std})} = \sqrt{8\ln(2)} \frac{\sqrt{mk_bT}}{QE}. \quad (2.26)$$

This value is often called the ion turnaround time [118] and presents a limiting factor in spectrometer design because it directly contributes to Δt in Equation (2.19) for the mass resolving power.

If we were to design a spectrometer using the first-order time focus constraint provided by Equation (2.23), both components of the spatial deviation would be mitigated. But according to Equation (2.26), the only way to mitigate turnaround time is to lower the temperature T of the ion bunch, or to increase the strength of the electric field E . Increasing the electric field strength will lead to a proportional increase to the kinetic energy spread ΔE_k . Therefore increasing the electric field E contributes to competing interests and we are in a pickle. From a technical standpoint, it is difficult to reduce the ion turnaround time below several nanoseconds [118]. This adds an inherent limitation to the resolving power of a time-of-flight spectrometer.

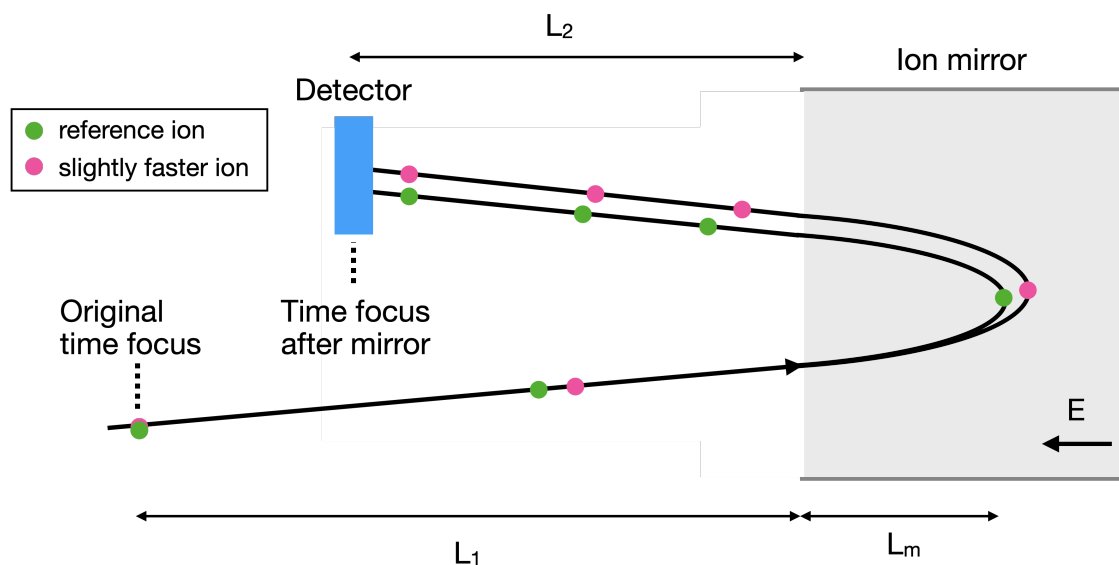


Figure 2.8: An illustration of an electrostatic ion mirror. Two ions of the same m/Q are represented by the green and pink circles entering the ion mirror. Ions with a higher kinetic energy penetrate deeper into the mirror and therefore travel a longer distance. This results in a point after the mirror where the ions can be time focused and where a detector is ideally placed. Figure inspired by [118, 123].

Ion mirrors

A significant development in the design of time-of-flight mass spectrometers was the electrostatic ion mirror. It was first introduced in the Reflectron [122], a time-of-flight mass spectrometer that utilized a single turn to guide the ions onto a slightly off-axis detector. By utilizing a mirror, the reflectron achieved mass resolving powers much higher than the simple linear time-of-flight mass analyzer. This comes down to the ability of the ion mirror to mitigate aberrations due to ion energy spread which is illustrated in Figure 2.8.

The green ion is a reference ion and the pink ion has a slightly higher kinetic energy. They start time focused at a distance L_1 from the ion mirror but as they travel through the field-free zone they are spatially separated. When they enter the potential field of the ion

mirror, the reference ion does not penetrate as deep into the mirror and therefore travels a shorter depth L_m into the mirror. When the ions leave, there is a point at a distance L_2 from the ion mirror where the ions are again focused and this is an ideal place to put the detector. When the detector position is placed at the second time focus, the ion trajectory is called *isochronous* because it is approximately independent of ΔE_k . It is important to stress here that for the best performance, ion mirrors should maintain the isochronicity of the system during a time-of-flight measurement.

Using a similar method of Taylor expanding the time-of-flight about a small shift in kinetic energy, the first-order time focus condition of the ion mirror can be derived [118]:

$$L_1 + L_2 = 4L_m. \quad (2.27)$$

As before, higher-order time focusing of the ion mirror can be achieved by keeping more terms in the Taylor expansion. In practice, this requires the implementation of ion mirrors with multiple electrodes to generate a piece-wise electrostatic field. The implementation of second-order time focusing ion mirrors can help to achieve mass resolving powers in the several thousands [118]. Therefore the ion mirror is a method of mitigating the effect of ion energy spread outside of the ion source or during sample preparation.

2.3.2 Multiple reflection time of flight mass spectrometry

In the previous section we discussed various contributions to time-of-flight aberrations that occur in a simple time-of-flight mass spectrometer. Some of these can be mitigated with the inclusion of an ion mirror and designing the spectrometer according to time focus constraints. However, the ion turnaround time given by Equation (2.26) is a significant constraint for

how small Δt can be made and therefore how large the mass resolving power can be. The other option for increasing the mass resolving power is to increase the total time-of-flight of the ions.

In Table 1.1 we presented the relative mass uncertainty required by various nuclear physics cases with nuclear structure requiring $\delta m/m \approx 10^{-7}$. We can make a simple approximation of the total time-of-flight required to achieve such precision. Assuming that the mass peak measured can be modelled by a Gaussian distribution, the relative mass uncertainty can be written as [119]:

$$\frac{\delta m}{m} = \frac{1}{2\sqrt{2\ln 2}} \frac{1}{\sqrt{N_{\text{ions}}}} \frac{1}{R_m}. \quad (2.28)$$

Assuming the total number of counts gathered for the peak was $N_{\text{ions}} = 500$, the mass resolving power required would be $R_m \approx 190\,000$. If we consider that the minimum turnaround time achievable is about $\Delta t = 5\text{ ns}$ [118], then the total flight time would need to be $t_{\text{tof}} \approx 2\text{ ms}$. For an ion with $A = 50$ and a kinetic energy of $E_k = 1\text{ keV}$, this amounts to a flight distance of about 120 m, which is a sizeable distance for an experimental apparatus.

The multiple-reflection time-of-flight mass-spectrometer (MR-ToF-MS) achieves a longer time-of-flight by folding the flight path upon itself to create a sort of racetrack. This “closed path” design is illustrated in Figure 2.9 where the mass analyzer now consists of two opposing electrostatic ion mirrors to trap the ions. The ions are injected through the left mirror into the mass analyzer, cycled N times⁵ and extracted from the right mirror towards a detector. This is a departure from the typical design of a linear time-of-flight spectrometer and has many benefits some of which are discussed below.

The most obvious benefit to be realized is that the MR-ToF-MS can in principle offer

⁵One cycle is two isochronous turns

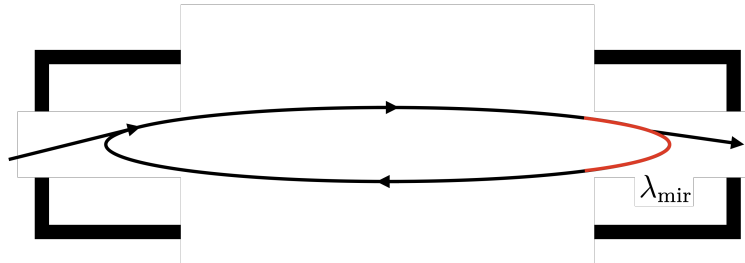


Figure 2.9: An illustration of the “closed path” design of a modern time-of-flight mass analyzer in an MR-ToF-MS. Figure inspired by [118, 123].

an unlimited drift length because the ions can be cycled for an arbitrary number of times in the mass analyzer. Because the flight path is folding upon itself, another benefit of the MR-ToF-MS is a smaller footprint which allows its installation into constrained spaces. In this design, the electrostatic ion mirrors must also allow the passage of ions during the injection and extraction phases of the measurement. To achieve this, the mirror electrode endcap potentials are pulsed which inevitably causes some time-of-flight aberrations. The effects of the voltage ripples during switching can be mitigated by only switching potentials when the ion is positioned far enough away to not feel it. A variable λ_{mir} is defined as the fraction of a full revolution period that the ion spends in the vicinity of the mirrors and is illustrated in Figure 2.9 in red.

Another drawback to consider is that the closed path design is essentially a race track so we must be careful that ions are not “lapping” each other. If they are lapping each other the time-of-flight spectrum will contain mixed-turn species and can be difficult to disentangle. Therefore, in practice mixed-turn species are avoided by limiting the range of masses that can enter the final time-of-flight spectrum. To keep all masses in the time-of-flight spectrum

from the same turn number, the following constraint can be derived [124],

$$\frac{(m/Q)_{\max}}{(m/Q)_{\min}} \approx 1 + \frac{2(1 - \lambda_{\text{mir}})}{N}. \quad (2.29)$$

Therefore as the number of turns N increases, the window of mass range decreases. This means that if a RIB with a wide mass composition were delivered to an MR-ToF-MS, a single mass analysis would not be able to measure the full mass spectrum while simultaneously reaching high mass resolving power. TITAN's solution to this problem is described in Chapter 3.

The total time-of-flight of the ions for an MR-ToF-MS is,

$$t_{\text{tof}} = t_{\text{tfs}} + N_{\text{it}}t_{\text{it}}, \quad (2.30)$$

where N_{it} represents the number of isochronous cycles in the mass analyzer and t_{it} is the time-of-flight for each cycle. t_{tfs} represents the time-of-flight required if the ion were to travel to the detector without any turns. The mass resolving power for an MR-ToF-MS is given by [120]:

$$R_m = \frac{m/Q}{\Delta(m/Q)} = \frac{t_{\text{tfs}} + N_{\text{it}}t_{\text{it}}}{2\sqrt{\Delta t_{\text{ta}}^2 + \Delta t_{\text{tfs}}^2 + (N_{\text{it}}\Delta t_{\text{it}})^2}}. \quad (2.31)$$

Δt_{ta} represents the turnaround time due to kinetic energy spread of the ions during initial injection into the mass analyzer. Δt_{tfs} represents the time spread due to aberrations when the ion is passed through the analyzer without any turns. Δt_{it} is the time spread contributed by aberrations during each turn in the mass analyzer. In the limit that $N_{\text{it}} \rightarrow \infty$, Equation (2.31) is asymptotic of the form,

$$R_m \approx \frac{t_{\text{it}}}{2\Delta t_{\text{it}}}. \quad (2.32)$$

Hence, at high enough turn numbers, mass resolving power is approximately independent of the turnaround time. Therefore, the mass resolving power is limited by how small Δt_{it} can be made by good ion mirror design. The minimization of ion mirror aberrations is beyond the scope of this thesis.

Before moving on, the classic relation between the ion mass and the time-of-flight for a simple linear spectrometer given by Equation (2.18) can be updated for an MR-ToF-MS to [120],

$$\frac{m}{Q} = \frac{c(t_{\text{exp}} - t_0)^2}{(1 + bN_{it})^2}, \quad (2.33)$$

where the new parameters b , c , and t_0 account for shifts in the specific experimental device. These are calibrated before a measurement using a reference ion.

Chapter 3

Overview of the experimental facilities

This thesis work was performed at Canada’s particle accelerator centre, TRIUMF, located in Vancouver, British Columbia. Because this thesis covers two different main topics, this chapter introduces the experimental facilities required for both of them. This took place at TRIUMF’s Ion Traps for Atomic and Nuclear science facility (TITAN), which operates multiple ion traps aimed at answering questions at the forefront of nuclear physics research. The first section discusses the production of Radioactive Ion Beams (RIB) via TRIUMF’s Isotope Separator and ACcelerator (ISAC) facility [125]. The next section discusses the TITAN facility and introduces the radiofrequency quadrupole (RFQ) cooler-buncher, which prepares RIB for injection into any of TITAN’s ion traps. The last sections introduce the Multiple-Reflection Time-of-Flight Mass Spectrometer (MR-ToF-MS) for precision mass measurements at TITAN, and the Electron Beam Ion Trap (EBIT) which is the foundation for in-trap decay spectroscopy at TITAN.

3.1 The TRIUMF cyclotron and the ISAC facility

At the heart of the TRIUMF laboratory is an ion source which produces H^- (1 proton, 2 electrons) ions for the TRIUMF cyclotron. The cyclotron accelerates the H^- ions in an outward spiraling trajectory using a high frequency alternating electric field and a six-piece sectioned magnet for beam confinement. At the edge of the cyclotron, thin graphite foils are used to strip the electrons and the resulting beam of protons are guided onto a beamline. The TRIUMF cyclotron is able to operate up to four different proton beams concurrently with energies ranging from 70 – 520 MeV with up to 300 μA of particle beam current [126].

Up to 100 μA of beam current can be delivered to the ISAC facility [127], which produces RIB via the well-known Isotope Separation On-Line (ISOL) method [13]. In this

method, thick targets are irradiated with the driver beam of highly energetic protons to induce spallation, fragmentation, and fission reactions [128]. Due to the thickness of the targets, the nuclei produced are stopped in the bulk material and must diffuse out before they can be ionized and formed into an ion beam. To encourage diffusion of the nuclei out of the bulk material and desorption from the surface, the target and target container are both heated to temperatures ranging from 2200 – 2400 °C. A number of different target materials are available for RIB production such as SiC, TiC, ZrC, UC_x, Nb, and Ta [129].

At ISAC, the ion sources are closely coupled to the targets to minimize production losses [128]. Figure 3.1 illustrates the target geometry with a coupling to the hot surface ion source. After the neutral atoms are released from the target, they diffuse through a transfer tube towards a hot cavity. In this cavity, they adsorb onto the hot surfaces and are ionized. The hot surfaces are typically made from a low work function refractory metal such as tantalum or rhenium. This allows a high affinity for “stealing” the electron from the atom to form a positively charged ion. Downstream from the hot cavity is an electrode structure that is used to extract the ions as a RIB as a continuous beam. This technique works efficiently to produce singly charged ions when the ion’s ionization potential is below approximately 6 eV [128].

For species with higher ionization potentials, TRIUMF’s Resonant Ionization Laser Ion Source (TRILIS) is available [131]. For this technique, lasers are frequency tuned and focused into the target cavity. These lasers excite the neutral atom into an autoionizing state which spontaneously ionizes to form a positively charged ion. The specific advantage of this method is that the lasers can be frequency tuned to selectively ionize species of interest while leaving undesirable species (i.e. beam contaminants) as neutrals. TRILIS shares the same target-ion source geometry as the surface ionization source and provides the benefits of higher

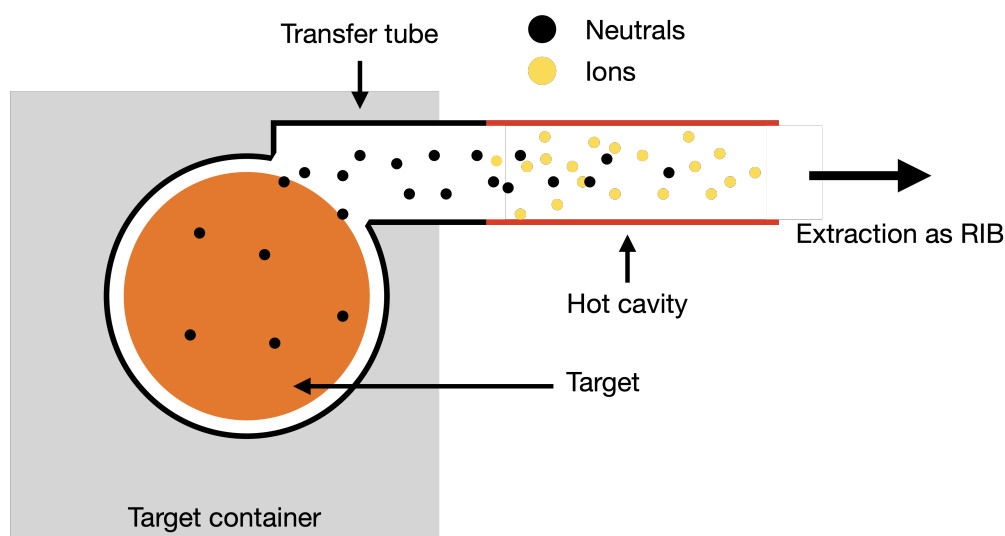


Figure 3.1: An illustration of the target and ion source geometry using the hot cavity surface ionization source. Illustration inspired by [130]

ionization efficiency and element selective ionization. Depending on the element, a number of laser ionization schemes are available¹.

Two other ionization sources are available, but were not used for this experiment. The Ion Guide Laser Ionization Source (IG-LIS) is specially designed to reap the benefits of TRILIS while simultaneously reducing surface ionized contaminant ions. This is achieved with an additional electrode that repels contaminant ions effusing from the target container and has demonstrated a seven orders of magnitude decrease in contaminants [132]. For species with very high ionization energy, a Forced Electron Beam Induced Arc Discharge (FEBIAD) ion source is available.

The ions are extracted from the ion source and accelerated as a RIB into ISAC's two-stage mass separator. The first stage is a pre-separator dipole magnet which acts as a cleaning stage to remove most contamination. The second stage is the high-resolution mass separator

¹See the [ISAC yields database](#)

magnet which can achieve a resolving power of $m/\Delta m = 2000$ [128]. This is sufficient to deliver a specific m/Q to TITAN, but insufficient to remove isobaric contaminants. A schematic depiction of the ISAC facility is given in Figure 3.2.

ISAC-I and ISAC-II Facility

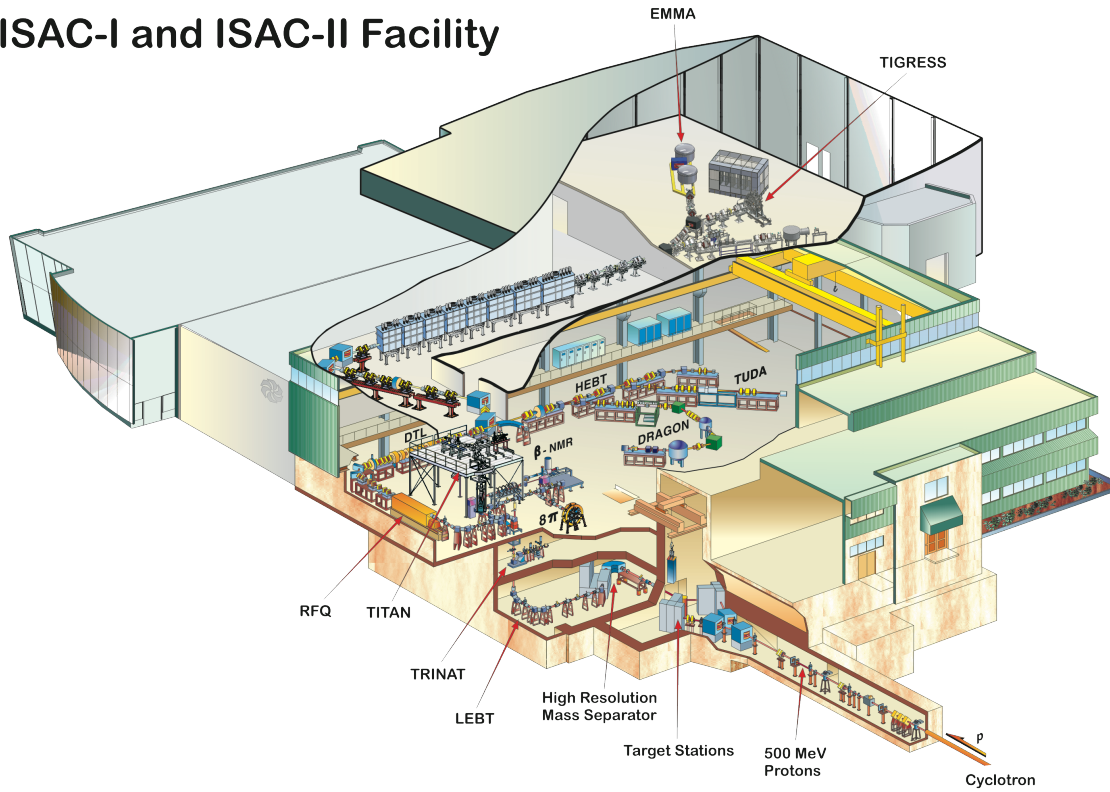


Figure 3.2: A schematic overview of the ISAC-I and ISAC-II facilities. The high energy proton beam is extracted from the cyclotron (not shown) into the ISAC target station for RIB production. After RIB production the ISAC mass separator sends a specific m/Q to downstream experiments. Figure from [133].

3.2 The TITAN facility

ISAC produces RIBs for experiments that are located in two experimental halls, ISAC-I and ISAC-II. TITAN is located in the low-energy section of ISAC-I. After beam purification by

the ISAC mass separator the RIB is delivered at 20 keV beam energy along the low-energy beamline to the ISAC-I experimental hall where TITAN is located on a raised platform. The TITAN experimental setup was originally developed to be capable of high precision mass measurements of short-lived nuclei via Penning trap spectroscopy coupled with highly-charged RIBs produced by the EBIT [134]. However, the capabilities of TITAN have grown over the years with the addition of the MR-ToF-MS and the advantages provided by an EBIT that can be used for nuclear decay spectroscopy. TITAN is therefore positioned to run unique experiments with impact on a wide breadth of topics in nuclear physics and nuclear astrophysics.

There are currently four ion traps in operation at TITAN:

Radiofrequency Quadrupole (RFQ) cooler-buncher: The RFQ cooler-buncher cools and bunches the continuous RIB received from ISAC in preparation for TITANs downstream measurement traps [135].

Electron Beam Ion Trap (EBIT): The EBIT breeds singly charged ions into highly charged ions (HCI) for in-trap decay spectroscopy and high precision mass measurements at MPET [136].

Multiple-Reflection Time of Flight Mass Spectrometer (MR-ToF-MS): The MR-ToF-MS uses the time-of-flight principle for precision mass measurements and can also provide isobaric purification of the RIB for other measurement traps [46].

Measurement Penning Trap (MPET): The MPET uses Penning trap mass spectroscopy for precision mass measurements [116, 117].

These devices can operate standalone or in concert with one another to achieve a desired experimental goal. An illustration of the TITAN facility is displayed in Figure 3.3. The

following sections give an introduction to the RFQ cooler-buncher, the EBIT, and the MR-ToF-MS because they were used for this thesis work.

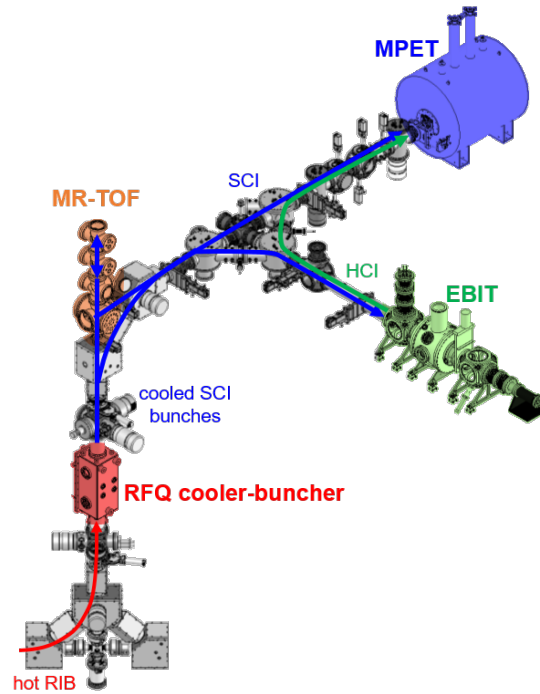


Figure 3.3: An illustration of the TITAN facility showing the four ion traps. The RFQ Cooler-Buncher prepares the continuous RIB from ISAC for injection into the three downstream traps.

3.2.1 Radiofrequency quadrupole cooler-buncher

The RFQ cooler-buncher is the gatekeeper to the TITAN facility and optimizes the RIB for injection into the measurement traps. From ISAC, the continuous RIB is delivered at 20 keV to TITAN using the Low Energy Beam Transport line. Generally speaking the measurement traps at TITAN require RIB that is bunched rather than continuous, with low energy spread, and at low energy. As such, the beam is first decelerated upon entry to the RFQ cooler-

buncher by floating the device at a potential a few tens of eV below the beam energy. The beam is accumulated and cooled and then accelerated at ~ 1.3 keV into the TITAN beamline.

Cooling of the RIB is achieved through collisions of the ions with an inert helium buffer gas that fills the trap to an approximate pressure of 1×10^{-2} mbar. These collisions act as a “buffer” to absorb the kinetic energy of the ions until the temperature of the ion bunch comes into thermal equilibrium with the buffer gas. A side effect of the gas cooling mechanism is an induced dispersion of the ion beam. This dispersion is counteracted with radial forces provided by a square-wave-driven radio-frequency field applied to the quadrupole electrode structure. The trap structure is longitudinally segmented into 24 electrodes and electric DC capture potentials are applied to these electrodes in order to accumulate the continuous RIB as it cools. A different potential configuration is then applied to the electrodes to extract ion bunches from the RFQ into the TITAN beamline. This is schematically illustrated in Figure 3.4.

The RFQ can also provide stable ions to the measurement traps via the TITAN Ion Source (TIS). TIS is a hot surface ionization source, which provides alkali metals such as rubidium and potassium. These stable ions are used for optimizing beam injection into measurement traps, tuning measurement cycles, and calibration during experiments.

3.3 The multiple-reflection time-of-flight mass spectrometer

When deciding on a mass spectrometer to install at a RIB facility, some of the most important requirements are a high mass resolving power, a fast measurement cycle for short-lived nuclei, and a high enough sensitivity to deal with low signal-to-background ratios. Depending on

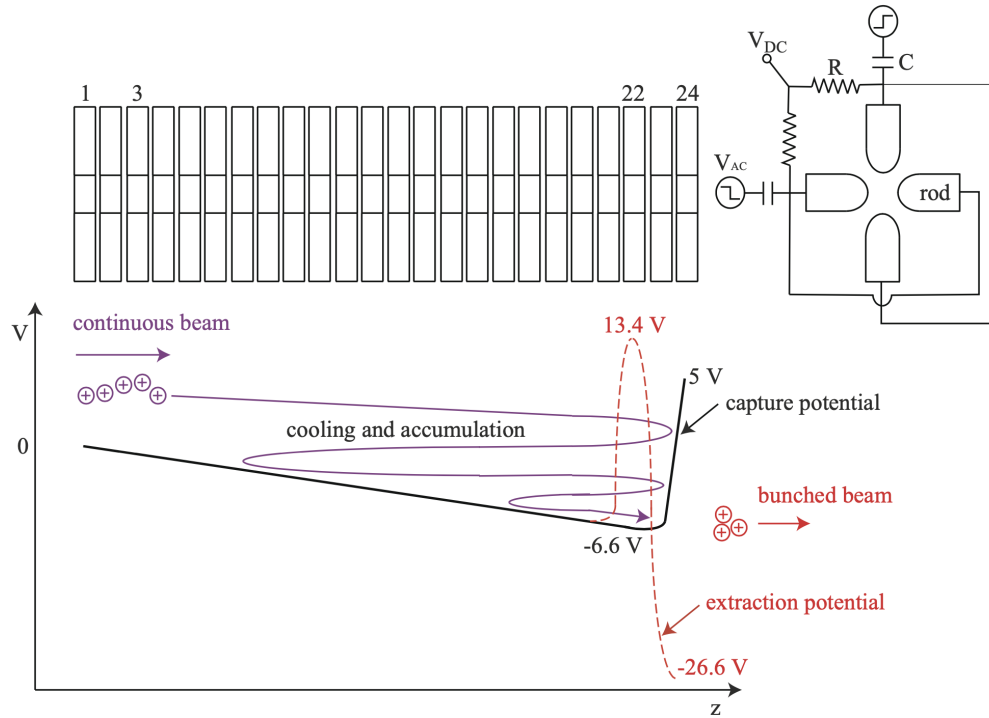


Figure 3.4: (top) An illustration of the segmented electrodes of the RFQ cooler-buncher. (bottom) The longitudinal drag potentials applied to the electrodes allows cooling and accumulation of the continuous RIB at the potential minimum for extraction. The dashed line indicates the potential that is used to extract the RIB into the TITAN beamline. Image from [135].

the requirements, a number of different types of mass spectrometers can be used. For isotope discovery and mass measurements of isotopes with half-lives shorter than $\sim 1\text{ ms}$, storage ring isochronous mass spectrometry (IMS) at in-flight facilities is a preferred method [137]. For the highest mass resolving power and studies of fundamental symmetries, Penning trap mass spectrometry is preferred [17].

However, both of these methods have their own respective drawbacks for mass measurements of the short-lived nuclei near proton and neutron drip lines. While IMS measurement cycles are fast enough to reach very short half-lives, they have historically

suffered from systematic uncertainties limiting the mass precision to $\delta m/m \approx 10^{-6}$ which borders requirements for nuclear astrophysics and structure. Penning traps have the highest mass resolving power, but the required measurement time scales linearly with m/Q and they have a low sensitivity for the ion of interest if high background contamination is present [119]. MR-ToF-MS fills a vacancy between these two methods by offering the fast measurement cycles needed to measure isotopes with a few ms half-lives, a high sensitivity to low production yields of the isotope of interest, and enough mass resolving power to study nuclear structure and nuclear astrophysics [119]. Because of this, MR-ToF-MS devices have been installed at RIB facilities worldwide [119, 138–140].

The original proposal for the TITAN facility saw the Penning trap as the provider of precision mass measurements [134]. While TITAN's MR-ToF-MS cannot reach the same mass resolving power as MPET, its advantages are in many ways complementary to the scientific program at TITAN. The TITAN MR-ToF-MS was built at the Justus-Liebig-University Gießen and commissioned at TITAN in 2017 [46]. The design is based on the highly successful MR-ToF-MS installed at the Fragment Separator (FRS) Ion Catcher at GSI in Darmstadt, Germany [121]. It is the first trap downstream of the RFQ and functions for two main purposes at TITAN: 1) as a standalone experimental device for precision mass measurements and 2) as a beam purification device for the other measurement traps.

Already since the commissioning of the MR-ToF-MS at TITAN, its benefits have been well demonstrated [47]. The ability to perform fast measurement cycles for measurements of short-lived nuclei was recently demonstrated with the observation of the $^{125\text{m}2}\text{In}$ isomeric state which has a 5.0(1.5) ms half-life [141]. The highest mass resolving power reached with the TITAN MR-ToF-MS is a mass resolving power of $R_m > 600,000$, which was used to

resolve the 220 eV isomer $^{69\text{m}}\text{Fe}$ from its ground state [142]. The device is also able to isolate and suppress contaminant ions up to 10^6 times higher than the species of interest by acting as its own isobaric cleaner [47]. The device also has a large mass range window which makes it particularly useful for performing ISAC yields measurements and assisting in the optimization of RIB delivery [143].

The MR-ToF-MS is comprised of two major sections, the ion transport system and the mass analyzer. Figure 3.5 identifies these sections as well as other important pieces of the trap. Below is a brief discussion of the MR-ToF MS design and features. For a more detailed discussion refer to [47, 144].

3.3.1 Ion transport system

The first section of the MR-ToF-MS is a uniquely designed ion transport system used to facilitate efficient transfer of ions to and from the time-of-flight mass analyzer at low energies (~ 1 keV). The system is composed of linear RFQ's which surround an RFQ switchyard at the heart of the system. Each of the linear RFQ's are constructed with four resistive plastic rods (resistance is $\sim 5\Omega/\text{cm}$) which allow the creation of linear drag potentials to transport ions through the system. These potentials are created by applying static voltages to the ends of each rod. Between each RFQ are biased apertures that can be used to store the ions.

At the intersection of the RFQ traps is the uniquely designed RFQ switchyard, which receives and transports the ions in any direction [145]. The switchyard also receives stable calibration ions from a thermal ion source and merges them with the RIB for injection into the mass analyzer. Above the RFQ switchyard is another linear RFQ for efficiently transporting the ions into the injection trap. The injection trap provides optimal conditions for injection of the ion bunch into the mass analyzer. The switchyard is also used to facilitate

delivery of isobarically clean RIB to other measurement traps when MR-ToF-MS is being used as an isobaric purifier.

Similar to the TITAN RFQ cooler-buncher, the MR-ToF-MS ion transport system also uses a buffer gas to cool the ions as they are transported to the mass analyzer. The accumulation and cooling procedure occurs at two points in the system, once just before the RFQ switchyard and once again just before the injection trap. Each of the cooling stages last on the order of ~ 1 ms. At the point of injection into the mass analyzer, it has been estimated that the mean kinetic energy is 1300 eV with an energy spread of 17 eV [47].

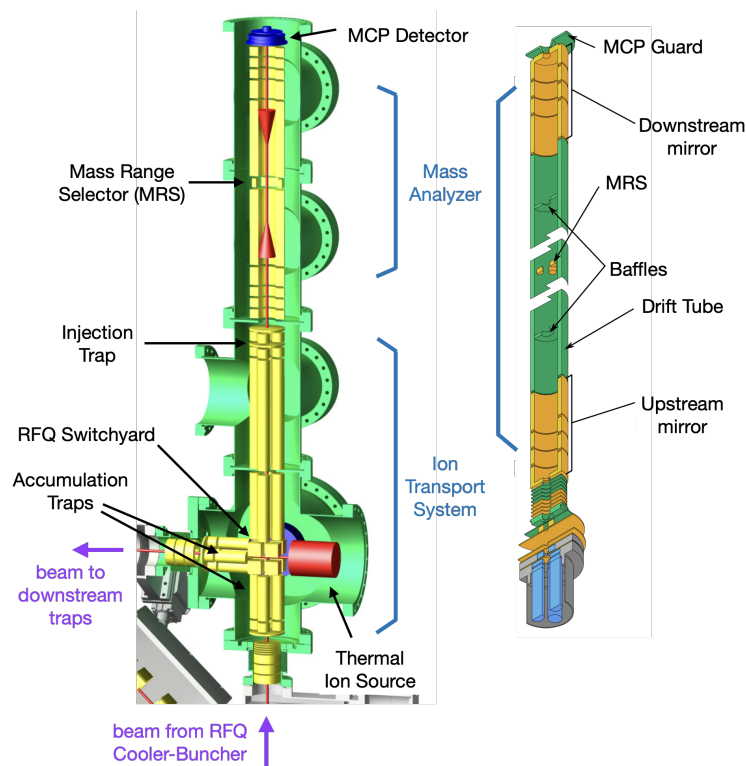


Figure 3.5: (left) Schematic of MR-ToF-MS with major sections labelled and (right) a detailed close-up of the Mass Analyzer. See references [47,144] for more details on individual MR-ToF-MS components and their functioning properties. Modified from [46] and [144].

3.3.2 Mass analyzer

The right side of Figure 3.5 gives a detailed look at the electrode structure of the mass analyzer. It is a symmetrical assembly consisting of two inward-facing ion mirrors connected by a grounded drift tube. Each mirror is composed of an endcap electrode and three ring electrodes. The endcap electrodes are pulsed to allow for injection and extraction of ions. At the center of the grounded drift tube is a four electrode structure known as the Mass Range Selector (MRS). The primary function of the MRS is to deflect the trajectories of ions into the baffles. This is used to limit the mass range of ions that are recorded into the final time-of-flight spectrum so that mixed-turn species are not recorded unless desired. At the far end of the mass analyzer behind the second mirror is a single ion detector (ETP MagneTOF™) used for recording the ion time-of-flight.

3.3.3 MR-ToF-MS Operation

The MR-ToF-MS can operate as a standalone mass measurement device or as a preparation device to remove isobaric contaminants from RIB's for measurements at other traps. During either of these modes, it is important that the MR-ToF-MS maintains isochronicity.

For the MR-ToF-MS to maintain isochronous operation during a regular time-of-flight analysis, we must make sure that the ions are time focused at the detector for the time-of-flight measurement. To achieve this, the time focus of the ions are aligned using a dynamic time focus shift (TFS) method [146], which is illustrated in Figure 3.6. This method uses slight shifts to the mirror electric potentials at different points during the time-of-flight analysis to move the time focus point. When the ions are first released from the injection trap into the analyzer, there is a point known as the first time focus where all ions of a given m/Q arrive at approximately the same time regardless of a small kinetic energy spread. The

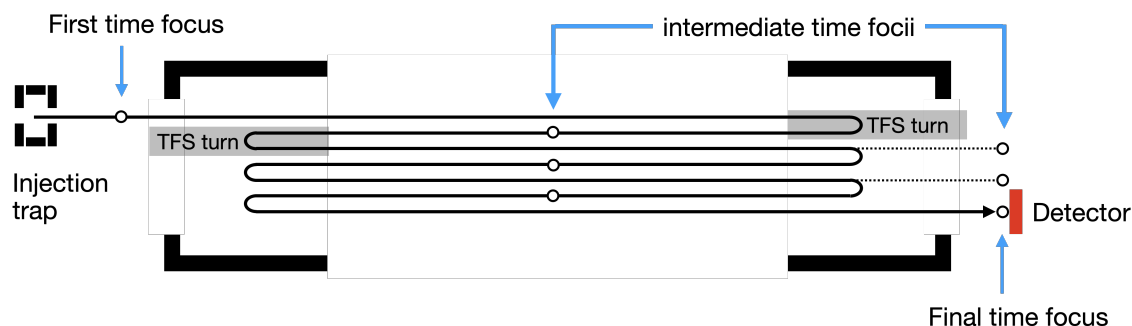


Figure 3.6: An illustration of the time-of-flight analyzer’s dynamic time-focus shift method used to ensure the time-of-flight measurement is isochronous [146]. Illustration inspired by Figure 1d from [146].

first turn in the analyzer is a TFS turn from the exit mirror which shifts the time focus of the ions to the center of the mass analyzer where the MRS is located. The second turn from the entrance mirror is also a TFS turn which shifts the time focus of the ions onto the MagneTOF detector. After these TFS turns, the mirrors are switched into isochronous mode where the time foci are maintained regardless of the number of turns taken in the analyzer. The more isochronous turns that are completed, the higher the mass resolving power of the measurement. After the desired number of turns are completed, the time-of-flight of the ions are recorded by opening the exit mirror and releasing them onto the MagneTOF detector.

During the time-of-flight measurement, the MRS at the center of the analyzer is used to deflect leading and trailing ions so that the final spectrum contains only species from a single number of turns. When the MRS is used, it is typically only engaged for the first 20 – 50 turns in the mass analyzer. It is sometimes desirable to use a technique called *beam merging* which tunes the MRS to allow only specific multi-turn species into the spectrum. This is particularly useful when injecting a stable calibration ion with a different m/Q than the ion of interest. However, care must be taken when using this method because it can lead to a

crowded spectrum if the m/Q from different turn numbers start to overlap.

To enhance the sensitivity of measurements in situations with low signal-to-background ratios, the MR-ToF-MS can be operated in a mass-selective retrapping mode [147]. This allows the device to operate as its own isobaric mass purifier before performing a time-of-flight analysis. When operating in this mode, the ions are injected into the mass analyzer following the exact same settings outlined above for a normal time-of-flight analysis. The ions are cycled for a desired number of turns to spatially separate contaminants from the ion of interest. After the desired isobaric separation is reached, the exit mirror potentials are adjusted to shift the time focus onto the injection trap and the entrance mirror is opened. This allows the ions to be released back into the injection trap where fast switching potentials are used to capture the ion of interest while rejecting contaminant species. After a cooling period of a few ms, the ions are released back into the mass analyzer for a routine time-of-flight analysis.

In the case that the MR-ToF-MS is being used as an isobaric purifier for down stream traps, the scheme is similar to the mass-selective retrapping mode but without the second cycle. After the isobaric separation cycle, the ions are released back into the injection trap where they are subsequently transported to the RFQ switchyard and then the downstream traps. The separate stages of MR-ToF-MS operation are illustrated in Figure 3.7. For a regular mass measurement, the stage order is 1 – 2 – 3*b*. For a mass measurement with mass-selective retrapping, the stage order is 1 – 2 – 3*a* – 3*b*. For isobaric separation and delivery to other measurement traps, the stage order is 1 – 2 – 3*a*.

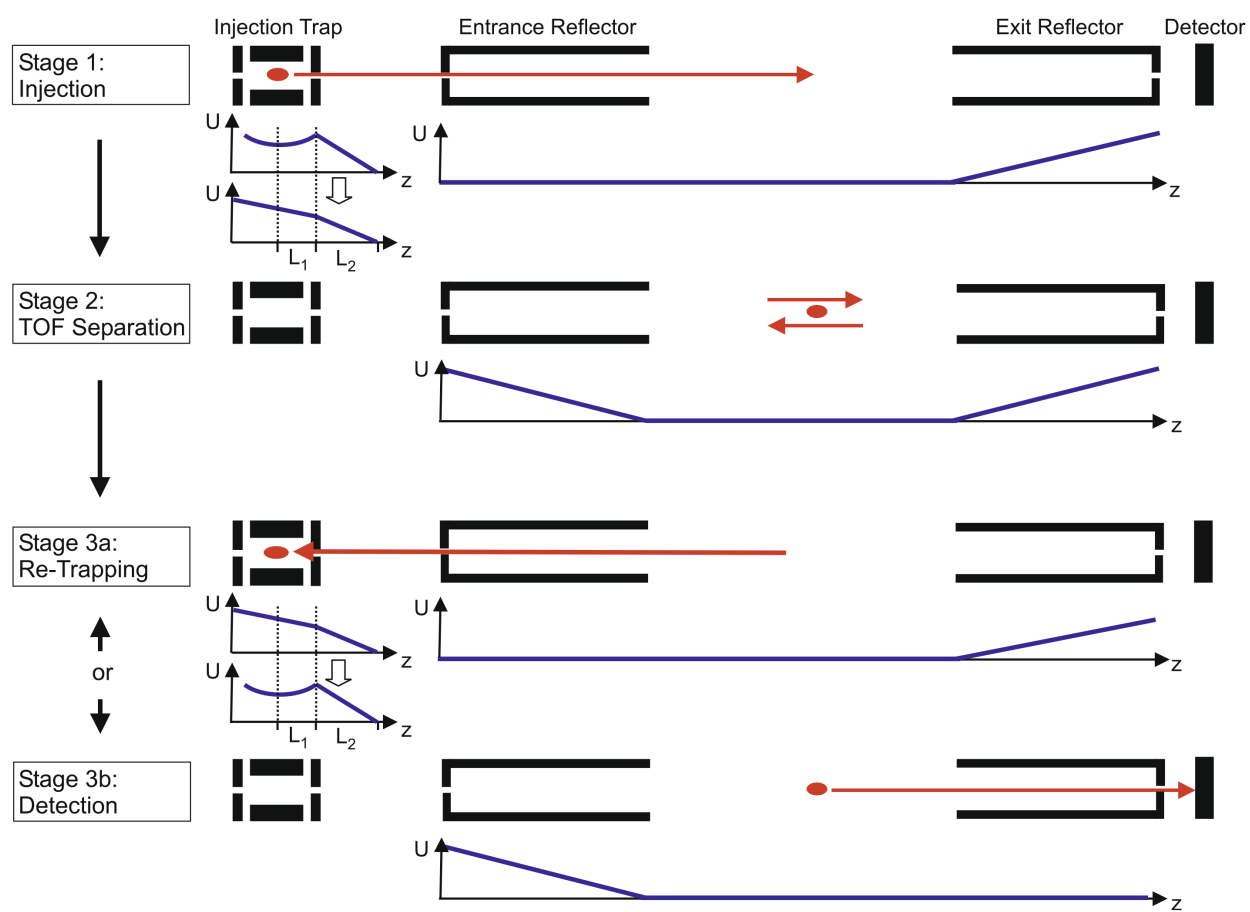


Figure 3.7: An illustration showing the separate stages of MR-ToF-MS operation. Illustration from [147].

Chapter 4

Mass measurements of neutron-deficient strontium and lanthanides

4.1 Introduction

This chapter presents the experiment S1615LOI, titled “Precision Mass Measurements of Neutron-deficient Sr Nuclei”, as well as the data analysis and results. For this experiment, a $50\ \mu\text{A}$, $500\ \text{MeV}$ p^+ beam was driven onto a niobium target to produce the strontium ions of interest, $^{74-76}\text{Sr}$. To enhance the signal-to-background ratio, the strontium ions were selectively ionized using the TRILIS lasers [131]. As a reminder, the TRILIS lasers perform selective ionization in the ionization cavity which is closely coupled to the RIB production target. This selective ionization was performed as a two-step (blue-blue) laser excitation scheme into an autoionizing state [148, 149]. The ions were then formed into a RIB and sent to the ISAC mass separator system to be A/Q selected with a resolution of approximately $1\ \text{u}/Q$. The requested RIB was delivered at $20\ \text{keV}$ into TITAN’s RFQ cooler-buncher. After cooling and bunching, RIB bunches were extracted and lowered to $1.3\ \text{keV}$ transport energy using a pulsed drift tube and supplied to the MR-ToF-MS at 50 bunches per second. The MR-ToF-MS was also operated at a repetition rate of $50\ \text{Hz}$.

A significant contributor to the background in the strontium spectra was due to the presence of heavy lanthanides ($Z = 57 - 70$). Because reaction products are created by spallation, fragmentation and fission reactions in the target material, these lanthanides were not produced by the niobium ($Z = 41$) target but were in fact produced by the tantalum ($Z = 73$) target holder which incidentally received some of the proton beam. Because of the low ionization potential, a fraction of these lanthanides were produced in the $Q = 2+$ charge state and therefore fell within a similar m/Q range as the strontium ions.

TITAN used this opportunity to perform additional mass measurements of ^{145}Tb , ^{146}Tb and ^{148}Ho . The following sections outline the overall measurement procedure, the analysis technique, and the final values obtained for both the neutron-deficient strontium and the

heavy lanthanides.

4.2 Measurement procedure

The measurement procedure at each A/Q was generally the same. First, a broadband mass acquisition was performed at a relatively low turn number and without the mass-selective re-trapping function. This is typically known as a “beam composition” measurement and is used to identify species in the spectrum so that a plan for the precision measurement of the ion of interest can be developed. If the ion of interest was clearly resolved, we tuned the MR-ToF-MS to a higher turn number to obtain the highest resolving power and performed a measurement. If the ion of interest was not seen, we attempted to increase the signal-to-background ratio until it was resolved. Typically the first method for this was to apply small changes in the ISAC magnet separator settings to ensure that it was centered on the ion of interest and not on a contaminant species. We also used the mass-selective re-trapping function to specifically cut out contaminant ions from the spectrum. By reducing the rate of contaminant species, the MR-ToF-MS was able to receive a higher intensity of RIB from ISAC which increased the rate of the ion of interest.

When setting up the MR-ToF-MS for a time-of-flight analysis, we also kept track of what species in the spectrum could be used for calibration. Ideally the RIB provided a native species that was well-resolved and with a well-known literature mass. In the case that no suitable calibrant peaks were present, the mass range selector (MRS) was setup to allow specific multi-turn species into the spectrum. Using what’s known as the *beam merging* technique, we injected calibrant species into the spectrum using the MR-ToF-MS internal ion source.

For the measurements performed in this thesis, the mass-selective re-trapping function was used at every mass unit. A range of 20 – 100 re-trapping turns were required to improve the signal-to-background ratio and a range of 756 – 842 turns (total ToF $\approx 11.7 - 13.1$ ms) were used for the time-of-flight analyses. Generally speaking, the mass-selective re-trapping mode allowed a factor of 10 – 100 higher beam intensity to be delivered to TITAN while suppressing contaminants and maintaining an overall count rate of < 1 pps at the MR-ToF-MS. Figure 4.1 illustrates the effect of mass-selective re-trapping in the ^{76}Sr measurement. The first spectrum without re-trapping used 846 measurement turns and demonstrated a signal-to-background ratio $^{76}\text{Sr}:^{76}\text{Rb} \approx 0.0023$. The second spectrum was performed with identical MR-ToF-MS settings, but included 100 re-trapping turns before the 846 measurement turns. This allowed TITAN to take a factor 10 more beam intensity from ISAC and demonstrated a much higher signal-to-background ratio with $^{76}\text{Sr}:^{76}\text{Rb} \approx 0.15$.

The spectrum shown in Figure 4.1 also demonstrates the beam merging technique to inject ^{85}Rb into the spectrum. Because ^{85}Rb is heavier than the A/Q where the measurement was performed, the MRS was specifically tuned to let it through. For $A/Q = 76$, the mass measurement was performed with 846 isochronous turns, and the MRS let ^{85}Rb through at 756 isochronous turns. ^{85}Rb was injected after the mass-selective re-trapping phase and therefore not affected by the re-trapping function.

The strontium ions of interest were unambiguously identified using resonant laser ionization with the TRILIS ion source. At each mass unit we recorded two different time-of-flight spectra, one with the TRILIS lasers blocked and one unblocked. Because the lasers were specifically tuned to ionize only strontium and leave other contaminants neutralized, this provided strong support that the peak affected by the laser toggling was

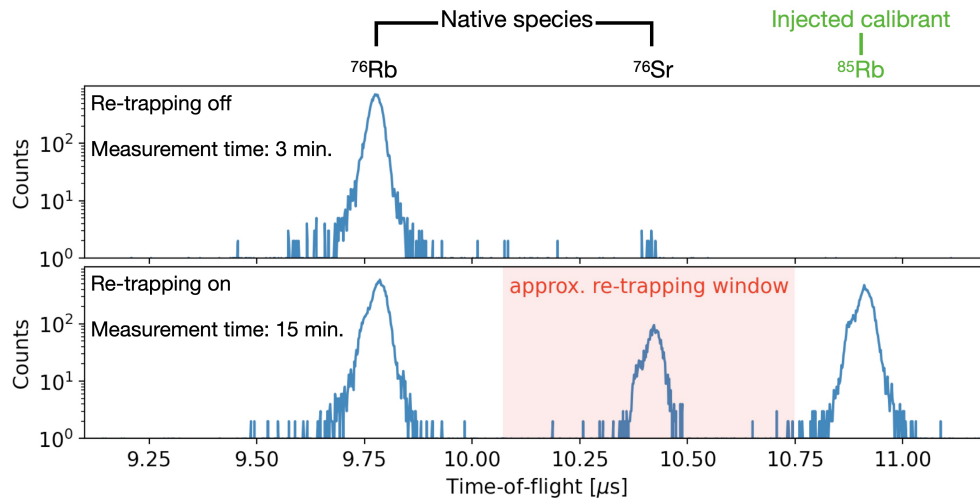


Figure 4.1: A raw spectrum of the $A = 76$ mass acquisition illustrating both the effect of mass-selective re-trapping and the beam merging technique. The top plot shows a broadband spectrum of the RIB which contained ^{76}Sr and ^{76}Rb . In the bottom plot, the re-trapping window was setup to increase the rate of ^{76}Sr with respect to ^{76}Rb . The calibrant ^{85}Rb was injected via the internal ion source and is not affected by the re-trapping procedure.

indeed strontium. Figure 4.2 shows a raw spectrum at $A/Q = 74$ where the laser toggling can be seen to only affect the strontium peak.

4.3 Analysis

The software used to acquire the time-of-flight spectra during the experiment is a collaboratively developed program called Mass Acquisition (MAc) [150]. MAc was also used to perform an initial part of the data analysis. In order to convert the time-of-flight data to mass values, we used Equation (2.33) which is reproduced here:

$$\frac{m}{q} = \frac{c(t - t_0)^2}{(1 + bN_{it})^2}, \quad (4.1)$$

where t_0 is the time delay due to electronic latency, c is a proportionality parameter, and b represents the difference between a no-turn time-of-flight analysis and a N_{it} turn time-of-flight analysis. Because the electronics and cabling of the system were not changed during the measurement, t_0 is considered a constant. The b and c parameters are fully correlated so c is kept a constant while allowing b to be time-dependent (see Section 4.3.1). t_0 and c are determined prior to the experiment using a zero-turn calibration with two species of well-known mass.

4.3.1 Time-resolved mass calibration

Low frequency fluctuations in the mirror voltages and thermal expansion in the mass analyzer cause a drift in an ion's time-of-flight during the N_{it} turns and limit mass resolution. Because of this, the b coefficient is considered time-dependent and is used to correct for these fluctuations. The effects of these fluctuations can be seen in the spectrum

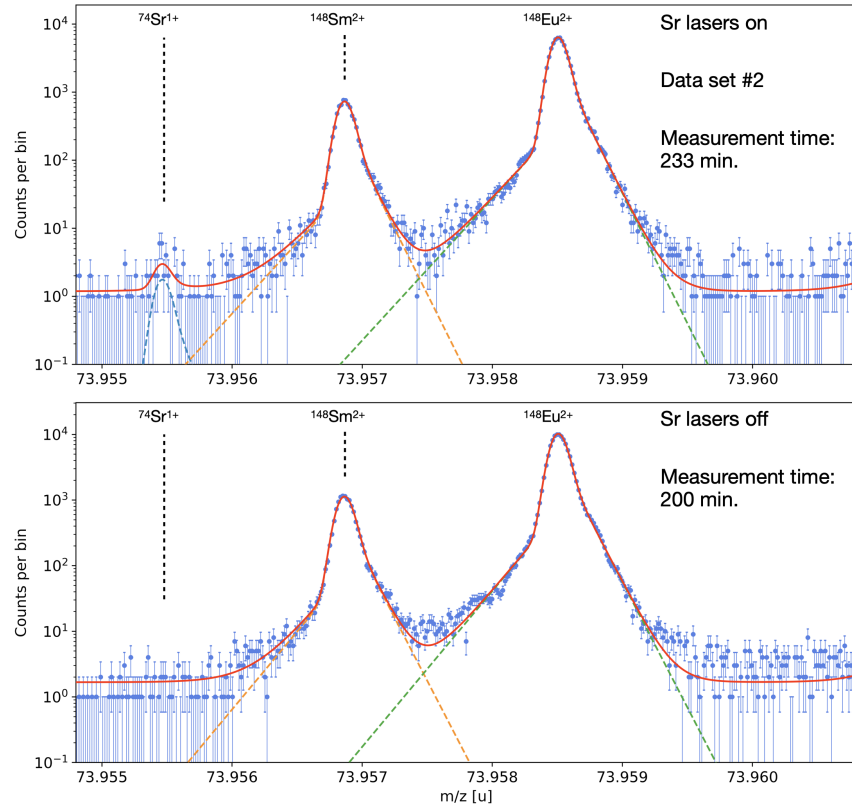


Figure 4.2: Mass spectra acquired at $A = 74$ with (top) and without (bottom) resonant laser ionization of strontium. The spectra have been drift corrected using the time resolved calibration (TRC) procedure (see Section 4.3.1) and fitted using the procedure outlined in Section 4.3.2. Error bars shown are $\pm 1\sigma$ assuming Poisson statistics in each bin. Multi-peak fits to the data (solid red line) and the underlying single peak fits (dashed lines) are indicated.

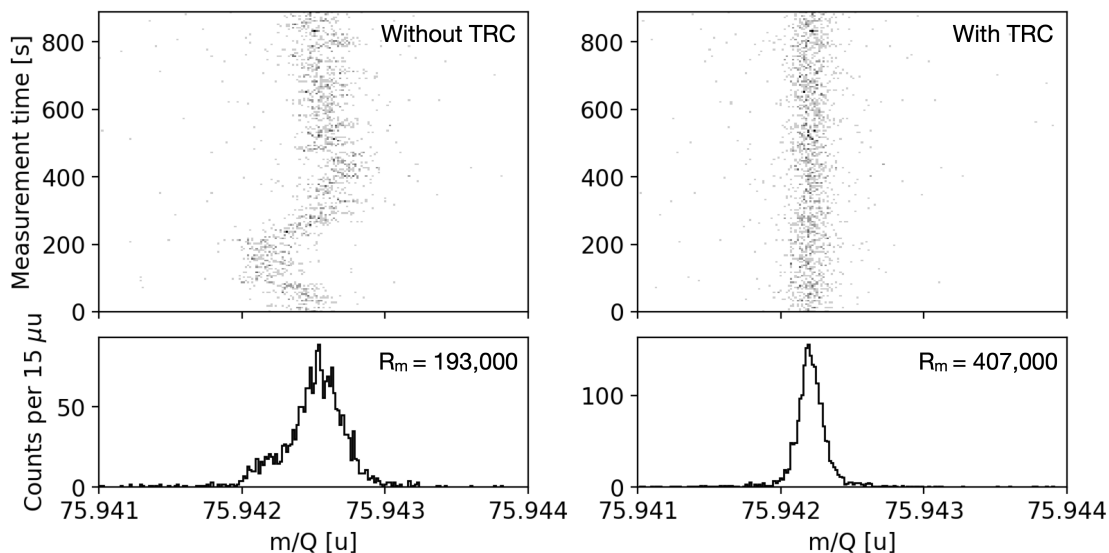


Figure 4.3: Drift correction of ^{76}Sr due to the TRC procedure. The bottom panels show a 1D histogram of the ^{76}Sr peak before and after TRC. The top panels show 2D histograms of the ^{76}Sr peak being accumulated over the time of the measurement before and after TRC.

shown on the left side of Figure 4.3 where the peak is broadened and shows a shoulder on the left side of the peak maximum. Therefore, the first step of data analysis was to correct for this by performing a time-resolved calibration (TRC). To perform a TRC, a reference peak with consistently high statistics throughout the measurement and a well-known literature mass was chosen. Then the full time-of-flight spectrum as a function of the measurement time was broken into small blocks of measurement time. At each block, the reference peak was fit with a Gaussian distribution. The centroids of each fit in a time block were then aligned to the literature mass of the reference peak by adjusting the b parameter. After this procedure, all of the blocks were stitched back together to arrive at the fully drift-corrected time-of-flight spectrum. As can be seen in Figure 4.3, application of the TRC more than doubled the ^{76}Sr mass resolving power from $R_m = 193,000$ to $R_m = 407,000$.

4.3.2 Peak shape models for curve fitting

The next part of the analysis was to determine a suitable peak for curve fitting the peaks in the spectrum. The mass spectrum was exported from MAc as a CSV and then analyzed with the in-house developed emgfit Python package [151]. This package uses non-linear least-squares minimization to fit hyper-Exponentially Modified Gaussians (Hyper-EMG) which have been specifically developed for asymmetric high-resolution MR-ToF-MS peak shapes [152]. More details of this package can be found in a recent publication [87] or the online documentation [151].

The peak shapes observed in an MR-ToF-MS spectrum can vary depending on the specific device and often deviate from purely Gaussian shapes. Most commonly observed is a tailing effect that can be pronounced on either the left or right side of the peak and breaks the symmetry of the Gaussian. The Hyper-EMG peak shapes are specifically designed with a high flexibility to fit asymmetric Gaussians which are left- or right-skewed. This is achieved by allowing flexibility in the number of exponential tails added to the left and right sides of the Gaussian distribution. The probability density function for a Hyper-EMG distribution is given as [153],

$$h_{\text{emg}}(x; \mu, \sigma, \Theta, \eta_-, \tau_-, \eta_+, \tau_+) \equiv \Theta h_{-\text{emg}}(x; \mu, \sigma, \Theta, \eta_-, \tau_-) + (1 - \Theta) h_{+\text{emg}}(x; \mu, \sigma, \Theta, \eta_+, \tau_+), \quad (4.2)$$

where Θ is a mixing parameter which determines the relative contributions of the negatively and positively skewed exponential tails, $h_{-\text{emg}}$ and $h_{+\text{emg}}$. These are each defined as,

$$h_{-\text{emg}}(x; \mu, \sigma, \eta_-, \tau_-) \equiv \sum_{i=1}^{N_-} \frac{\eta_{-i}}{2\tau_{-i}} \exp\left(\left(\frac{\sigma}{\sqrt{2}\tau_{-i}}\right)^2 + \frac{x - \mu}{\tau_{-i}}\right) \text{erfc}\left(\frac{\sigma}{\sqrt{2}\tau_{-i}} + \frac{x - \mu}{\sqrt{2}\sigma}\right), \quad (4.3)$$

$$h_{+\text{emg}}(x; \mu, \sigma, \eta_+, \tau_+) \equiv \sum_{i=1}^{N_+} \frac{\eta_{+i}}{2\tau_{+i}} \exp\left(\left(\frac{\sigma}{\sqrt{2}\tau_{+i}}\right)^2 - \frac{x - \mu}{\tau_{+i}}\right) \text{erfc}\left(\frac{\sigma}{\sqrt{2}\tau_{+i}} - \frac{x - \mu}{\sqrt{2}\sigma}\right), \quad (4.4)$$

where N_{\pm} denotes the total number of positively and negatively skewed exponential tails and the indices $\pm i$ refer to the parameters of the exponential tails themselves. The parameters η_{\pm} and τ_{\pm} are the tail weights and the exponential decay constants, respectively. μ and σ are the centroid and standard deviation of the underlying Gaussian distribution, respectively.

When fitting a spectrum with multiple peaks, the total model function over the continuous mass range is,

$$f(x) \equiv \sum_{i=1}^{N_{\text{peaks}}} a_i h_{\text{emg}}(x; \mu_i, \sigma_i, \Theta, \eta_-, \tau_-, \eta_+, \tau_+) + c_{\text{bkg}}, \quad (4.5)$$

where a_i is the amplitude, μ_i is the centroid, and σ_i is the standard deviation of the underlying Gaussian of the i -th peak. The constant c_{bkg} captures a uniform background which can arise from dark counts on the MagneTOF detector or ions that are counted after scattering with residual gas particles.

During the analysis, a single high statistics peak was chosen to be the peak shape representative for the entire spectrum. This peak was then fitted with multiple Hyper-EMG peak shapes and the best fit was chosen by minimizing Pearson's chi-squared value [151]. In the fitted spectrum plots given in this chapter, the tail-order of the Hyper-EMG peak shapes are identified using the notation $\text{emg}LR$, where L and R are numbers denoting the number of exponential tails added to the left and right side of the Gaussian, respectively.

4.3.3 Calculation of final mass values

After the ideal Hyper-EMG peak shape model was determined, all peaks in the spectrum were simultaneously fitted using a binned maximum likelihood estimation that is implemented in the emgfit package [151]. This method minimizes the negative log-likelihood ratio [154]:

$$L \equiv 2 \sum_i^N \left(f(x_i) - y_i + y_i \ln \left(\frac{y_i}{f(x_i)} \right) \right) \quad (4.6)$$

which is a different cost function than the standard χ^2 statistic. The primary reason for using a different cost function is because Equation (4.6) performs better for low-statistics peaks which follow Poisson statistics [154]. It is important to note here that the binned maximum likelihood estimation method does not make assumptions about the specific distribution of errors in the data. Instead, it focuses on maximizing the likelihood function, which measures the likelihood of observing a set of data given a set of model parameters.

The final mass value was obtained by choosing a high statistics peak with a well-known literature mass to use as the mass calibrant. Then the mass value was converted from the 1^+ charge state into a neutral atomic mass excess using,

$$\text{ME} = m_{\text{ion}} + Qm_e - Am_u \quad (4.7)$$

for an ion with A nucleons in Q charge state. When scaling from an ionic mass to the atomic mass, the electron binding energy is considered negligible the level of mass resolving power achieved by the MR-ToF-MS. m_e is the mass of the electron, and m_u is the atomic mass.

In some cases separate mass measurements had to be performed for a specific ion-of-interest. These independent data sets could not be combined prior to analysis because the MR-ToF-MS tune had slightly changed or too much time had elapsed between measurements.

In this case, the data sets were analyzed separately and the resulting mass values were later combined using a variance-weighted mean [155]:

$$m_{\text{ion}} = \frac{\sum_i m_i / (\delta m_i)^2}{\sum_i 1 / (\delta m_i)^2} \quad (4.8)$$

where m_i and δm_i denote the calculated mass and mass uncertainty of the i th independent data set.

4.3.4 Evaluation of measurement uncertainties

Following the methodology outlined in [120], a number of uncertainty contributions were considered. Each of the contributions are explained below.

Non-ideal extraction (NIE)

When the ions are released from the mass analyzer onto the detector, the exit mirror potential is quickly switched to allow them through. This switching is fast, but it still requires some time on the order of $\sim \mu s$. Because the voltage switch is not instantaneous, it can affect the kinetic energy of the ions such that the total time-of-flight is modified. If this effect is not applied equally to each ion passing through the mass analyzer, it is a systemic problem that must be mitigated and its uncertainty contribution quantified. To mitigate the effect, the opening time of the exit mirror is optimized prior to the experiment with reference ions. To estimate the systematic uncertainty contribution from this effect, we followed the procedure outlined in [120]. By scanning the mirror opening time and recording the deviation in the time-of-flight of a ^{133}Cs reference ion, the time-of-flight uncertainty due to NIE was estimated

to be $\delta t_{\text{NIE}} \approx 0.60$ ns. This was converted to a mass uncertainty using the relation [120],

$$\left(\frac{\delta m}{m}\right)_{\text{NIE}} = \frac{2\delta t_{\text{NIE}}}{t_{\text{IOI}}} \sqrt{\frac{(m/Q)_{\text{IOI}}}{(m/Q)_{\text{ref}}}} \quad (4.9)$$

where t_{IOI} is the total flight time of the ion of interest. The lowest m/Q measured during this experiment was the doubly-charged ^{145}Tb at $m/Q = 72.5$. The largest m/Q measured during this experiment was the singly-charged ^{76}Sr at $m/Q = 76$. Across this range, the mass uncertainty from NIE doesn't vary significantly, with an average uncertainty of $(\delta m/m)_{\text{NIE}} \approx 1.25 \times 10^{-7}$.

Ion-ion interactions

Ion-ion interaction uncertainty refers to peak shifting and broadening due to interactions between ions in the analyzer. The nature of these interactions is dependent on the specific tune of the MR-ToF-MS, the RIB composition, and the detection rate. At TITAN, the systematic uncertainty due to ion-ion interactions has been estimated with a conservative upper limit of $(\delta m/m)_{\text{ion-ion}} \approx 3.3 \times 10^{-8}$ per detected ion per measurement cycle [142, 156]. The rate of ions detected per measurement cycle was well below 1 during the entirety of this experiment, therefore the uncertainty contribution from ion-ion interactions was considered negligible.

Peak shape uncertainty

When fitting a peak with one of the Hyper-EMG models, each of the model parameters are determined and assigned an uncertainty. It is assumed that each of these parameter uncertainties provide an independent contribution to the uncertainty of the determined mass

value. This is called the peak shape uncertainty and a procedure for determining it is outlined in [120]. The procedure varies each model parameter by $+1\sigma$ and -1σ while keeping the other parameters unchanged. For each parameter, the larger of the two mass shifts is chosen and then added in quadrature with the other mass shifts to determine the total uncertainty contribution.

The procedure outlined above does not properly account for possible correlations between the peak shape parameters. Neglecting these parameter correlations could lead to a sizeable under-estimation of the peak shape uncertainty. Therefore, a Markov-Chain Monte Carlo (MCMC) sampling method implemented in `emgfit` was used to obtain a more refined estimate of the peak shape uncertainty [151]. This procedure uses MCMC sampling to explore the parameter space of the peak shape calibration and produces a large number of peak shape parameter sets. These parameter sets approximate the posterior distributions of the peak shape parameters and naturally account for parameter correlations. With each set of peak shape parameters, the ion-of-interest is again fitted and the root-mean-square of the resulting mass values is used to estimate the peak shape uncertainty. In all cases, the MCMC routine resulted in peak shape uncertainties smaller than those obtained from the $\pm 1\sigma$ variation method described above. For the total uncertainties reported in Section 4.12, the peak shape uncertainties from the $\pm 1\sigma$ variation method are used because they give conservative upper limits. As can be seen in Tables 4.3 and 4.4, the peak shape uncertainties are negligible compared to statistical and systematic uncertainties. Appendix A of Reference [157] gives a detailed description of the MCMC peak shape uncertainty procedure.

Statistics

The statistical uncertainty from fitting a mass peak with a Hyper-EMG peak is given as [120]

$$(\delta m)_{\text{stat}} = A_{\text{stat}} \frac{\text{FWHM}}{\sqrt{N_{\text{counts}}}}, \quad (4.10)$$

where A_{stat} is a constant of proportionality, N_{counts} is the number of counts in a peak, and FWHM is the full width at half maximum of the peak. A_{stat} depends on the specific peak shape being evaluated and for Hyper-EMG peaks must be calculated numerically. The `emgfit` package uses a parametric bootstrap routine (outlined in [120]) for determining A_{stat} [157]. This routine uses a Monte-Carlo approach to generate 1000 simulated spectra by randomly sampling events from the best-fit peakshape model obtained from the MLE fit. Peak fitting is then re-performed with each simulated spectrum and the final mass values are calculated. The statistical mass uncertainty is then calculated as the standard deviation of these 1000 mass values.

Calibration parameters

The calibration parameters c , b , and t_0 given in Equation 4.1 carry some uncertainty that must be considered for the final mass values. Recall that t_0 is the time delay due to electronic latency in the system, which was approximately $0.18 \mu\text{s}$ during this experiment. The mass uncertainty due to an uncertainty in t_0 can be calculated using Equation 24 given in [120]. Using a conservative estimate of $\delta t_0 \approx 0.5t_0$, the relative mass uncertainty contribution from δt_0 is a negligible 7.5×10^{-10} . The parameters c and b are correlated (see Equation 4.1) and therefore, as long as the ion-of-interest and calibration peak have the same number of turns N_{it} , the mass uncertainty due to uncertainties in these parameters can be fully described by

the uncertainty of the b parameter. The uncertainty of the b parameter is included in the mass calibration uncertainty [120].

Mass calibration

There are two uncertainties related to mass calibration that are considered. The first is the mass uncertainty of the mass calibrant which is obtained from literature. The second is the uncertainty of the mass calibrant fit. These uncertainties are added in quadrature to obtain the total mass uncertainty associated with mass calibration:

$$\left(\frac{\delta m}{m}\right)_{\text{recal}} = \sqrt{\left(\frac{\delta m}{m}\right)_{\text{cal,lit}}^2 + \left(\frac{\delta m}{m}\right)_{\text{cal,fit}}^2}. \quad (4.11)$$

Total uncertainty

For each mass spectrum, each uncertainty contribution was evaluated separately. For a mass measurement that used only one data set, the total mass uncertainty was calculated by combining each of the uncertainty contributions in quadrature:

$$\left(\frac{\delta m}{m}\right)_{\text{total}} = \sqrt{\left(\frac{\delta m}{m}\right)_{\text{NIE}}^2 + \left(\frac{\delta m}{m}\right)_{\text{PS}}^2 + \left(\frac{\delta m}{m}\right)_{\text{stat}}^2 + \left(\frac{\delta m}{m}\right)_{\text{recal}}^2}. \quad (4.12)$$

For a mass measurement that combined multiple independent data sets, the total statistical uncertainties for each data set were first combined using a variance-weighted mean [155]:

$$(\delta m)_{\text{stat}} = \sqrt{\frac{1}{\sum_i 1/(\delta m)_{\text{stat},i}^2}}, \quad (4.13)$$

where $(m)_{\text{stat},i}$ denotes the relative statistical uncertainty for the i -th independent data set. This ensures that the total statistical uncertainty of the combined data sets is less than the

statistical uncertainty for an individual data set. Then the systematic uncertainties for each independent data set were combined using a simple mean value:

$$\left(\frac{\delta m}{m}\right)_{\text{sys}} = \frac{\sum_i \left(\frac{\delta m}{m}\right)_{\text{sys},i}}{N_{\text{sets}}}, \quad (4.14)$$

where N_{sets} is the total number of independent data sets and i denotes the i -th independent data set. For the mass measurement with N_{sets} independent data sets, $\left(\frac{\delta m}{m}\right)_{\text{recal}}$, $\left(\frac{\delta m}{m}\right)_{\text{NIE}}$, and $\left(\frac{\delta m}{m}\right)_{\text{PS}}$ were all considered systematic. Finally, the total mass uncertainty was calculated by adding the statistical and systematic uncertainties in quadrature:

$$\left(\frac{\delta m}{m}\right)_{\text{total}} = \sqrt{\left(\frac{\delta m}{m}\right)_{\text{stat}}^2 + \left(\frac{\delta m}{m}\right)_{\text{sys}}^2}. \quad (4.15)$$

The total mass uncertainty budget of the reported strontium and lanthanide masses are shown in Tables 4.1 and 4.2, respectively. In all cases, the uncertainty is dominated by either statistical uncertainty or uncertainty from NIE.

4.4 Final values and discussion

Each spectrum in this section shows error bars for each data bin as well as fit residuals to demonstrate the goodness of fit, but the reader is reminded that these fits were performed using binned maximum likelihood estimation, not chi-squared minimization.

Nuclide	⁷⁶ Sr	⁷⁵ Sr			⁷⁴ Sr	
	1	1	2	3	1	2
Dataset	1	1	2	3	1	2
N_{it}	846	842	842	842	839	839
$\left(\frac{\delta m}{m}\right)_{\text{stat}}$	2.833E-8	1.087E-7	1.051E-7	1.493E-7	6.958E-7	5.572E-7
$\left(\frac{\delta m}{m}\right)_{\text{recal}}$	1.722E-8	1.810E-8	2.644E-8	2.044E-8	1.30E-8	1.00E-8
$\left(\frac{\delta m}{m}\right)_{\text{PS}}$	5.940E-9	2.189E-8	5.619E-9	1.329E-8	2.669E-8	1.791E-8
$\left(\frac{\delta m}{m}\right)_{\text{NIE}}$	1.2608E-7	1.2524E-7	1.2524E-7	1.2524E-7	1.2441E-7	1.2441E-7
$\left(\frac{\delta m}{m}\right)_{\text{total}}$	1.305E-7	1.453E-7			4.539E-7	

Table 4.1: The uncertainty budget of the strontium mass measurements. For mass values that were determined from multiple independent datasets, the uncertainty budget of each dataset is shown. N_{it} gives the total number of isochronous turns that were used for each measurement.

Nuclide	¹⁴⁵ Tb	¹⁴⁶ Tb	¹⁴⁸ Ho
N_{it}	848	848	783
$\left(\frac{\delta m}{m}\right)_{\text{stat}}$	2.15E-8	2.626E-8	6.325E-8
$\left(\frac{\delta m}{m}\right)_{\text{recal}}$	1.55E-8	3.987E-8	8.163E-8
$\left(\frac{\delta m}{m}\right)_{\text{PS}}$	4.00E-8	3.238E-9	9.608E-9
$\left(\frac{\delta m}{m}\right)_{\text{NIE}}$	1.231E-7	1.236E-7	1.244E-7
$\left(\frac{\delta m}{m}\right)_{\text{total}}$	1.322E-7	1.325E-7	1.620E-7

Table 4.2: The uncertainty budget of the lanthanide mass measurements. N_{it} gives the total number of isochronous turns that were used for each measurement.

Nuclide	$T_{1/2}$ (ms)	N_{counts}	Mass calibrant	Mass excess (keV)		
				Literature values	TITAN	TITAN-Literature
^{74}Sr	27.6(2.7)	36(12)	$^{148}\text{Sm}^{2+}$	-40 830#(100#) ¹	-40 970(31)	-140(105)
^{75}Sr	88(3)	424(22)	$^{75}\text{Rb}^+$	-46 620(220) ¹ -46 200(150) ²	-46 273(10)	347(220) 73(150)
^{76}Sr	7 890(70)	2 108(46)	$^{76}\text{Rb}^+$	-54 250(30) ¹	-54 257(9)	-7(31)

¹ Values from the Atomic Mass Evaluation (AME) 2020 [158] (# indicates extrapolations on the mass surface).

² A recent value from the CSRe [159].

Table 4.3: Summary of strontium masses determined as part of this thesis. All masses were measured as singly charged ions. The third column of the table gives N_{counts} , which is the number of counts determined by the area of the fitted mass peak. The uncertainty of N_{counts} is given by the fit.

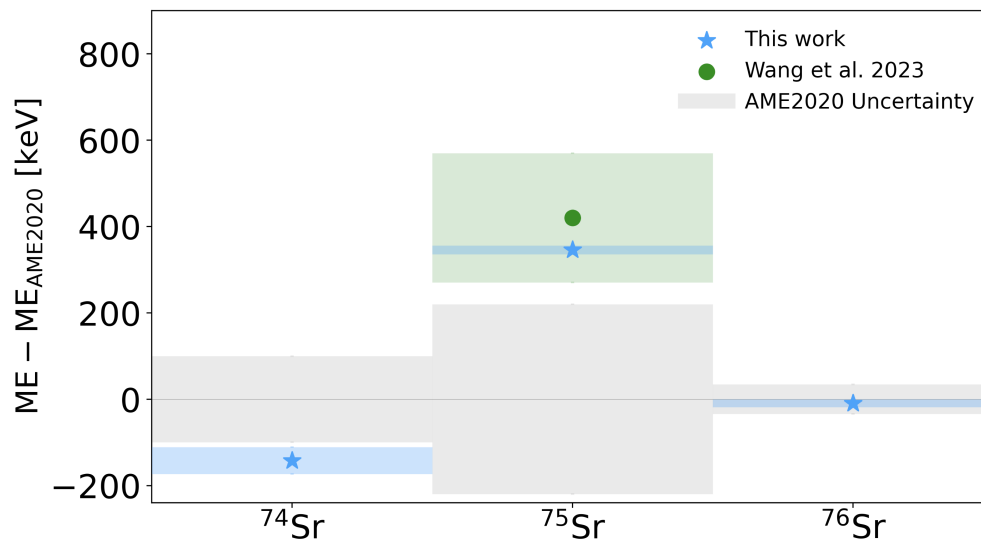


Figure 4.4: The deviation in mass excess (ME) between the determined mass values and literature values provided by the AME 2020 [69]. A direct storage ring measurement recently reported by Wang *et al.* (green circle) is also shown [159]. Error bars show $\pm 1\sigma$.

4.4.1 Strontium

For the measurements presented here, the mass resolving power fell within the range $R_m = 400,000 - 530,000$. At $A = 76$, this corresponds to an ability to resolve peaks or isomeric states which are approximately 140 – 180 keV separated. The final mass values for strontium are given in Table 4.3 with other pertinent values including literature values and deviations from literature. The deviation between the determined strontium mass values and literature values provided in the AME 2020 is shown in Figure 4.4.

Strontium-76

Our final mass value of ^{76}Sr is calculated from a single data set which accumulated data for 15 minutes and obtained over 2000 counts. With the mass-selective re-trapping function, the spectrum was relatively clean. ^{85}Rb from the internal ion source served as the TRC reference peak and ^{76}Rb served as a mass calibration peak. The literature value for ^{76}Sr is provided by a Penning trap measurement at ISOLTRAP [160] and serves as a good benchmark for the TITAN MR-ToF-MS. Our new value is within 1σ of the ISOLTRAP value and improves the mass precision by a factor of 3.

Strontium-75

Our final mass value of ^{75}Sr is a variance-weighted mean from three independent data sets collected over the course of the beamtime. The total collection time was approximately 17 minutes and resulted in over 400 counts of ^{75}Sr . Even with mass-selective re-trapping, a significant amount of contamination from doubly-charged lanthanides was present. This included $^{150}\text{Sm}^{2+}$, $^{150}\text{Gd}^{2+}$, $^{150}\text{Eu}^{2+}$, $^{150}\text{Tb}^{2+}$, $^{150}\text{Dy}^{2+}$, and $^{150}\text{Ho}^{2+}$. Fortunately, the doubly-charged lanthanides did not obfuscate the ^{75}Sr peak.

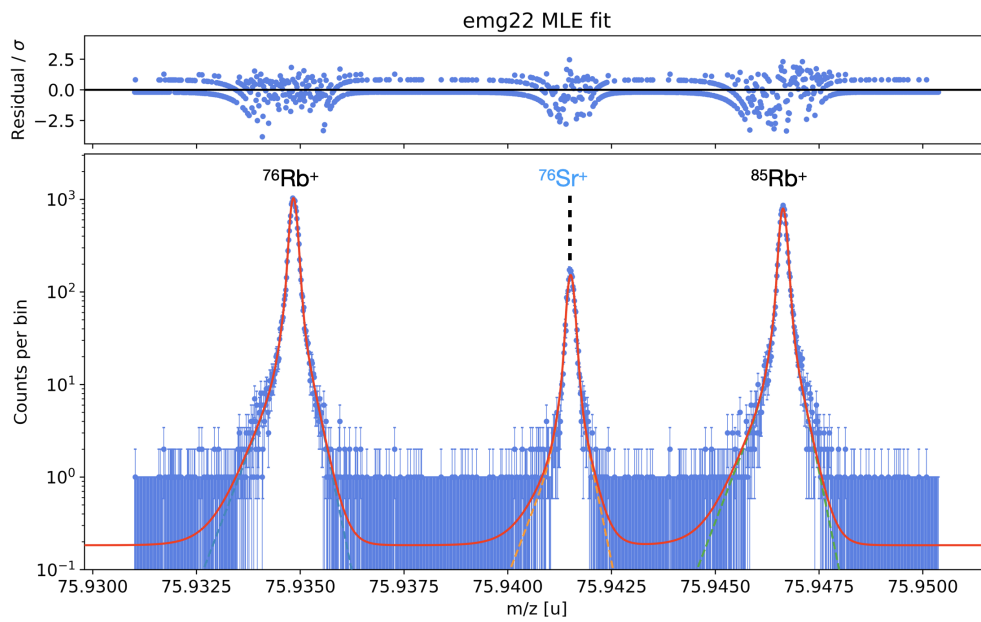


Figure 4.5: The $A/Q = 76$ spectrum (blue circles) showing the ^{76}Sr ion of interest, ^{76}Rb , and the deliberately injected ^{85}Rb . Error bars shown are $\pm 1\sigma$ assuming Poisson statistics in each bin. Multi-peak fits to the data (solid red line) and the underlying single peak fits (dashed lines) are indicated. The top panel shows fit residuals normalized by the standard deviation of each bin.

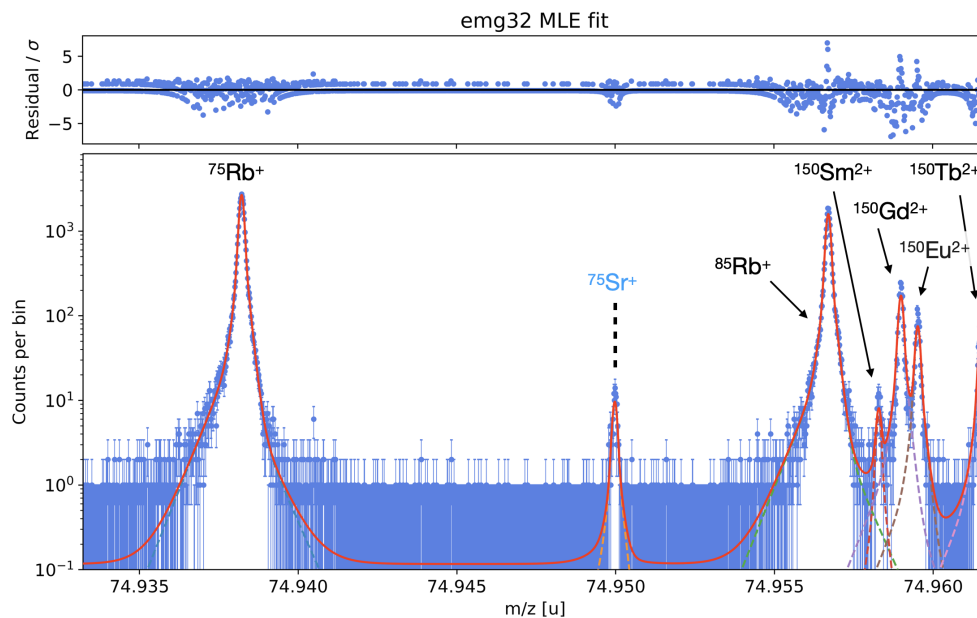


Figure 4.6: The $A/Q = 75$ spectrum from data set 1, showing the ^{75}Sr ion of interest and a native ^{75}Rb peak. Doubly-charged lanthanides to the right of ^{75}Sr are a significant beam contaminant. Multi-peak fits to the data (solid red line) and the underlying single peak fits (dashed lines) are indicated. The top panel shows fit residuals normalized by the standard deviation of each bin.

The AME 2020 literature value is an indirect observation obtained from a Q-value measurement of the ^{75}Sr decay into ^{75}Rb [161]. Our value deviates from this by approximately 1.5σ , which is reasonable given the systematic uncertainties of a β -decay endpoint measurement to accurately estimate the Q-value. More recently, the experimental cooler storage ring (CSRe) in Lanzhou has achieved an improved precision with a reported mass excess of $-46\,200(150)$ keV [159]. Our value is within 1σ agreement with the CSRe value and improves upon the mass precision by a factor of 15.

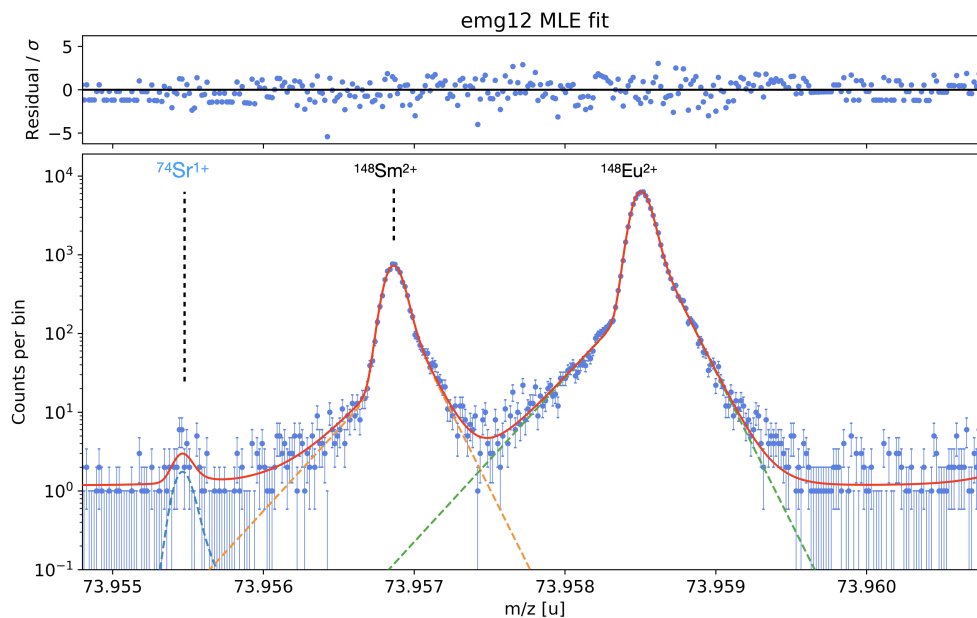


Figure 4.7: The $A/Q = 74$ spectrum from data set 2, showing the ^{74}Sr ion of interest on the left shoulder of doubly-charged contaminants. Multi-peak fits to the data (solid red line) and the underlying single peak fits (dashed lines) are indicated. The top panel shows fit residuals normalized by the standard deviation of each bin.

Strontium-74

Our final mass value of ^{74}Sr is a variance-weighted mean from two independent data sets. The total collection time was approximately 500 minutes and resulted in 36 counts of ^{74}Sr . To verify the peak was indeed strontium, the TRILIS lasers were blocked for a data set of similar recording length. A comparison between the laser blocked and laser unblocked spectra is shown in Figure 4.2. Similar to the $A = 75$ spectrum, there was a significant background contamination from doubly-charged lanthanides such as $^{148}\text{Sm}^{2+}$, $^{148}\text{Eu}^{2+}$, $^{148}\text{Tb}^{2+}$, and $^{148}\text{Dy}^{2+}$. The only singly charged species in the spectrum were the ion of interest and the deliberately injected rubidium ions.

Mass-selective re-trapping was used for this measurement and allowed a factor of 100 more

beam intensity to be delivered to the MR-ToF-MS all while suppressing beam contamination. This mode played a critical role in ensuring TITAN acquired enough statistics for $^{74}\text{Sr}^+$ to be observed. The plot in Figure 4.7 shows a fitted $A = 74$ spectrum from data set 2 with $^{74}\text{Sr}^+$ visible on the left shoulder of the $^{148}\text{Sm}^{2+}$ peak.

The literature value of ^{74}Sr is an extrapolation that was provided by Rodríguez *et al.* from Coulomb shifts of the ^{74}Kr nucleus [115]. Our value deviates from this extrapolation by approximately 1.4σ . In contrast to the $^{75-76}\text{Sr}$ measurements, the ^{74}Sr total relative uncertainty of 4.54×10^{-7} is dominated by statistical uncertainty. This is reflected by the relatively large peak area uncertainty reported in Table 4.3.

4.4.2 Lanthanides

The mass values determined for the lanthanides are given in Table 4.4 with other pertinent values including literature masses and mass deviations. Literature values are provided by the AME 2020 [158] and a measurement at the Cooler-Storage Ring ESR by Litvinov *et al.* using Schottky mass spectrometry [162]. The lanthanides were challenging to analyze due to the very crowded spectra and the possibility of ground state species overlapping with low-lying isomeric states. This possibility constrained the assignment of the various calibrant peaks during the analysis.

Terbium-145

Our final mass value of ^{145}Tb is obtained from a single data set collected in approximately 80 minutes and accumulating nearly 700 counts. The spectrum showed strong contamination from $^{145}\text{Pm}^{2+}$, $^{145}\text{Sm}^{2+}$, $^{145}\text{Eu}^{2+}$, $^{145}\text{Gd}^{2+}$, $^{145\text{m}}\text{Gd}^{2+}$, and $^{145}\text{Dy}^{2+}$. Merging of stable rubidium calibrants into the beam was attempted, but these calibrant peaks were

Nuclide	N_{counts}	Mass calibrant	Mass excess (keV)		
			Literature values	TITAN	TITAN- Literature
^{145}Tb	698(33)	$^{145}\text{Sm}^{2+}$	-66 400(110) ¹ -65 881(28) ²	-65 849(18)	551(112) 32(33)
$^{146}\text{Tb}+^{146\text{m}1}\text{Tb}?$	1 359(39)	$^{146}\text{Sm}^{2+}$	-67 760(40) ¹ -67 424(28) ²	-67 413(18)	347(44) 11(33)
$^{148}\text{Ho}+^{148\text{m}1}\text{Ho}?$	274(17)	$^{148}\text{Sm}^{2+}$	-57 990(80) ¹ -57 815(30) ² -57805(9) ³	-57 807(22)	183(83) 8(37) -2(24)

¹ Values from the Atomic Mass Evaluation (AME) 2020 [158].

² Values from Litvinov *et al.* [162].

³ Value from Rauth *et al.* [163].

Table 4.4: Summary of lanthanide masses determined as a part of this thesis and their deviations from literature values. All masses were measured as doubly-charged ions. The second column of the table gives N_{counts} , which is the number of counts determined by the area of the fitted mass peak. The uncertainty of N_{counts} is given by the fit.

not well resolved from the contaminant peaks and therefore did not provide their intended benefit. As such, one of the contaminant species had to be used as the TRC reference.

The literature values provided in the AME 2020 have been estimated from decay data of the isomeric and ground states of ^{145}Dy into ^{145}Tb [164–166]. It is suggested that the ground state has a 30.9(6) s half-life and an isomer with unknown half-life exists at 860(200) keV [167]. However, it can be seen that our value has a rather large disagreement with the AME 2020 value nearing a 5σ deviation. This is not unreasonable given the difficulty in estimating ground state masses from β -decay Q-values.

Litvinov *et al.* used time-resolved Schottky mass spectrometry at the cooler-storage ring ESR and reported a mass excess of $-65881(28)$ keV [162]. According to the procedure outlined in [168], the authors increased the uncertainty of their measurement to 57 keV to account for the possibility of the unresolved isomer. The resolving power reached by our spectrometer would be well able to resolve the 860(200) keV isomer, but we see no indication that it is present in the spectrum. This is illustrated in Figure 4.8 where the same spectrum displays our ability to resolve ^{145}Gd and its 749.1(0.2) keV isomer, $^{145\text{m}}\text{Gd}$ [158, 169]. Our value is in good agreement with the value published by Litvinov *et al.* and we therefore conclude that we must have observed the ground state with no isomer present. The total relative mass error is 1.3×10^{-7} which is dominated by systematic uncertainties.

Terbium-146

Our mass value of ^{146}Tb is based on a single data set collected in about 100 minutes with over 1300 counts registered. Again the spectrum showed strong contamination from other doubly-charged lanthanides such as $^{146}\text{Sm}^{2+}$, $^{146}\text{Pm}^{2+}$, $^{146}\text{Eu}^{2+}$, $^{146}\text{Gd}^{2+}$, and $^{146}\text{Dy}^{2+}$. At this mass unit we were able to successfully inject ^{85}Rb and ^{87}Rb into the spectrum and keep

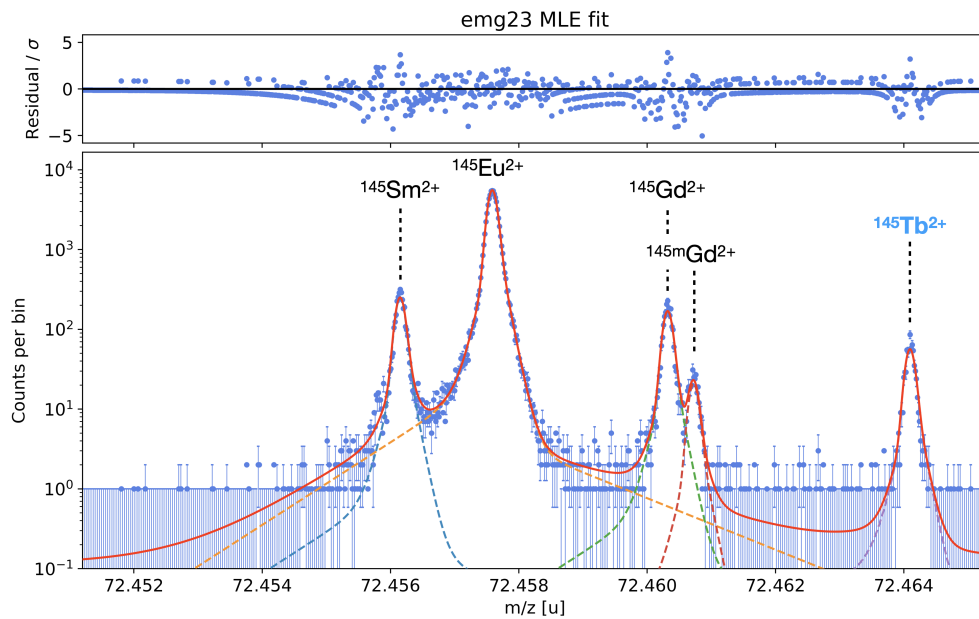


Figure 4.8: Fitted $A = 145$ spectrum showing the $^{145}\text{Tb}^{2+}$ ion of interest and some of the contaminant species. Our ability to resolve $^{145}\text{Gd}^{2+}$ from its isomer suggests that we should also resolve $^{145}\text{Tb}^{2+}$ from its isomer.

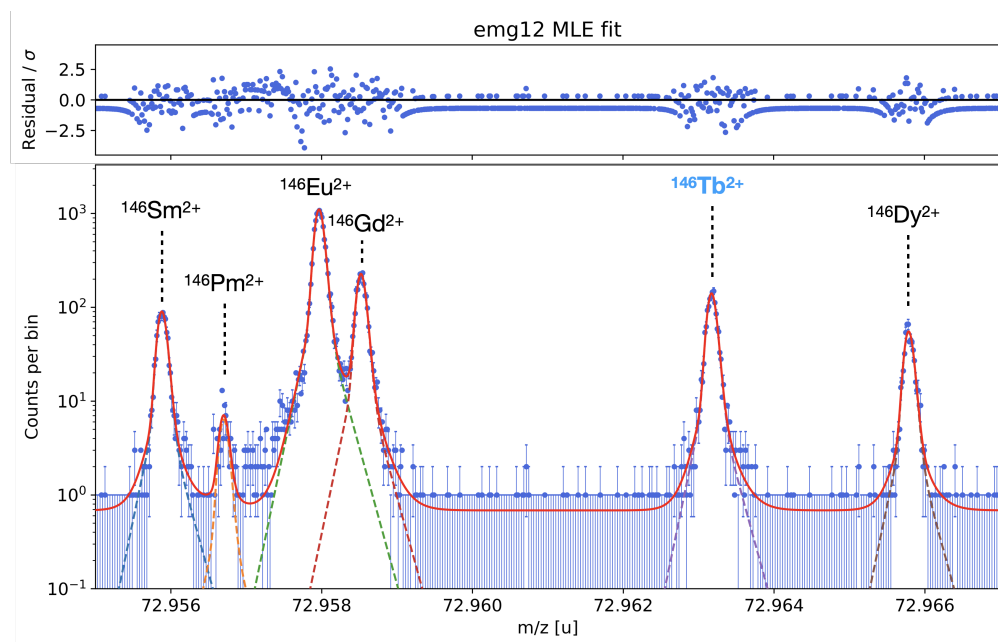


Figure 4.9: Fitted $A = 146$ spectrum showing the $^{146}\text{Tb}^{2+}$ ion of interest and contaminant species.

them well resolved from the contaminant peaks. ^{85}Rb was chosen as the ideal TRC reference peak.

Previously, the ground state mass of ^{146}Tb has been determined via a β -decay Q-value measurement paired with the direct mass measurement of ^{146}Dy [163]. ^{146}Tb has two isomeric states which have been studied through a number of in-beam experiments [170–174]. $^{146\text{m}1}\text{Tb}$ has an excitation energy of 150(100) keV and a half-life of 24.1(0.5) s and therefore must be considered in our analysis. $^{146\text{m}2}\text{Tb}$ has an excitation energy of 930(100) keV and a reported half-life of 1.18(0.02) ms and therefore any production of this state is expected to be completely diminished by the time it effuses out of the target and is delivered to TITAN.

Our measurement of ^{146}Tb achieved a mass resolving power of $R_{\text{m}} \sim 500,000$, which is right on the threshold of resolving $^{146\text{m}1}\text{Tb}$. Therefore, we cannot state whether our peak

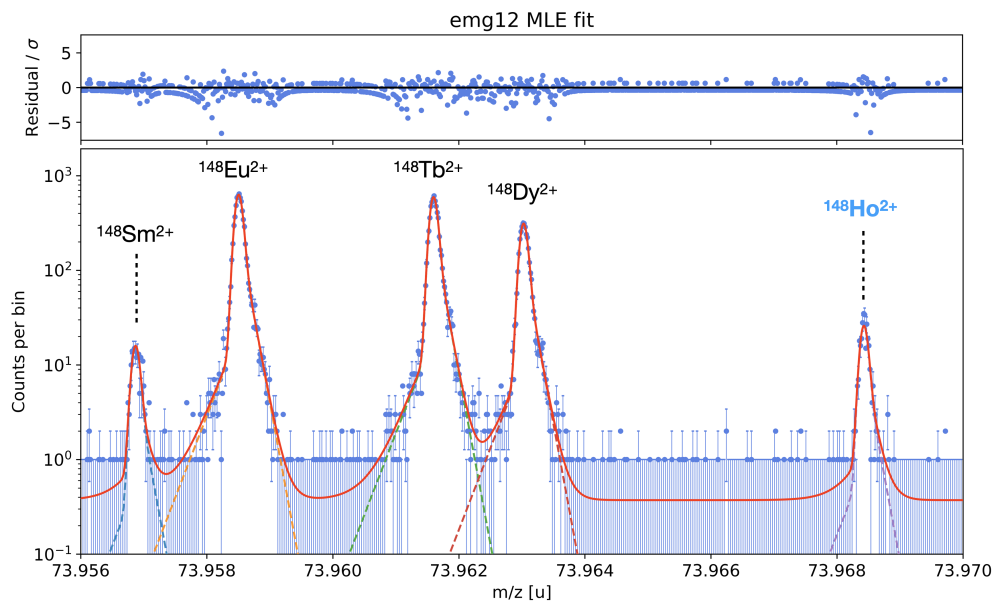


Figure 4.10: Fitted $A = 148$ spectrum showing the $^{148}\text{Ho}^{2+}$ ion of interest and contaminant ions.

contains 1) only the ground state, 2) only the isomeric state, or 3) some combination of both states. Based on the resolving power, if the peak contained both ground and isomeric states, the isomeric state would have to be below ~ 150 keV excitation energy. It is important to emphasize that our value deviates from the AME 2020 value by nearly 8σ , but is in very good agreement with the value published by Litvinov *et al.* [162]. The total relative error of 1.3×10^{-7} is dominated by systematic uncertainties.

Holmium-148

Our final mass value of ^{148}Ho is based on a single data set which was collected in about 60 minutes and registered over 270 counts. At this mass unit we successfully injected both rubidium calibrants from the internal ion source and used ^{87}Rb as the TRC reference peak. The spectrum was crowded with other doubly-charged lanthanides which can be seen in

Figure 4.10. $^{148}\text{Sm}^{2+}$ was chosen as a suitable mass calibration peak because its mass is known with an order of magnitude better precision than the other doubly-charged contaminants [167]. Other candidates such as $^{148}\text{Tb}^{2+}$ were not reliable choices because of the possibility of an isomeric admixture contained in the peak.

The NUBASE 2020 evaluation reports an atomic mass excess of the (1^+) ground state as $-57990(80)$ keV with a life-time of $2.2(1.1)$ s and two isomeric states $^{148\text{m}1}\text{Ho}$ and $^{148\text{m}2}\text{Ho}$. Similar to the case at $A = 146$, $^{148\text{m}2}\text{Ho}$ has a lifetime of $2.36(0.06)$ ms and is therefore not expected to be present in our spectra. The $(5)^-$ $^{148\text{m}1}\text{Ho}$ however has a reported excitation energy of $250(100)$ keV and a lifetime of $9.49(0.12)$ s and must be considered in our analysis.

This isotope has been previously studied with Schottky mass spectrometry by Litvinov *et al.* [162] and a Penning trap measurement by Rauth *et al.* [163]. In both cases the experimenters were unable to resolve $^{148\text{m}1}\text{Ho}$ from the ground state and resorted to following the AME guideline for determining the mass center [69]:

$$M_0 = M_{exp} - R_m E_1 \quad (4.16)$$

where R_m denotes the isomeric admixture ratio, M_{exp} is the experimentally determined mass center, E_1 is the excitation energy of the isomeric state.

Prior to adjusting the mass center to account for the isomeric admixture, the measurements were in good agreement: a mass excess of $-57815(30)$ keV was reported by Litvinov *et al.* and a mass excess of $-57805.4(8.8)$ keV was reported by Rauth *et al.*. Litvinov *et al.* used the reported $400(100)$ keV excitation energy [168] and an isomeric admixture ratio of $R_m = 0.5$ to determine the new mass center. This admixture ratio was chosen because another value could not be derived. Rauth *et al.* shifted the excitation energy to $250(100)$ keV based on their device's resolving power. An admixture ratio of

$R_m = 0.741(13)$ was calculated from the observed yield ratio between the $1/2^+$ ground and $11/2^-$ isomeric states of ^{143}Dy and ^{147}Dy . It was argued that this mixing ratio is appropriate to apply to ^{148}Ho because the $(6)^-$ isomeric and (1^+) ground states have the same spin difference. However, since the 2012 NUBASE evaluation [175], the assignment of the ^{148}Ho isomeric state was changed to (5^-) , so this argument no longer applies.

Our measurement of ^{148}Ho achieved a mass resolving power of $R_m \sim 500,000$. Based on this resolving power, if both the ground and isomeric states were present in the peak, the isomeric state would have to be below ~ 150 keV excitation energy. Our analysis gives an atomic mass excess of $-57807(22)$ keV, which is in good agreement with the values previously reported by Litvinov *et al.* and Rauth *et al.* [162,163]. The total relative error is 1.6×10^{-7} , with the largest contribution from systematic uncertainties.

Chapter 5

Neutron-deficient Sr masses for nuclear structure and astrophysics

5.1 Scientific impact on the isobaric multiplet mass equation

In Chapter 2 we discussed using the isobaric multiplet mass equation (IMME) to study nuclear structure and isospin symmetry breaking in nuclei. This requires detailed knowledge of nuclear masses and level structure near the $N = Z$ line to provide complete isobaric mass multiplets. The IMME is well tested in the $A = 10 - 60$ region thanks to the most recent global evaluations provided by Lam *et al.* [63] and MacCormick *et al.* [49]. Evaluating the IMME at higher masses is difficult because of the encroaching dripline, however mass measurements can complete some of the low-lying multiplets at $T = 1/2$ and $T = 1$ [49]. Our mass measurements of $^{74-75}\text{Sr}$ provide the first time experimental completion of the $T = 1/2$ doublet at $A = 75$ and the $T = 1$ triplet at $A = 74$. In the following sections we take a look at the impact the new data have on the trends of the IMME coefficients.

Evaluation of the IMME coefficients was performed using an error-weighted least-squares fitting of the experimental data with the Python lmfit package [176]. Unless otherwise noted, all mass values were obtained from the Atomic Mass Evaluation (AME) 2020 [69] and excitation energies were obtained from Evaluated Nuclear Structure Data Files (ENSDF) provided by the National Nuclear Data Center [70]. The IMME evaluations by MacCormick *et al.* [49] and Lam *et al.* [63] were used to determine the correct isobaric analog states for a given multiplet. For isobaric analog states that are nuclear excited states, the uncertainty is calculated by combining the ground state uncertainty and the excitation energy uncertainty in quadrature.

5.1.1 The $T = 1/2$ doublets

In Section 2.1.3 we discussed the anomalous behaviour of the $T = 1/2$ b coefficients in the upper fp-shell. This was highlighted in the bottom panel of Figure 2.2, where the plot of Δb shows the onset of a staggering anomaly at $A = 69$ which continues until the available experimental data ends at $A = 75$. There is currently no theoretical mechanism proposed to explain this staggering anomaly and multiple theoretical approaches cannot reproduce it [74–77]. However, Δb generally lacks precision in the fp-shell because the mass uncertainty of the $T_z = -1/2$ isobaric analog states are relatively large. Further experimental work to improve the precision of the b coefficients in the fp-shell with mass measurements will help to resolve the staggering anomaly. This includes mass measurements of $T_z = -1/2$ nuclei such as ^{69}Br , ^{71}Kr , ^{73}Rb , and ^{75}Sr .

A recent mass measurement of ^{71}Kr reported by Wang *et al.* [159] is a first step towards this goal. Combined with our measurement of ^{75}Sr , we can better pin down Δb in the fp-shell. Figure 5.1 shows the new trend of Δb when the AME 2020 data is updated with the new masses at $A = 71, 75$. These new masses shift the values of Δb at $A = 71, 73$, and 75 . It can clearly be seen that the new mass values remove the staggering anomaly by restoring the regular staggering pattern. With regards to the $A = 4n + 1$ and $A = 4n + 3$ multiplet subgroups, this means that their trend lines no longer intersect at $A = 69$ as was suggested in Figure 2.2. Two theoretical curves are shown to illustrate the restoration of agreement between theoretical predictions and the experimental values. The first is a global fit of the homogeneously charged sphere model modified with two free parameters performed by MacCormick *et al.* [49]. The second theoretical curve is an extended Skyrme pn -mixed Density Functional Theory (DFT) calculation by Bączyk *et al.* [75].

An interesting feature seen in the plot of Δb in Figure 5.1 is a dampening of the staggering

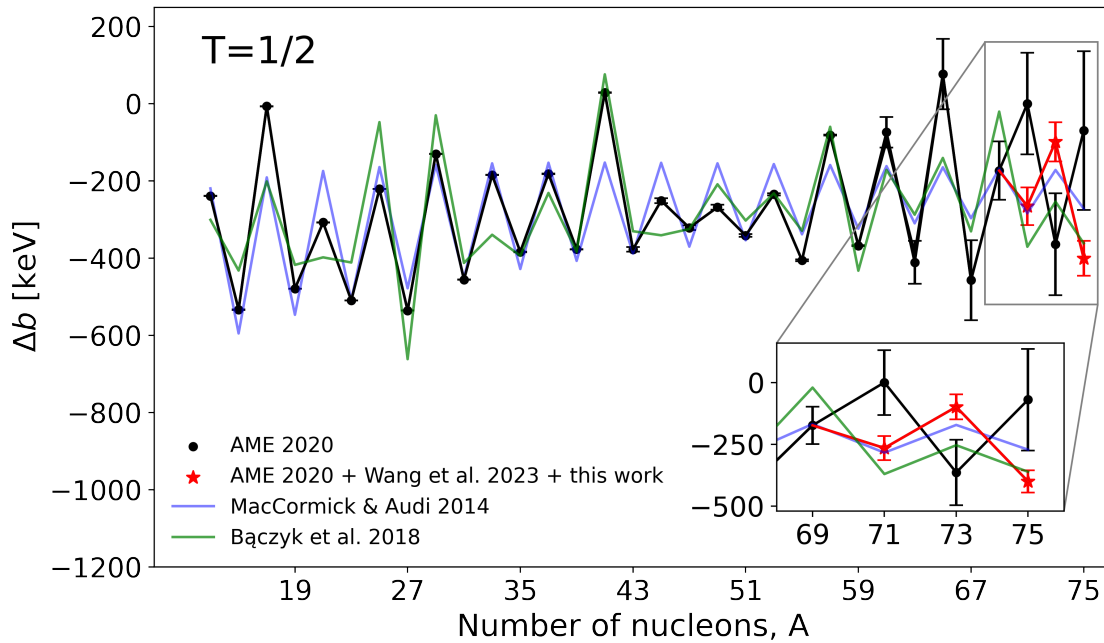


Figure 5.1: The staggering behaviour of the doublet b coefficients viewed using a plot of Δb . The AME 2020 evaluation [69] (black curve) shows the staggering anomaly at $A = 69 - 75$ which is removed when the new ^{75}Sr and ^{71}Kr masses (red curve) are included. A charged homogeneous sphere calculation (blue curve) [49] and a DFT calculation (green curve) [75] are both shown to illustrate that the experimental data and theoretical predictions are now once again in agreement.

amplitude in the $f_{7/2}$ subshell ($A = 43-53$). This feature has been reproduced with a modern nuclear shell-model approach by Kaneko *et al.* [74], and an extended Skyrme pn -mixed DFT approach by Bączyk *et al.* [75]. While these approaches both showed success in reproducing the $f_{7/2}$ dampening, it is notable that the underlying mechanisms responsible for it aren't exactly in agreement. With the inclusion of the isospin non-conserving nuclear forces, Kaneko *et al.* [74] observed a decrease in the $f_{7/2}$ staggering amplitude while Bączyk *et al.* [75] observed an increase in the staggering amplitude. It is unlikely that better experimental mass precision in this region will resolve the discrepancy between these results. However, Bączyk *et al.* also predicted a similar dampening effect to occur in the $g_{9/2}$ subshell at $A = 83$. New precision mass measurements at higher masses would help to test these theoretical predictions.

5.1.2 The $T = 1$ triplets

Isospin symmetry breaking (ISB) corrections are a critical input for testing the conserved vector current (CVC) hypothesis and top-row unitarity of the Cabibo-Kobayashi-Maskawa (CKM) quark mixing matrix [53]. Because the $T = 1$ triplets are the smallest multiplets that can be used to extract both the b and c coefficients, the triplets have historically been the target for theoretical approaches to extracting ISB corrections [53]. This method was pioneered by Towner and Hardy using the shell-model approach [53], but methods using a Density Functional Theory (DFT) approach by Satula *et al.* [177] and an ab-initio Valence-Space In-Medium Similarity Renormalization Group (VS-IMSRG) approach by Martin *et al.* [178] have also been implemented. Martin *et al.* performed their calculations along $A = 10 - 74$, but experimental triplet data above $A = 60$ was not available to validate their calculations.

The $T = 1$ triplets are constructed from mass and level structure data of even- A nuclei. The most recent global survey of the IMME by MacCormick *et al.* evaluated the triplets up to $A = 58$ [49]. This was recently extended up to $A = 60$ with a TITAN mass measurement of ^{60}Ga by Paul *et al.* [87]. In contrast to the doublets, not all of the isobaric analog states in a triplet are nuclear ground states. Most commonly, the $T_z = \pm 1$ isobaric analog states are nuclear ground states while the $T_z = 0$ analog state is an excited state. However, as we move to masses $A > 40$, the $T_z = 0$ state tends to be a nuclear ground state if $A = 4n + 2$ (where n is a positive integer) but an excited state if $A = 4n$. Therefore, $A = 4n + 2$ multiplets above $A = 40$ can be completed with precision mass measurements and without the need for knowledge of level structure. A recent mass measurement of ^{66}Se by Zhou *et al.* [88] and our mass measurement of ^{74}Sr both complete their respective $A = 4n + 2$ triplets. The $A = 74$ triplet and is now the highest experimentally evaluated triplet by eight mass units. With these newly completed triplets we can test the accuracy of the VS-IMSRG predictions by Martin *et al.* [178].

In the previous section we used the derivative Δb to view the non-trivial structure of the doublet b coefficient. However, because the new triplet data at $A = 66$ and 74 do not have neighbors, we cannot perform such an action. Instead, we use the approximate value of b provided by the homogeneously charged sphere approximation in Equation (2.12). By subtracting Equation 2.12 from our experimental data on the triplet b coefficients, we can view finer structural details. This value quantifies the deviation of experimental b coefficients from predictions of the homogeneously charged sphere model and helps visualize fine details of the coefficients:

$$b_{\text{dev}} \equiv b_{\text{exp}} - b_{\text{hcs}} = b_{\text{exp}} + \frac{3e^2(A-1)}{5r_0A^{1/3}}. \quad (5.1)$$

Figure 5.2 plots this value for only the $A = 4n + 2$ multiplets using data from the AME

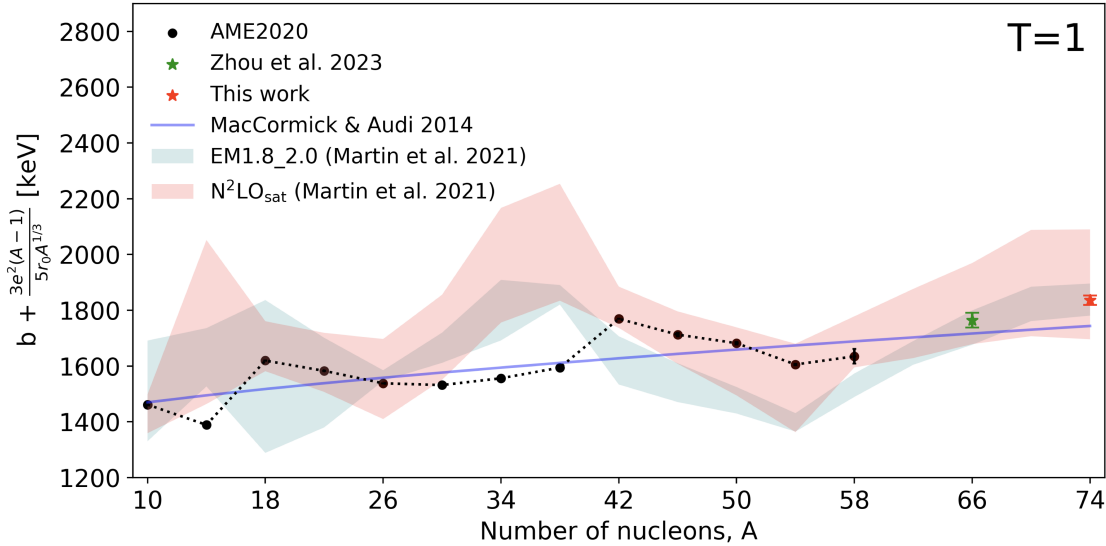


Figure 5.2: A plot of the triplet b coefficients using b_{dev} , the deviation between the experimental b coefficient and the prediction of the homogeneously charged sphere approximation. The AME 2020 data [69] (black circles) extends to $A = 58$ but the two new mass measurements give data points at $A = 66, 74$ (green and red stars). The VS-IMRSG predictions by Martin *et al.* show good agreement with the new data points.

2020 and the new data at $A = 66, 74$. We observe a consistently increasing trend which is supported by three theoretical curves that are shown. The first is the two-parameter global fit of the homogeneously charged sphere approximation by MacCormick *et al.* [49]. The other two are the *ab initio* VS-IMSRG calculations by Martin *et al.* [178]. The VS-IMSRG calculations utilized two different interactions derived from chiral effective field theory, 1.8/2.0(EM) [179] and N²LO_{sat} [180]. We see that the VS-IMSRG calculations agree well with the new data points at $A = 66, 74$.

Figure 5.3 updates the AME 2020 triplet c coefficients for the $A = 4n + 2$ multiplet subgroup by including the new values at $A = 66, 74$. We see that the new data points are in good agreement with the two-parameter homogeneously charged sphere approximation

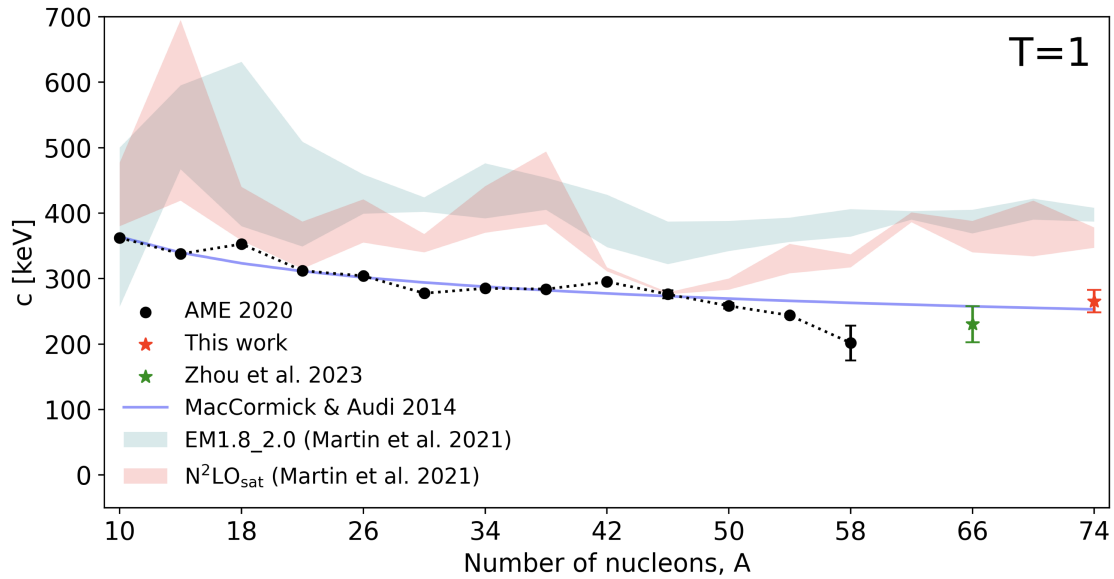


Figure 5.3: The c coefficients extracted from $A = 4n + 2$ triplets. New mass measurements of ^{66}Se (green star) and ^{74}Sr (red star) provide an extension of the coefficient data past what was available in the AME 2020 evaluation (black circles) [69]. The two-parameter global fit of the homogeneously charged sphere model (blue curve) by MacCormick *et al.* [49] agrees well with the trend up to $A = 74$. VS-IMSRG calculations using two different χEFT -derived interactions (filled curves) is reproduced from Martin *et al.* [178]. While the VS-IMSRG calculations capture the general trend of the data, there is still an appreciable amount of deviation.

by MacCormick *et al.* [49]. However, the VS-IMSRG calculations by Martin *et al.* seem to consistently over-predict the value of the c coefficient by ~ 200 keV.

5.2 Scientific Impact on the rp-process and Type-I X-ray Bursts

In this section we investigate the impact that the newly measured strontium masses have on burst model predictions using a self-consistent single-zone model [37]. The model that we used is Model A from [37] because its predicted light curves and burst ashes have been demonstrated to capture important mass uncertainties along the rp-process pathway [41]. This model uses a high mass fraction of initial hydrogen ($X_H = 0.66$) which gives a strong rp-process path up to $A \approx 104$ with peak burst temperatures near 2 GK.

We first evaluated how the new masses affect the relevant astrophysical proton-capture reaction rates. This includes the following reactions: ${}^{73}\text{Rb}(p, \gamma){}^{74}\text{Sr}$, ${}^{74}\text{Rb}(p, \gamma){}^{75}\text{Sr}$, ${}^{75}\text{Rb}(p, \gamma){}^{76}\text{Sr}$, and ${}^{76}\text{Sr}(p, \gamma){}^{77}\text{Y}$ which are highlighted in Figure 5.4. Because the ${}^{77}\text{Y}$ mass is unmeasured and given as an extrapolation in the AME2020 [158], we used a mass value previously calculated from the ${}^{77}\text{Sr}$ mirror nucleus using the Coulomb displacement energy method [39, 41]. Calculation of the astrophysical reaction rates was performed using the Hauser-Feshbach nuclear reaction code TALYS 2.0 [181] which outputs the reaction cross-sections as a function of temperature in GK. The competing photo-disintegration rates were calculated from the proton-capture Q-values using the principle of detailed balance given by Equation (2.17). To evaluate the sensitivity of the simulations to the mass inputs, the mass values were varied by $\pm 3\sigma$ for the AME2020 data as well as the new mass values.

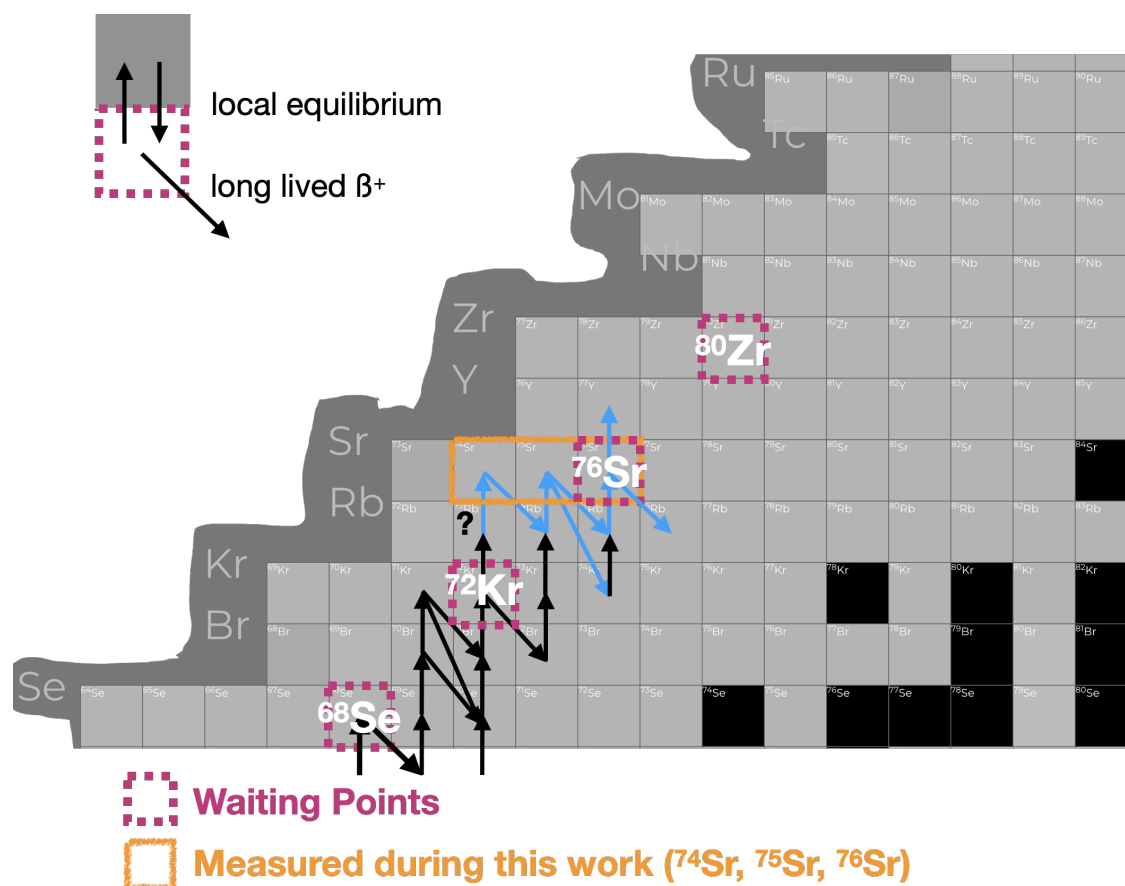


Figure 5.4: An illustration of the rp-process path showing the masses measured during this work. The blue arrows indicate the reactions that are directly impacted by the new mass values whose effect on the rp-process was studied. The important waiting point nuclei are indicated with a magenta border as well as a small diagram at the top left showing the conditions that enable a waiting point.

The new mass values help us to better pin down the reaction flow between the waiting points at ^{72}Kr and ^{76}Sr . We find an increased strength of the ^{74}Rb β -decay branch and a decrease in the amount of mass flow beyond the ^{76}Sr waiting point. Based on the AME2020 evaluation, the $^{76}\text{Sr}(p,\gamma)$ branch remained 50% uncertain, but this has now been reduced to 20% with the remaining uncertainty due to the unmeasured ^{77}Y mass. This reduces the ^{76}Sr bypass flow from 2% to 0.7%, which is connected with an increased production of stable $A = 74$ ashes. The mass uncertainty of stable $A = 74$ ash production was previously 16% and is now a negligible 0.7%.

The main contributors to the change in reaction flow are the new mass values for ^{75}Sr and ^{76}Sr and the ^{77}Y estimated value. Sequential two-proton capture into ^{74}Sr had a minimal effect as a ^{72}Kr waiting point bypass pathway. This was in fact already known because a previous study determined that ^{74}Sr does not reach a (p,γ) equilibrium with ^{72}Kr and ^{73}Rb due to the negative proton separation energy of ^{73}Rb which was calculated to be $S_p(^{73}\text{Rb}) = -640(40)$ keV [182]. While presently the altered rp-process reaction flow patterns have only minimal impact on X-ray burst observables, the effect of the new strontium masses may have a stronger impact when more precision mass measurements in this region and beyond become available. For example, a proposal at the Facility for Rare Isotope Beams (FRIB) was recently accepted to perform precision mass measurements of $^{78-80}\text{Zr}$ and $^{77-79}\text{Y}$ using the Low Energy Beam Ion Trap (LEBIT) facility [183].

In addition, we must take caution when accepting reaction rate calculations for nuclei near the proton drip line where resonant reactions can occur. As mentioned in Section 2.2, the Hauser-Feshbach model of reaction rates can be inaccurate if for example a few resonances dominate the reaction [111].

Chapter 6

Installing and commissioning a new HPGe array at the TITAN EBIT

6.1 Decay spectroscopy with radioactive highly charged ions

Highly charged ions (HCI) are atomic systems which have many of their electrons removed from the atomic orbitals. When many of the electrons are removed from the atomic orbitals, the resulting HCI is a drastically simplified quantum mechanical system and the remaining electrons are tightly bound. Because the remaining electrons are more tightly bound, they experience extremely strong electromagnetic fields up to 10^{16} V/cm electric and 20,000 T magnetic fields [184]. This leads to magnified QED effects and the elevation of properties like binding energy, fine structure splitting, and hyperfine splitting [185]. This makes HCI an extremely sensitive tool for studying fundamental physics theories [186] and an ideal system for building an atomic optical clock [187]. In addition, because most of the matter existing in hot astrophysical conditions is existing in a highly ionized form, terrestrial experiments on HCI are useful for interpreting astrophysical X-ray spectra [188, 189].

In the realm of nuclear physics research, HCI have been used to increase the precision of mass measurements. The benefit of using HCI for Penning trap mass measurements arises from the linear scaling of mass precision with the mass-to-charge ratio m/Q [184],

$$\frac{\delta m}{m} \propto \frac{m}{QB T_{\text{rf}} \sqrt{N_{\text{ion}}}} \quad (6.1)$$

where B is the magnetic field strength, T_{rf} is the excitation time, and N_{ion} is the number of ions measured. The effectiveness of Penning trap mass measurements with stable HCI has been well demonstrated with the success of the SMILETRAP facility [190]. The use of HCI to achieve high mass precision is even more beneficial at RIB facilities where the measurement time is limited by short half-lives, and high statistics are hard to gather with

typically low production yields of the ion of interest. TITAN first demonstrated Penning trap mass measurements of radioactive highly-charged rubidium and gallium isotopes in 2011 [191].

The removal of electrons from the atomic orbitals also has an impact on nuclear decays [192, 193]. While many forms of nuclear decay involve only interactions between the protons and neutrons bound in the nucleus, common modes of electroweak decay such as electron capture (EC) and internal conversion (IC) proceed through an interaction between the nucleus and the atomic orbitals and are therefore dependent on the atomic charge state. EC occurs when a proton in the nucleus absorbs an atomic electron and transforms into a neutron while simultaneously emitting a neutrino. IC occurs when an excited nucleus de-excites through the emission of an electron from the atomic orbital. Additionally, for other decay modes, such as β^+/β^- -decay, the emitted lepton can interact with the atomic orbital which can affect the resulting emission spectrum.

The half-lives of these decays can be significantly altered and even be blocked by removing electrons from the atomic orbitals. For example, Litvinov *et al.* [192] studied the EC decay constant in helium-like (two electrons) and hydrogen-like (one electron) charge states of ^{140}Pr . In comparison to neutral ^{140}Pr , the authors found that helium-like ^{140}Pr decay rates were a factor ~ 3.3 slower while hydrogen-like ^{140}Pr decay rates were only a factor ~ 2.3 slower. This counterintuitive result where the hydrogen-like decay rate is faster than the helium-like decay rate is explained by accounting for conservation of total angular momentum of the nucleus-lepton system. For the case that all electrons are stripped from the atomic nucleus, the IC and EC decay modes are completely blocked. These effects on decay life-times can have a significant impact on astrophysical reaction rates where temperatures are hot enough to fully ionize atoms. A prominent example is that of ^7Be in the core of the sun which plays

an important role in the hydrogen burning sequence [194].

Generally speaking, very few radioactive HCI decay spectroscopy experiments have been performed to date. This is due to the inherent difficulty of combining the techniques for RIB production, charge breeding, and decay spectroscopy into one experiment. Most studies have been performed at the experimental storage ring (ESR) at GSI in Darmstadt, Germany [195]. TITAN operates a decay spectroscopy program using radioactive HCI produced by a device called an Electron Beam Ion Trap (EBIT). An introduction to the EBIT as a charge breeder of HCI is given in the next section.

6.2 Introduction to the Electron Beam Ion Trap (EBIT)

The EBIT falls under a class of devices known as Electron Beam Ion Breeders (EBIBs) which use electron impact ionization to create HCI [196]. Electron impact ionization occurs when the kinetic energy of a free electron colliding with a bound electron is enough to overcome the ionization potential of the atom [197]. EBIBs utilize electron impact ionization to breed HCI by introducing a cloud of trapped ions to a high-density, high-energy, monoenergetic electron beam [196]. The operating principle of an EBIB is shown in Figure 6.1. The electron beam is generated by a cathode and is compressed into a high density using a magnetic field oriented along the beam axis. This electron beam is focused into an ion trap where ions are stored in a localized position and the electron impact ionization can occur. Axial confinement of the ions is achieved using a segmented electrode structure to create an axial potential well and radial confinement is provided by the radial space charge potential of the electron beam in combination with the strong magnetic field. As the ions are ionized into higher charge

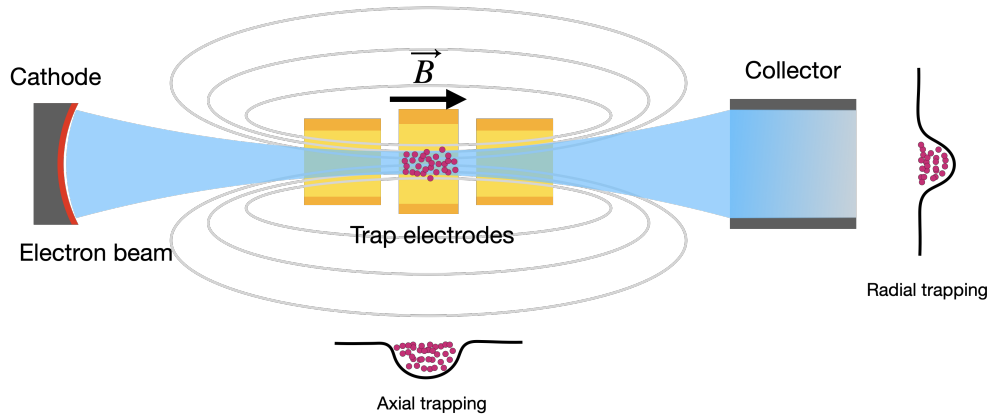


Figure 6.1: An illustration showing how an EBIB uses electron impact ionization to create HCI. A magnetic field compresses an electron beam that is focused onto a cloud of ions. The ions are held in a localized region by an axial trap defined by an electrode structure and a radial trap due to the electron beam space charge.

states, they are further trapped because they must overcome a larger potential barrier to escape the trap. Downstream from the ion trap, the electron beam is captured by a collector electrode.

EBIB devices are used for two different purposes and can therefore be specified with two designations: as an ion trap (EBIT) and as an ion source (EBIS). EBIS devices were designed first and have historically been used to quickly produce HCI for external devices [198]. Along with the Electron Cyclotron Resonance Ion Source (ECRIS), EBIS devices are now installed at multiple RIB ISOL facilities worldwide as a part of the accelerator infrastructure [196,199–201]. These charge breeding devices are installed directly after the isotope production stage but before the post-acceleration stage. The benefit they provide is because the attainable final beam energy is directly proportional to the charge state Q and Q^2 for linear accelerators and cyclotrons, respectively [196]. This allows ISOL facilities to develop smaller and more efficient medium- and high-energy beam post-acceleration infrastructure.

The EBIT was developed out of a desire to adapt an EBIS to perform X-ray spectroscopy on HCl stored in the trap [202]. The details of how this is achieved are introduced in the next section. TITAN is the only setup at a RIB facility which operates an EBIT coupled to an ion trapping setup rather than as accelerator infrastructure. Although the TITAN EBIT design is more closely associated with an EBIT than an EBIS, it can operate as both a source and a trap for HCl. As source, the TITAN EBIT produces radioactive HCl for mass measurements at the Measurement Penning Trap (MPET) [191]. As an ion trap, the EBIT produces and stores radioactive HCl for in-trap decay spectroscopy experiments. The next section introduces the TITAN EBIT.

6.3 The TITAN EBIT

The TITAN EBIT was built at the Max Planck Institute for Nuclear Physics (MPIK) in Heidelberg, Germany and commissioned at TITAN in 2008 [136]. It was designed alongside its sibling the FLASH EBIT¹ [203] as a mobile cryogen-free EBIT capable of visiting other facilities to perform experiments. In the case of the FLASH EBIT, this allowed transport to the Free-electron Laser (FLASH) at the Deutsches Elektronen-Synchrotron (DESY) in Germany and the Stanford Linear Accelerator (SLAC) in California. The essential pieces of their designs, such as the electron gun and collector assemblies, are based on their predecessor, the Heidelberg EBIT [204]. The three main components of the TITAN EBIT shown in Figure 6.2 are the ion trap, the electron gun and the collector. The following sections first discuss how the electron beam is generated by the electron gun and collector, and then discuss how the ions are trapped in the ion trap. Then we explicitly discuss how the EBIT is operated to produce HCl. A more detailed discussion of the TITAN EBIT can

¹Formerly known as the TESLA EBIT.

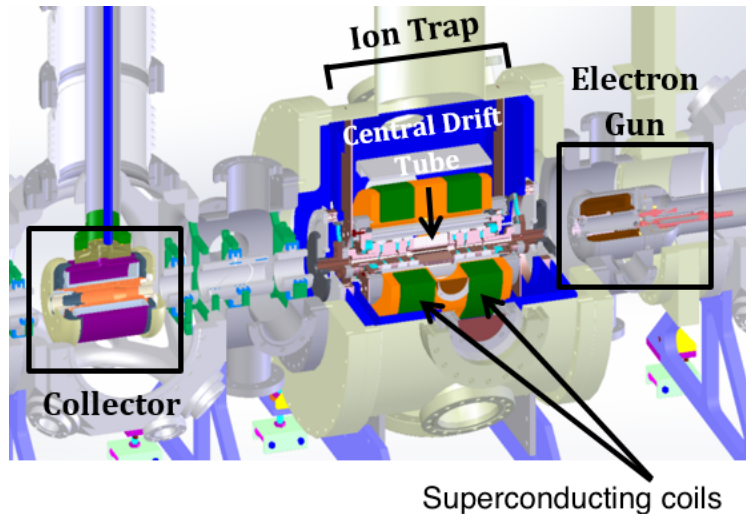


Figure 6.2: A sectioned view of the TITAN EBIT highlights the main components. Ions are stored in the ion trap and ionized by a high-density, high-energy electron beam generated by the electron gun and collector. Figure from [205].

be found in the thesis of M. Froese [205] and the EBIT commissioning publication [136].

6.3.1 Electron gun and collector

The rate of ionization of an ion in the i -th charge state by electron impact is given by the relation [206],

$$R_i^{\text{EI}} = \frac{J_e}{e} N_i \sigma_i^{\text{EI}} f(e, i), \quad (6.2)$$

where J_e is the electron beam current density, e is the electron charge, N_i is the ion density, $f(e, i)$ is an overlap factor between the electron beam and ion cloud, and σ_i^{EI} is the electron impact cross section which can be calculated using semi-empirical formulae such as the Lotz formula [197]. Through Equation (6.2), we can see that maximizing the current density, the density of ions, and the ion-electron overlap factor are necessary for a high charge breeding efficiency. Achieving a high current density starts with the design of the electron gun.

At the heart of the EBIT electron gun is the cathode which generates electrons by thermionic emission. Thermionic emission occurs when the cathode has been heated to sufficiently high temperatures that electrons are emitted from the cathode surface. TITAN uses a barium-impregnated tungsten cathode that is coated with an osmium-ruthenium mixture (Heat Wave M-type cathode) to reduce the threshold temperature for electron emission [205]. These cathodes are well known for their durability and have operational lifetimes of up to 10,000 hours. This cathode is operated at temperatures in the range of $\sim 950 - 1200$ °C.

The design of an electron gun presents unique challenges because the electrons begin mostly stationary at the cathode surface and must be accelerated to high energies. The problem that must be overcome is that the space charge density of the electrons near the cathode surface is generally high and the Coulomb repulsion causes the beam to expand. To counteract this, the geometry of the electrodes can be specifically designed following a Pierce-type geometry which tightly focuses the beam while minimizing aberrations [207]. This geometry can be seen in Figure 6.3 where the four most important electrodes are labelled. The anode is highlighted in green and provides the potential to accelerate the electrons from the spherically concave cathode surface. The cathode holder and the focus electrode provide the geometrical surfaces to optimally shape the electron beam as it is extracted from the cathode surface.

In accordance with the semi-empirical optical theory of electron beams published by Herrmann [208], the radius of a thermionically produced electron beam that is optimally focused and guided into a magnetic field of strength B can be written as,

$$r_H = r_B \sqrt{\frac{1}{2} + \frac{1}{2} \sqrt{1 + 4 \left(\frac{8k_b T_c r_c^2 m}{e^2 r_B^4 B^2} + \frac{B_c^2 r_c^2}{B^2 r_B^4} \right)}}, \quad (6.3)$$

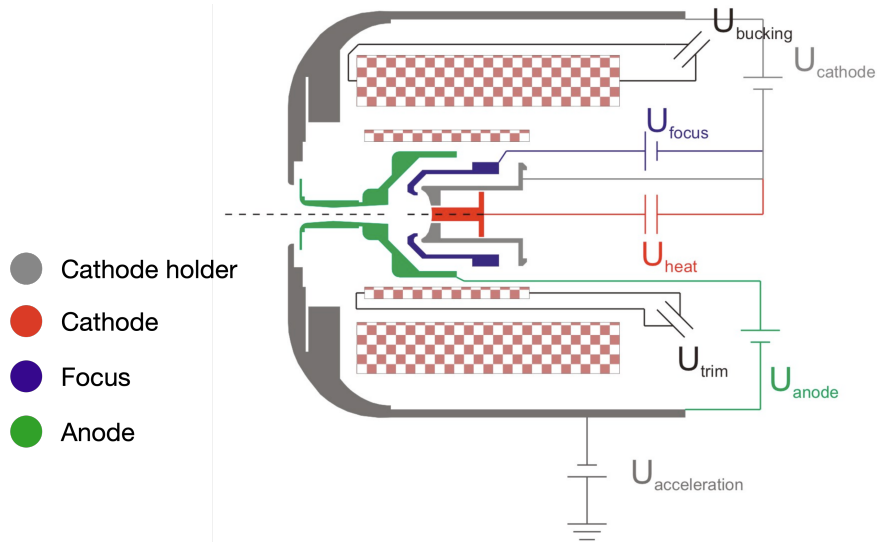


Figure 6.3: A sectioned view of the TITAN EBIT electron gun with the electrodes labelled. An electrical schematic showing the power supplies used to bias the gun are also shown. Modified from [205].

where T_c , r_c and B_c are the temperature of, radius of, and magnetic field at the cathode, and r_B is the Brillouin radius [208]. From this equation it can be seen that the Herrmann radius is minimized if the magnetic field at the cathode is zero. In accordance with Herrmann, the TITAN EBIT uses two magnetic coils situated around the electron gun to minimize the magnetic field at the surface. These coils are known as the trim and bucking coils and can be seen as the red-checked volumes in Figure 6.3. A plumbing system using water as the coolant is built into the gun to aid in the removal of heat generated by the electron gun assembly and magnetic coils. TITANs gun has been in operation since 2008 with one cathode replacement occurring in October 2021.

The electron beam is collected on the opposite side of the ion trap by a water-cooled collector assembly shown in Figure 6.4. At the center of the collector and with the largest surface area is the collector electrode which is where the kinetic energy of the electrons

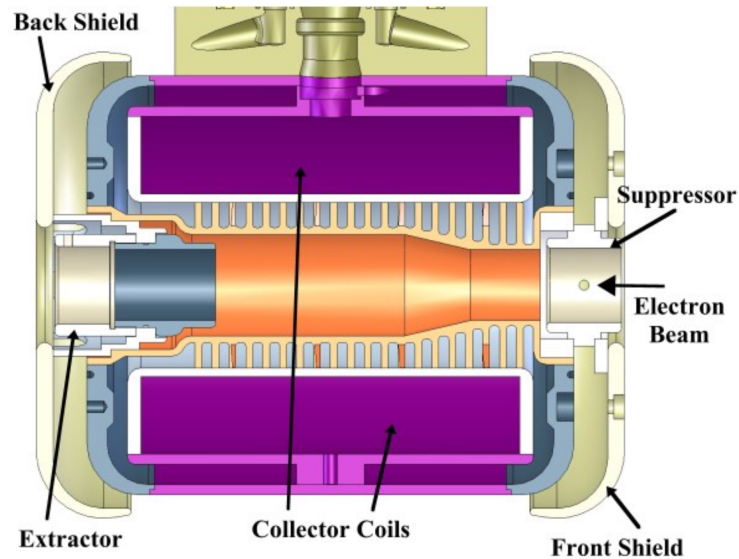


Figure 6.4: A sectioned view of the collector with electrodes labelled. Figure from [205].

is converted to heat and dissipated by the water cooling system. Two smaller electrodes known as the suppressor and extractor are installed on either side of the collector electrode. Furthest from the trap center is the extractor electrode which creates a potential barrier to prevent any electrons from passing through the collector assembly. Closest to the trap center is the suppressor electrode which is used to ensure secondary electrons are collected on the collector electrode and do not travel back into the trap center. Secondary electrons are those that are produced as a result of the primary electrons impacting onto the collector electrode surface. To aid in field decay and electron collection, a magnetic coil is used to de-focus the electron beam as it enters the collector.

6.3.2 Ion trap

An EBITs ion trap is a complex system that is used to facilitate the passage of a high energy electron beam, house a structure for applying the magnetic field which compresses

the electron beam, and trap the ions for optimal charge breeding conditions. This section introduces the various aspects of the ion-trap design.

During charge breeding, there are a number of processes that are competing to recombine with the HCl, chief among these being charge exchange with residual gas atoms in the ion trap. Because of this, maintaining ultra high vacuum (UHV) conditions is necessary in the trapping region. At TITAN EBIT this is realized by maintaining 2×10^{-9} mbar [205] with a system of roughing pumps and turbomolecular pumps. To improve the overall vacuum performance and reduce outgassing from material surfaces, the EBITs ion trap uses a cryogen-free two-stage Gifford-McMahon cryo-cooler which is thermally coupled to the superconducting magnet and trap electrodes. A specific advantage of using this system is that residual condensable gasses will be captured on the interior walls of the trap such that they do not interfere with the charge breeding process. The cold head holds the trap center at approximately 4.5 K [136].

The cryo-cooler is actually part of the superconducting magnet structure that was designed and built for TITAN by Cryogenic Ltd. The magnet structure consists of a pair of superconducting coils which are configured in a semi-Helmholtz geometry. The first stage of the cryo-cooler is cooled to 25 K and connected to a thermal shield around the magnet, while the second stage is directly attached to the magnet coils and is cooled to 4.5 K. The maximum magnetic field that can be supported by this system is 6 T at the trap center. A sectioned view of the drift tube assembly is shown with labelling in Figure 6.5. The outermost drift tubes, DT1 and DT9, are referred to as the trumpet electrodes and serve as the interface between the room temperature chamber and the first stage of the cryo-cooler. The outer portions of the trumpet electrodes are machined from stainless steel to prioritize reflection of infrared radiation, while the inner portions are machined from copper and are

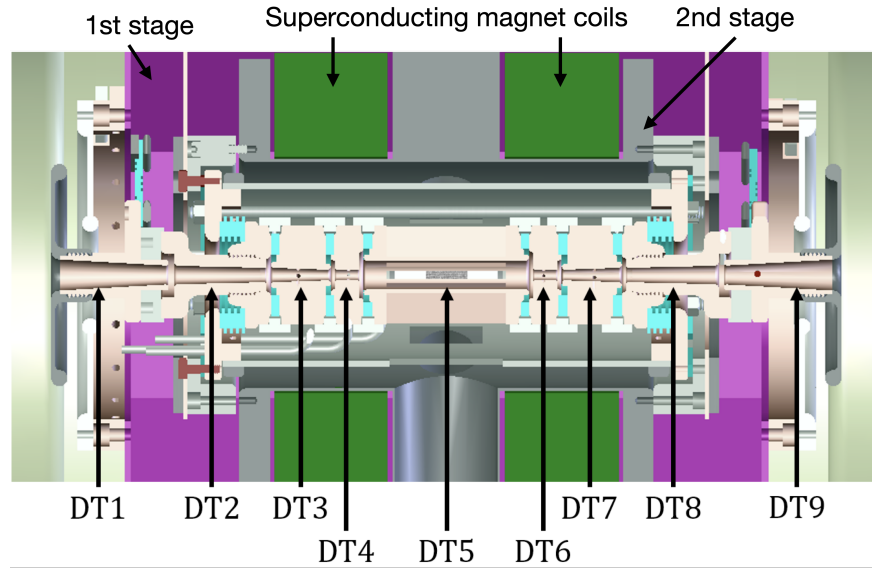


Figure 6.5: A sectioned view of the drift tube (DT) assembly through which the electron beam passes. Each DT is labelled as well as the location of the cryo-cooler stages and the superconducting magnet coils. Figure from [209].

thermally coupled to the second stage of the cryo-cooler.

The drift tube assembly is composed of nine electrodes that are individually biased to control the ion injection and trapping dynamics. The primary usage is to create an ion trapping potential (well potential) centered on DT5 with barriers provided by DT4 and DT6. Shorter and longer trapping potentials can be used by creating these well potentials on shorter drift tubes or across multiple drift tubes. A unique design of the TITAN EBIT is the central DT5 which is azimuthally segmented into eight pieces to form an octupole. This design was chosen to allow flexibility to the setup for future techniques to be developed at TITAN [205]. This includes techniques like resistive cooling of the ion bunches using small bandwidth RLC circuits, radio frequency excitation schemes for beam cleaning, and the setup of quadrupole or octupole traps.

The ion trap offers a number of unique features that enable an in-trap decay spectroscopy

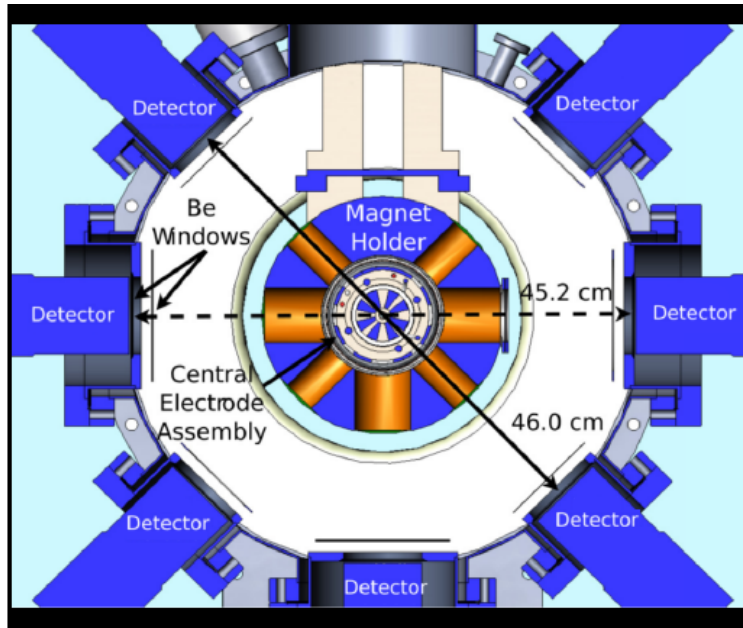


Figure 6.6: A cross-section of the EBIT ion trap showing the radial access that photon detectors have to the trap center. Figure modified from [210].

program at TITAN. Figure 6.6 shows a cross-section of the EBIT ion trap and identifies the seven spots where detectors are installed radially around the trap. The line of sight into the trap center for photon spectroscopy is enabled via specifically machined 35 mm apertures through each of the octupole segments of DT5 as well as radial bores through the magnet housing and the first and second cryo-cooler stages. To maintain UHV and cryogenic temperatures in the trap center, thin beryllium windows are installed on the radial bores of the first and second cryo-cooler stages. The outermost vacuum chamber of the EBIT has radial ports which also have beryllium windows. This makes for a total of three beryllium windows that isolate the trap center from atmosphere. On each port, the innermost windows are $25\ \mu\text{m}$ thick and the two outermost windows are $500\ \mu\text{m}$ thick.

A species can be introduced into the ion trap for charge breeding in two different ways.

One way, discussed in Section 6.3.3, is by injecting a beam of singly charged ions along the axis of the beam into the trap. The other way is to inject a collimated neutral atomic beam into the trap from the radial direction. To do this, one of the detector slots in Figure 6.6 is replaced with a two-stage differentially pumped gas injection system that is mounted onto the vacuum chamber [205]. To allow entry of the collimated beam into the trap center, the beryllium windows on the first and second cryo-cooler stages are replaced with metal discs featuring narrow slits. The collimated atom beam crosses the electron beam and is ionized as ions are trapped. Section 6.6.3, presents the preliminary results of an experiment that was performed using argon gas injected with this system.

6.3.3 EBIT Operation

The charge breeding of RIB bunches is illustrated in Figure 6.7. RIB bunches from the TITAN RFQ cooler-buncher are injected into the EBIT from the side of the collector. To ensure that the ions are injected into the trap center, the bunch can be steered and focused using a split Einzel lens (not shown) that is installed between the collector assembly and the ion trap. The central electrode of the Einzel lens is segmented into four individually biased pieces to allow for steering of the beam in the x and y directions [205]. Trapping of the ion bunch is performed by creating a well potential shown in Figure 6.7. During injection, the collector-side barrier is briefly lowered to allow entrance of the RIB bunch and then quickly raised to re-establish the trap. Quick switching of the electrodes is facilitated by TRIUMF-built high voltage switch boxes containing solid-state Behlke™ switches controlled by a programmable pulse generator (PPG).

Once the ions are trapped, the time scale of charge evolution in the EBIT ranges from milliseconds up to seconds depending on the desired charge state [211]. The complex

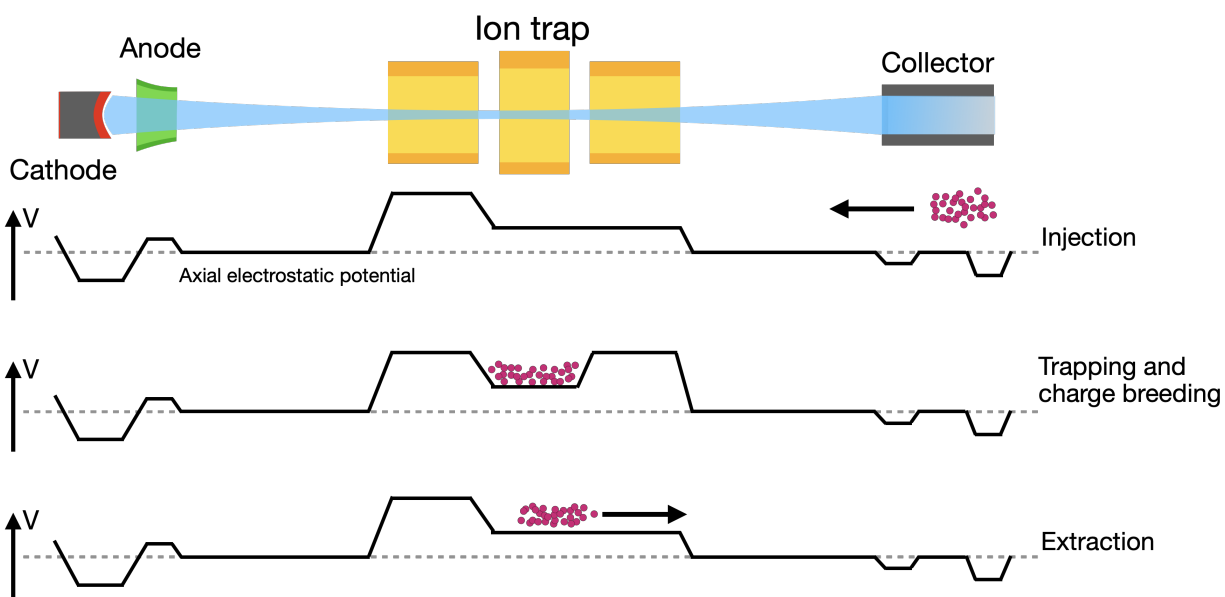


Figure 6.7: An illustration of the axial electrostatic potential during EBIT operation.

dynamics of charge state evolution in the trap are beyond the scope of this thesis. TITAN uses an in-house developed program called *ebitsim* to simulate the charge state evolution of ions in the EBIT. This program is implemented using Python and is available on the TITAN GitHub². The program implements various atomic physics phenomena such as electron impact ionization, radiative recombination, and charge exchange with residual gasses. For radioactive species, β -decay half-lives have been implemented into the code as well.

The HCI are extracted from the EBIT by lowering the potential barrier of the trap and simultaneously increasing the trap potential to apply a “kick”. It is estimated that this extraction contributes an energy spread of $10 - 100 \text{ eV}/Q$ to the HCI bunch during extraction [212]. Some of this energy spread can be mitigated by applying different trapping and extraction schemes which are programmed with the PPG. For example, instead of trapping

²<https://github.com/TITANCollaboration>

on the central drift tube (DT5), the ions can be trapped on a barrier electrode (e.g. DT6), which provides tighter axial confinement of the ions. The electrodes can also be programmed for voltage ramping schemes. This allows the voltage to be changed slowly or quickly over the course of a programmed time span. On the central drift tube, the voltage ramping shape is controlled by an Arbitrary Function Generator (AFG). This allows more complex schemes than just a linear voltage ramp to be implemented.

A number of diagnostic tools are available to assist TITAN in determining what the charge state distribution of the ions are at a given time. One reliable method is to extract the HCI from the trap and onto a microchannel plate (MCP) detector which is downstream in the TITAN beamline. Using the time-of-flight of the ions, the mass-to-charge ratio can be used to identify the different charge states present. This diagnostic is used to determine the optimal EBIT cycle times for preparing a desired charge state for a mass measurement at TITAN's Measurement Penning Trap.

6.4 In-trap decay spectroscopy at the EBIT

The EBIT as an in-trap decay spectroscopy tool for radioactive HCI was first demonstrated by using an array of X-ray and β particle detectors to perform measurements of electron capture branching ratios in ^{107}In [213] and ^{124}Cs [214].

These commissioning experiments were performed towards measurements of the small EC branching ratios of intermediate nuclei in $\beta\beta$ decay and are an important asset in calculations of nuclear matrix elements for searches of neutrinoless double-beta ($0\nu\beta\beta$) decay [215]. These first experiments highlighted some important benefits of implementing an in-trap decay spectroscopy program at an EBIT, which are outlined here, but also discussed in [210, 216].

For radioactive species on the neutron-rich side of stability, β^+ -decay tends to produce a significant background of 511 keV photons due to positron-electron annihilation. This background can obfuscate experiments which seek a high-sensitivity environment to measure decay signals with small branching ratios. The primary benefit of performing the decay spectroscopy in the EBIT is that the strong axial magnetic field spatially separates charged particles (α , e^\pm , and p) and guides them away from the trap volume [216]. At TITAN EBIT, this was shown to suppress the 511 keV annihilation background by a factor of 20 [216].

The EBIT also demonstrated a large ion capacity, which for the measurement of small branching-ratio decays is important for gathering enough statistics within a reasonable amount of time. The total trap capacity of the ion trap is roughly determined by the compensation of the electron beams negative space charge with the positively charged ions. For an electron beam of 500 mA beam current and 10 keV beam energy, the trapping region roughly contains 10^9 electrons [216]. For an average ion charge state of $Q = 30^+$, this implies that approximately 10^7 HCI can be stored in the EBIT trap. Because TITANs RFQ cooler-buncher is limited to extracting 10^5 singly charged ions per bunch, a multiple-bunch stacking scheme has been devised to fill the EBIT trap capacity [214]. Based on the technique by Rosenbusch *et al.* [217], the ion trap potentials are slightly lowered to allow the injection of the singly charged ions, but not enough to allow the HCI to escape. This is because the effective potential depth is deeper for HCI than for SCI. The trapping potentials are illustrated in Figure 6.8.

The second topic of this thesis covers the assembly and commissioning of a new spectroscopy array for the in-trap decay spectroscopy program. This array uses a suite of high-purity germanium (HPGe) X-ray and γ -ray detectors and will be used for two newly proposed experiments. The two experiments that are currently envisioned for the setup are

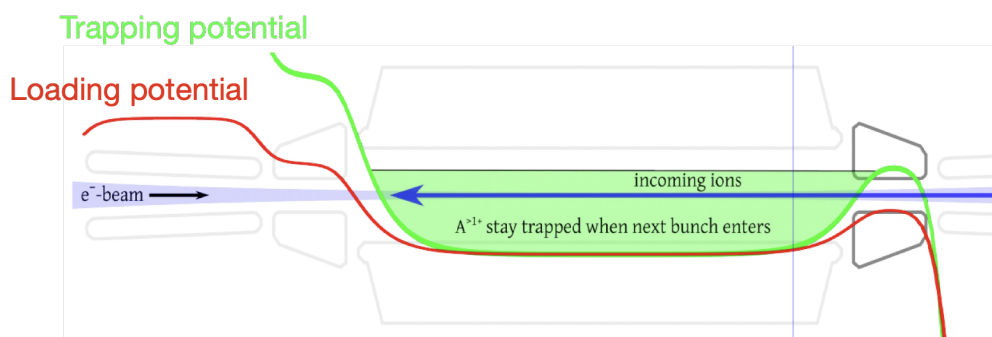


Figure 6.8: An illustration of the trapping and loading potentials used during the multiple injection technique. Figure from [209].

S2175 (Nuclear two-photon emission unveiled through suppression of first-order decay processes) and S2128 (Controlled stimulation of nuclear excitation via electron capture in the TITAN EBIT).

6.5 The new HPGe detector array for in-trap decay spectroscopy

This section gives a brief introduction to high purity germanium (HPGe) detectors for photon spectroscopy and unless otherwise noted, most of the material is sourced from the excellent textbook by Glenn F. Knoll [155]. Silicon and germanium semiconductors have a long history of being used as the solid-state detection medium for charged particle, X-ray, and γ -ray spectroscopy. A primary reason for this is that, in contrast to insulators and conductors, semiconductors provide a small gap ($\sim 1\text{ eV}$) between the valence and conduction bands which is exploited to liberate many charge carriers and achieve high energy resolution. The charge carriers in these materials are known as electron-hole pairs because they consist of electrons liberated by ionizing radiation or thermal energy and the

corresponding electron vacancies. Small levels of atomic impurities in the semiconductor material tend to create substitutional sites within the band gap which strongly influence the electrical properties of the material. Methods of doping the material with donor (pentavalent) and acceptor (trivalent) atoms have historically been used to compensate these impurities. Modern techniques have allowed for the fabrication of high purity germanium crystals with incredibly low impurity concentrations (< 1 part per 10^{12}). This HPGe material is designated mildly p-type (n-type) if the residual impurities in the crystal are acceptors (donors). In the case of a p-type (n-type) material, the electrical conductivity is mostly determined by the flow of holes (electrons).

The three major interactions responsible for the deposition of a photons energy into a semiconductor detector are Compton scattering, pair-creation and the photoelectric effect. Germanium is chosen as a suitable detection medium because it has a high atomic number ($Z = 32$), a small band gap energy of ~ 0.7 eV, and the crystals can be grown to sizes as large as 100 cm^3 in volume. To enhance detection efficiency and energy resolution, the germanium crystals are typically reverse biased. This bias creates a depletion region where the charge carriers generated by the incident photons experience minimal recombination and are efficiently collected. The germanium crystals are also cooled to cryogenic temperatures using liquid nitrogen, which serves to reduce thermally generated noise and improve energy resolution.

The charge carriers liberated by the incident photons are drifted in the electric field created by the high voltage bias which generates a current pulse. This current pulse is amplified using a charge-sensitive integrating preamplifier to create a voltage pulse which is then shaped in preparation for digitization. Using fast voltage digitizers, the pulse heights are recorded and used to build a histogram of the photon energy spectrum. This signal

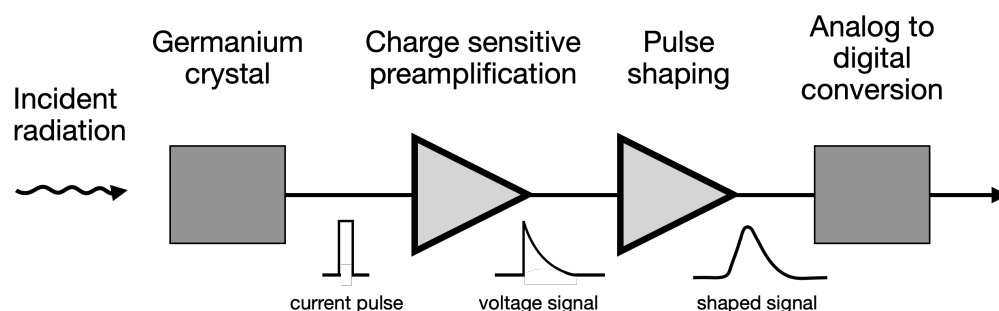


Figure 6.9: A diagram showing the basic signal processing chain of the detectors used at TITAN. The signal is generated in the HPGe crystal, preamplified, shaped, and finally converted to a digital signal for storage.

processing chain is illustrated in Figure 6.9.

For our purposes, two different types of HPGe detectors are installed onto the array to allow for observation of two different photon energy regimes, X-ray and γ -ray. The X-rays are produced by atomic transitions and electron-ion interactions in the EBIT trap, and the γ -rays are produced by nuclear decays and transitions in the radioactive nuclei. X-ray energy ranges from 1 keV to 100 keV, and γ -ray energy ranges from 100 keV up to a few MeV.

6.5.1 HPGe γ -ray detectors

The γ -ray detectors are n-type coaxial (EG&G Ortec GMX 23200-S) detectors designed by Ortec in the mid-1980s. The official manufacturer name for the detectors is the “duet detector” because these were designed to be paired with BGO scintillators for active Compton suppression. These detectors were originally used in the 8π spectrometer [218], but after its decommissioning, the detectors were moved to the Nuclear Science Laboratory (NSL) at Simon Fraser University (SFU). One detector is permanently stationed at TITAN while additional detectors are available for short-term loan from SFU during experiments.

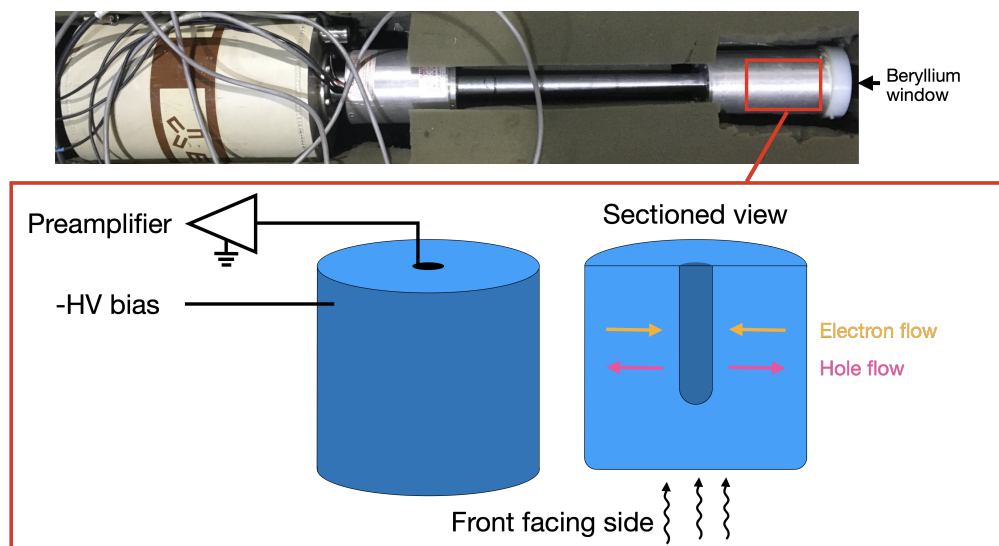


Figure 6.10: (top) A picture of one of the γ -ray detectors. (bottom) An illustration of the coaxial geometry HPGe crystal used by the γ -ray detectors.

An image of one of the detectors is shown in Figure (6.10) along with an illustration of the HPGe crystals coaxial geometry. Each crystal is 6 cm long and 5.3 cm in diameter, for an approximate detection volume of $\sim 130 \text{ cm}^3$. The crystals are mounted into a cooled cryostat which maintains cryogenic temperatures and is covered with a beryllium window to act as a heat and vacuum shield. To maintain cryogenic temperatures, each detector is equipped with a 1.2L liquid nitrogen dewar. For detector operation, a negative high voltage (HV) bias is applied to the outer surface of the HPGe crystal. This applies a radially oriented field which drifts the electron-hole pairs liberated by the incident photons.

6.5.2 HPGe X-ray detectors

TITAN currently has two ultra low-energy HPGe X-ray detectors (GUL0110P manufactured by Canberra Inc.³). The HPGe crystals inside of these detectors are p-type planar crystals

³now called Mirion Technologies

which are approximately 10 mm thick and 11.3 mm in diameter. The crystals are fabricated with a very thin front-facing contact and mounted in a cryostat with a very thin 0.025 mm beryllium window. These features maximize X-ray detection efficiency because the amount of dead layers between the X-ray source and the sensitive volume of the HPGe crystal is minimized as much as possible.

Photon absorbing material between the detector and source are further minimized with a special mounting design shown in Figure 6.11. This design allows photon sensitivity down to 1 keV and as low as 300 eV if the cryostat window is removed. The entire detector system is mounted onto an extendable slide table and the detector crystal is installed into a flexible bellows with a flange at the end. This setup allows for mounting of the detector onto a vacuum chamber where it occupies the same vacuum as the photon source. This also allows the detector to be extended into the bore of the EBITs magnet assembly which increases the solid angle coverage. To maintain cryogenic temperatures, each detector is equipped with a 7.5 L liquid nitrogen dewar.

6.5.3 Mounting the detectors onto the EBIT

This section explains how the detectors were mounted onto the EBIT. Before mounting, these detectors were tested and compared to the manufacturers specifications. The results of the test are presented in Section 6.6.

There is currently one X-ray detector mounted onto the EBIT which can be seen in Figure 6.12. The other detector is on loan to the CANREB EBIS group working in the ARIEL facility at TRIUMF [199]. The detector slide table is seated onto a table that attaches to the side of the EBIT. Vibration dampening feet are attached between the slide table and the EBIT table to mitigate the effect of vibrations from the EBIT. The beryllium

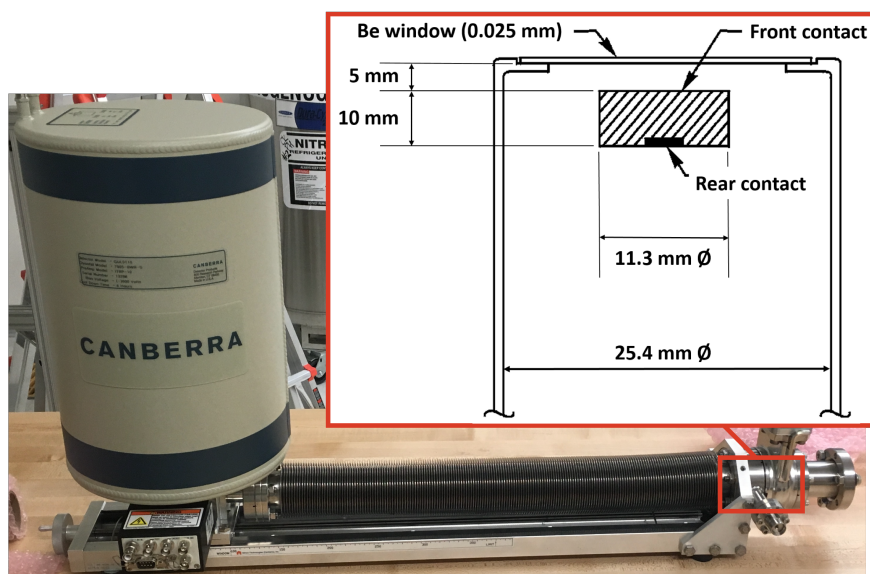


Figure 6.11: One of TITANs X-ray detectors (Canberra GUL0110P) shown when it was first being set up. The illustration shows the planar HPGe crystal inside of the cryostat.

window on the EBIT viewport is removed and replaced with a flange which adapts the CF 8" flange of the EBIT to the CF $2\frac{3}{4}$ " flange of the detector. The detector sits on this table and is then bolted onto the EBIT so that they share the same vacuum volume. To allow for extension of the detector element into the EBIT trap, the beryllium windows on the first and second cryo-cooler stages are replaced with small diameter nozzles which aim to reduce the thermal load on the magnet body. These nozzles allow just enough clearance for the detector element to pass through. Using the manual slide table, the detector crystal can be extended into the bore between the superconducting coils until it sits approximately 100 mm away from the trap center.

A mounting mechanism for the γ -ray detectors is not provided by Ortec, therefore a custom system is used to ensure proper mounting of the detectors onto the EBIT. A concern for the design of the mounting system was to minimize vibrations that would translate from

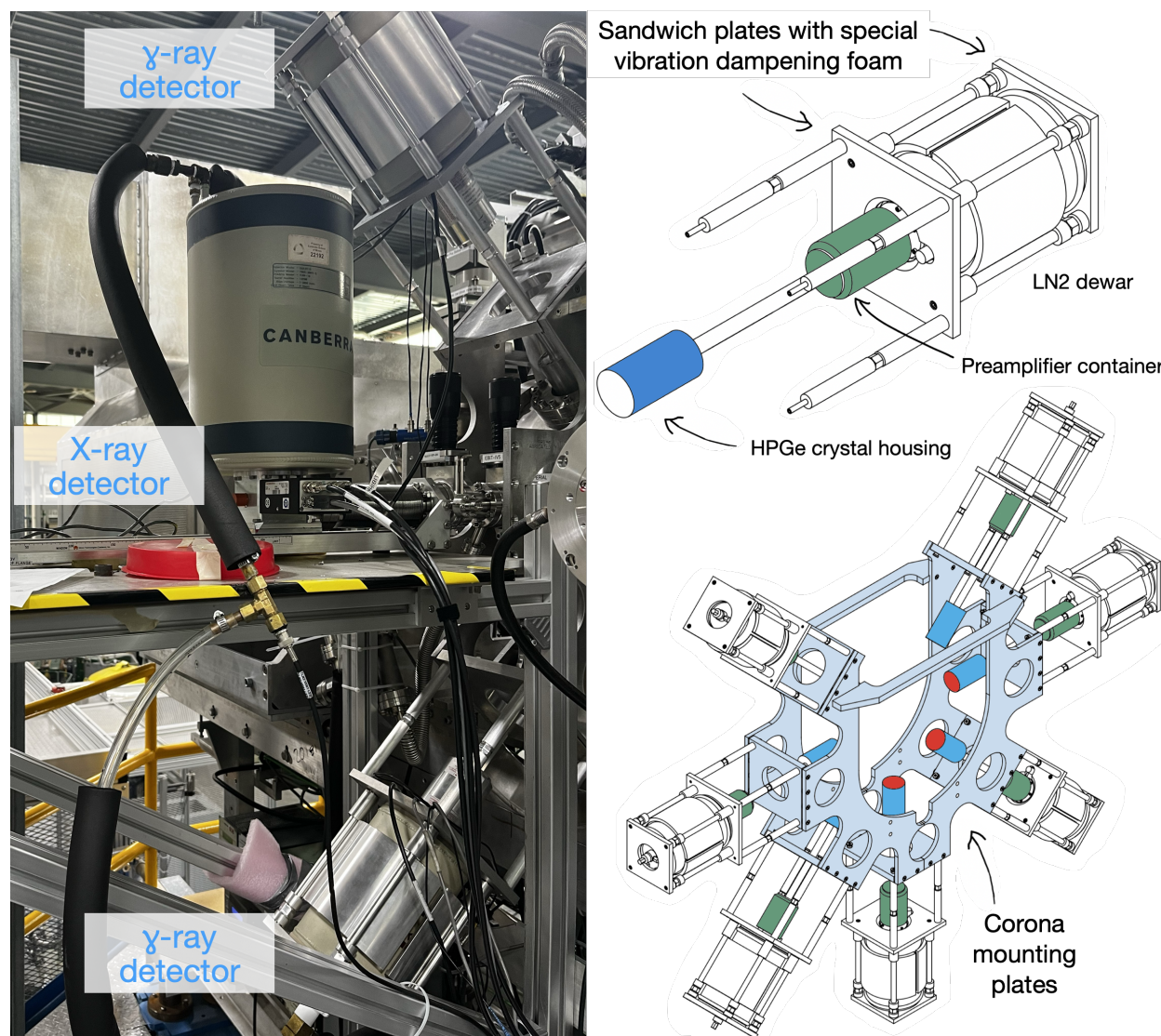


Figure 6.12: (left) Three detectors are shown mounted onto the EBIT. (right) Solidworks drawings of the γ -ray detector mounting solution. Each detector is securely fastened into a mounting bracket via the dewar and is then bolted onto the corona mounting plates which are installed on the EBIT.

the EBIT vacuum pumping system to the detectors. Vibrational insulation is achieved using a special clamp system that “sandwiches” the detector dewar between two insulation-lined plates. The insulation is a high-density polymer molded foam (Polymer Technologies Inc. PHDM-NS) designed for broadband frequency absorption. The “sandwich” clamp is then bolted onto the EBIT via the mounting plate. The mounting plate is held in place by a pair of corona mounting brackets which extend around the EBIT to all viewports. This mounting system can be seen in Figure 6.12. The mounting system is designed to eliminate the chances of accidental beryllium window puncture which would cause a vacuum failure in either or both the EBIT and the detector. In this configuration the γ -ray detectors are positioned at approximately 1.5 mm from the beryllium windows on the EBIT viewports.

To aid in the maintenance of the γ -ray detectors, a pair of mounting stands has been designed and machined, As shown in Figure 6.13, these stands allow experimenters to store the detectors in two different orientations next to the EBIT. In the case that the detectors need to be unmounted from the EBIT and tested for resolution or efficiency, the detectors can be mounted right side up and operated in the stands. If maintenance or adjustments to the preamplifiers are necessary, the detectors can be mounted into the stands in an inverted position where the preamplifiers are easier to access.

6.5.4 Liquid nitrogen filling system

The HPGe detectors need to be maintained at cryogenic temperatures using dewars that can be pressure-filled with liquid nitrogen (LN₂). This requires an automated fill system that can perform scheduled fills at regular intervals. The fill interval is set by the γ -ray detectors which have smaller 1.2 L dewars and require refills every six hours. Because of this relatively short time scale, the fill system needs to be robust so that minimal operator intervention is



Figure 6.13: The γ -ray detector stands for detector maintenance and calibrations. (left) The detector is mounted in an upright orientation which allows for access to the LN2 dewar and enough space under the detector for a calibration source. (right) The detector is mounted in an inverted orientation which allows access to the detector window and the preamplifier electronics.

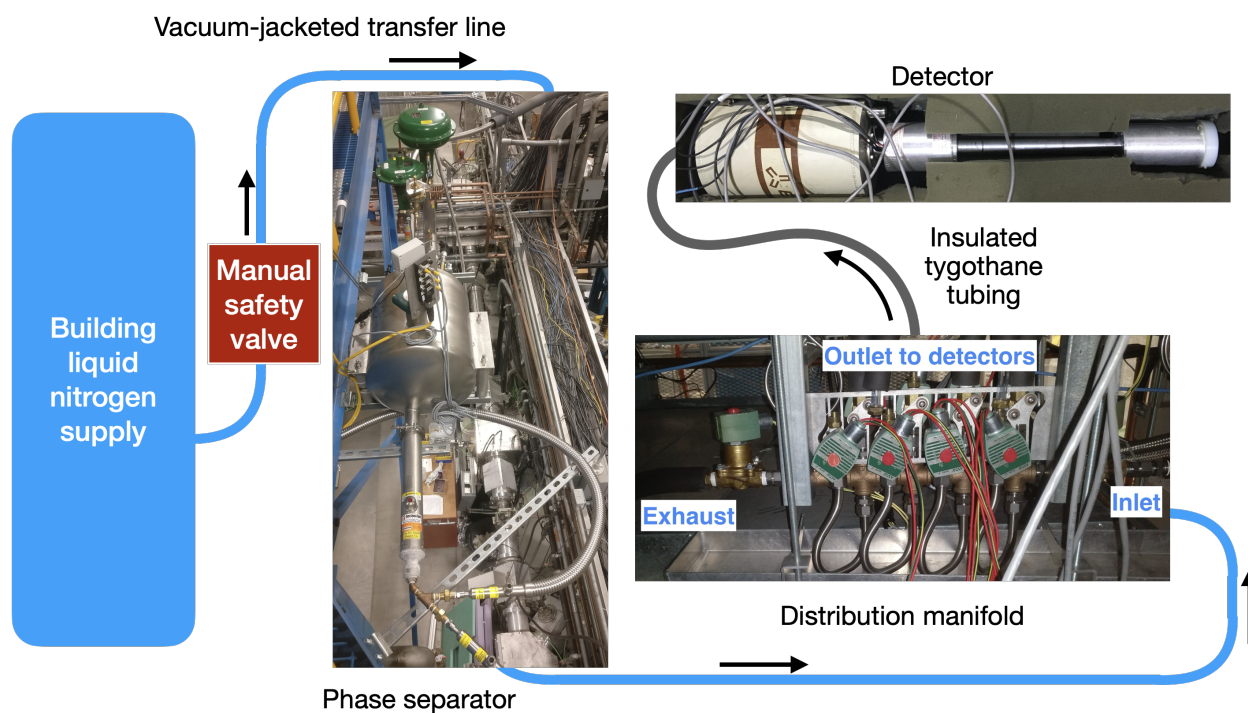


Figure 6.14: An illustration of the components of the liquid nitrogen autofill system.

necessary.

Previous iterations of the LN2 filling system used a Taylor Wharton 240 L LN2 storage tank placed below the TITAN platform. This dewar delivered pressurized LN2 up to a manifold which then distributed it to the detectors. The dewar was manually refilled every ~ 1 week using the building LN2 supply on the East side of the experimental hall. Two main problems with this system resulted in inconsistent LN2 filling times and a higher-than-desirable maintenance schedule. The first is that the pressure required to pump the LN2 up to the manifold introduced turbulence and gaseous impurities in the LN2. This effectively reduced the amount of LN2 that was actually being delivered to the detectors and therefore lowered the filling efficiency. The second is that the detector manifold design did not equally distribute the LN2 among the different detectors. Therefore it was decided to upgrade the LN2 system considering the following requirements: 1) It should improve filling efficiency by reducing the total time required to fill detectors, 2) it should be a robust system that requires minimal maintenance by TITAN personnel and 3) the system should supply LN2 to other cryogenic TITAN components such as MPET.

The new LN2 autofill system can be seen in Figure 6.14 where each of the components are highlighted. Each of the components are discussed below in more detail.

Phase separator

The first component of the LN2 system is the 22litre LN2 phase separator (Technifab Cryogenics PS-22-1B) which is mounted onto the side of the TITAN platform and shown in Figure 6.14. The phase separator is directly connected to the building LN2 supply using a vacuum insulated line. When the phase separator is not being used, this line is left charged, but can be closed via a manual shutoff valve at the building supply tank. By

providing better separation of gaseous impurities and more temperature stability, the phase separator is the first upgrade for delivering higher quality LN2 to TITAN systems. The phase separator currently delivers LN2 to MPET and the HPGe detector array. LN2 delivery to the detectors is managed by a newly installed manifold.

Detector manifold

The new detector manifold shown in Figure 6.14 in its final configuration mounted on the underside of the TITAN platform, distributes LN2 to the HPGe detectors. Inlet, outlet, and exhaust lines are controlled electronically with solenoid valves. The major difference between the new design and the previous design are the orientations of the outlets. The previous design was configured with LN2 outlets in the upward and downward orientations, which contributed an uneven distribution between the detectors. This resulted in inconsistencies during fills because some detectors would time-out their fill cycle before LN2 actually reached the dewar. This required manual monitoring of fills to catch the time-out and manually restart the fill. Outlets on the new manifold are all in an upwards orientation, resolving this issue and giving a uniform LN2 distribution across all outlets. The outlet lines to the detectors are made from a Tygothane™ thermoplastic polyurethane tubing which is insulated with a nitrile butadiene rubber foam. The tubing is attached to the manifold using brass Poly-Flo™ fittings which use a plastic compression ferrule to maintain a secure attachment.

Liquid nitrogen injection

The Canberra X-ray detector dewars are equipped with two ports with 1/8" NPT male barb fittings which are used for LN2 injection and exhaust lines. In this case, injection of LN2 into the dewars is as easy as attaching the Tygothane™ hose onto the ports and securing

them with hose clamps. This is a robust design which has not required any maintenance since it was first setup in 2021.

The Ortec γ -ray detector dewars only have a single open-ended port to which an LN2 injecting device must be connected. This LN2 injector must manage the inlet and exhaust flows while the detector is being filled. Figure 6.15 shows a picture of the original Ortec injectors that were supplied with the γ -ray detectors. The design features two concentric tubes serving as the inlet and outlet pathways. The inner tube is terminated with an inlet tip designed to disperse the LN2 onto the inner sides of the dewar rather than the inner bottom. This reduces turbulences that would generate nitrogen vapor. The outer tube is slightly recessed from the inlet tip acting as a sheathe. When the LN2 level in the dewar volume reaches the height of the outer tube, enough pressure builds up to start pushing LN2 out of the exhaust and the dewar is considered full. Because these detectors were originally purposed for the 8π array, the dewars have an internal structure that allows LN2 filling in multiple orientations. To achieve this, the inlet port contains a hollow tube that extends approximately 1/2 of the depth into the dewar. This ensures that the dewar is at least half-way full before the pressure is high enough to push LN2 out of the exhaust. Our initial testing with the Ortec injectors showed a high propensity for ice formation between the concentric tubes and the dispersion tip, reducing flow rates and eventually completely blocking flow. This required a de-icing operation to be performed every 3 – 10 days.

To overcome this icing issue, a new injector was designed. Figure 6.15 shows the new TITAN-designed injector that was inspired by a neighboring experiment, the GRIFFIN spectrometer. With the TITAN injector there are a number of changes to the design. First, the junction which threads the injectors on to the detector dewars is made from Polytetrafluoroethylene (Teflon) material. This design was chosen so that in the instance of

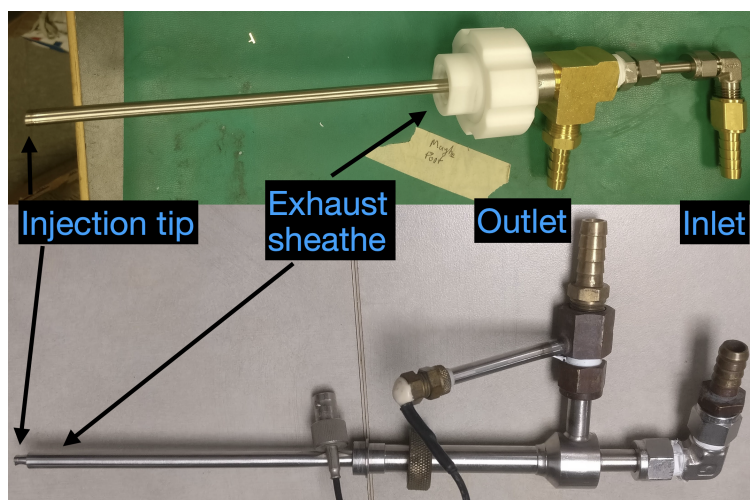


Figure 6.15: A comparison between the old (bottom) and new (top) LN2 injectors used with TITAN's γ -ray detectors.

failure of a component, the Teflon piece will break rather than the port on the dewar. This is to avoid the cost of replacing or repairing the LN2 dewars which are not standard components. The new design has also removed points where ice build-up is more likely to occur. This includes the removal of the exhaust sheathe and the dispersion tip of the inlet tube. With these changes, the TITAN injectors have demonstrated major improvements over the previous injectors. Since installation, there have been zero instances requiring de-icing of the TITAN injectors, and they have been demonstrated to fill in multiple orientations.

Operation

Liquid nitrogen transport and delivery systems are operated using a pre-cooling procedure where sections of the system are sequentially cooled before liquid is transported through them. At TITAN this is achieved with electronically controlled solenoid valves and a series of sensors to monitor temperatures at various points within the system. The sensors used in



Figure 6.16: The temperature sensitive green LEDs (P/N HLMP1790, Digikey P/N 516-1310-ND) used as temperature sensors in the LN₂ system. After soldering the leads, they are coated in a black moldable glue (Sugru™).

this case are temperature-sensitive green light emitting diodes (LEDs) placed in series with a 24 V DC voltage source and a 6.8 k Ω resistor. When the diode temperature drops in the presence of LN₂, its band-gap will increase and the voltage drop across it increases. Figure 6.16 shows an LED whose leads are coated in a moldable thermal glue being installed into the LN₂ system using a brass tee connector. Programmable Logic Controllers (PLCs) are used to monitor the voltage across the LEDs. The software for monitoring and operating an LN₂ fill is implemented using the Experimental Physics and Industrial Control System (EPICS) [219]. The control panels for both the phase separator and the manifold are shown in Figure 6.17

During a filling sequence the inlet valve between the phase separator and building supply is first opened. Because the LN₂ must travel from the opposite side of the experimental hall, approximately 20 minutes are required to cool down the vacuum-jacketed line and the phase separator. Once the phase separator starts to fill, about five minutes are required to fill its 22 liter capacity. A line level sensor indicates the fill capacity of the phase separator. When the level reaches a set level, the outlet valve opens to allow precooling of the detector

manifold.

During precooling of the manifold, the manifold exhaust valve is open allowing the pressurized N_2 to escape. As the manifold cools down, one of the LED sensors monitors the temperature at the exhaust. When liquid nitrogen reaches the exhaust, the voltage across the LED will be read as $\sim 7V$ and the exhaust valve is closed. The outlet valves simultaneously open to begin sending LN2 towards the detectors. The same LED exhaust system is used on each of the detectors to indicate when the detector dewar is sufficiently full. To prevent the build up of moisture in the system which hastens ice formation, one-way valves are installed onto the manifold and detector dewar exhausts. At the end of each fill, this traps N_2 gas in the system which prevents moisture from leaking in. A full LN2 filling procedure requires approximately 35 – 40 minutes in total when all detectors in the array are being used.

6.5.5 Electronics

Operation of an HPGe detector requires a high voltage power supply to bias the HPGe crystal, a power supply for the signal preamplification stage, and electronics to shape and digitize the signal into a photopeak histogram. This section discusses the electronics that were set up to operate the detectors. The full electronics rack is shown in Figure 6.18.

High-voltage biasing and signal preamplification

The γ -ray detector crystals require a bias voltage of $-2000V$ and the X-ray detector crystals require $-800V$. This biasing is performed by a CAEN R8034N programmable HV power supply (see Figure 6.18) which supplies up to 6kV on eight separate channels. Each channel takes an inhibit signal from the detectors which will kill the high voltage bias if the detector

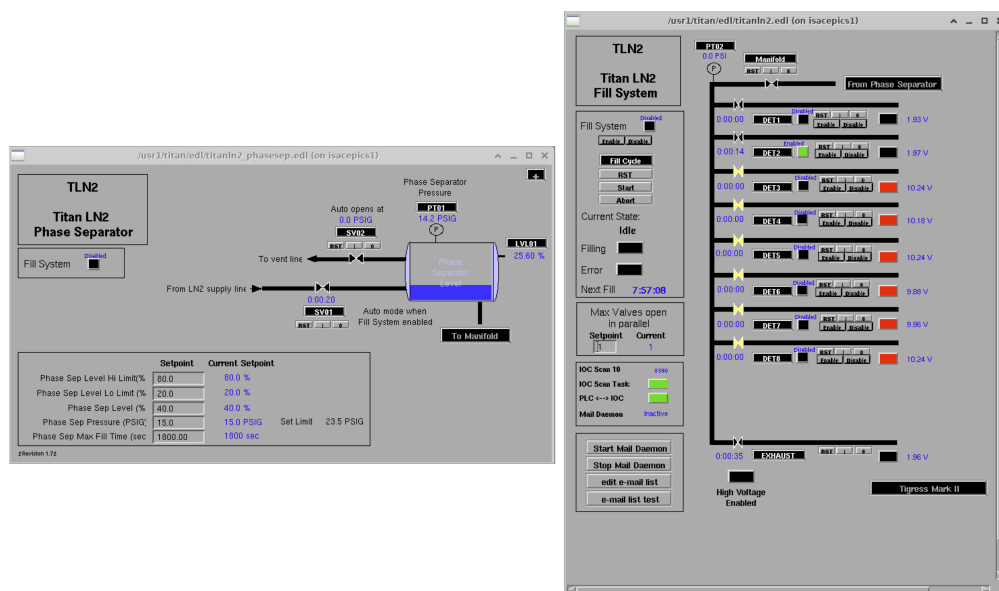


Figure 6.17: The software used to control the LN2 system is implemented using EPICS. The controller diagrams for the phase separator and detector manifold are shown in the left and right panels, respectively.

crystal warms up beyond a set threshold. This protects the detectors in the event that the liquid nitrogen fill system fails and someone is unavailable to unbias the system. The CAEN HV Wrapper Library⁴ was used to write a small program for controlling the module over Ethernet so that all detector biasing can be controlled remotely.

Preamplifier power is supplied with two CAEN N5424 modules (see Figure 6.18) which are installed inside of a Nuclear Instrumentation Module (NIM) crate. Each module can supply power for up to four preamplifiers, therefore leaving TITAN with some redundancy in the event that a channel fails. These supply modules work for all of TITAN's X-ray and γ -ray detectors as they have the same standard 9-pin connector configuration.

⁴<https://www.caen.it/products/caen-hv-wrapper-library/>

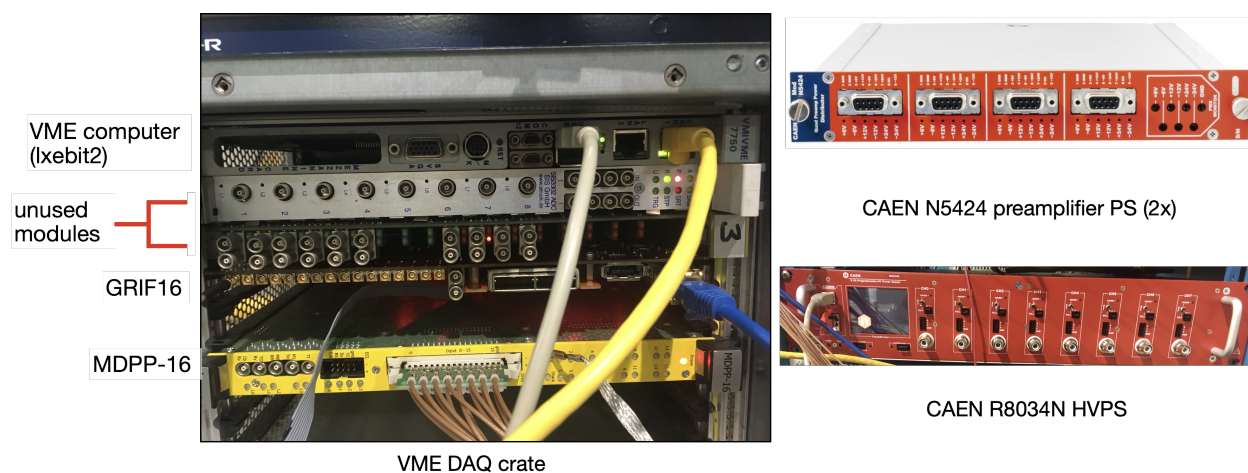


Figure 6.18: The electronics used to power and operate the detectors, and digitize the signals.

Digitization

The signal digitization process is dependent on what style of preamplifier is used in the detector. TITAN's detectors use standard charge-sensitive preamplifiers. These preamplifiers are sensitive to the current signal created by the photon deposition event and integrate it into a voltage pulse whose amplitude is proportional to the collected charge. A key difference between TITAN's γ -ray and X-ray detectors is the preamplifier feedback circuit. The γ -ray detectors use RC feedback while the X-ray detectors use a transistor-reset circuit designed to allow rapid signal processing in high count rate scenarios. These differences require two different signal processing methods for digitization.

The X-ray detectors use a Mesytec MDPP-16 fast time and amplitude digitizer [220]. This unit provides 16-bits of amplitude resolution at an 80 MHz sampling rate and can be synchronized with external devices to adapt to specific experimental needs. The device has a 16 MHz internal clock oscillator for timestamping events, but can receive an external clock up to 75 MHz. The γ -ray detectors use a specially designed GRIF16 digitizer which was

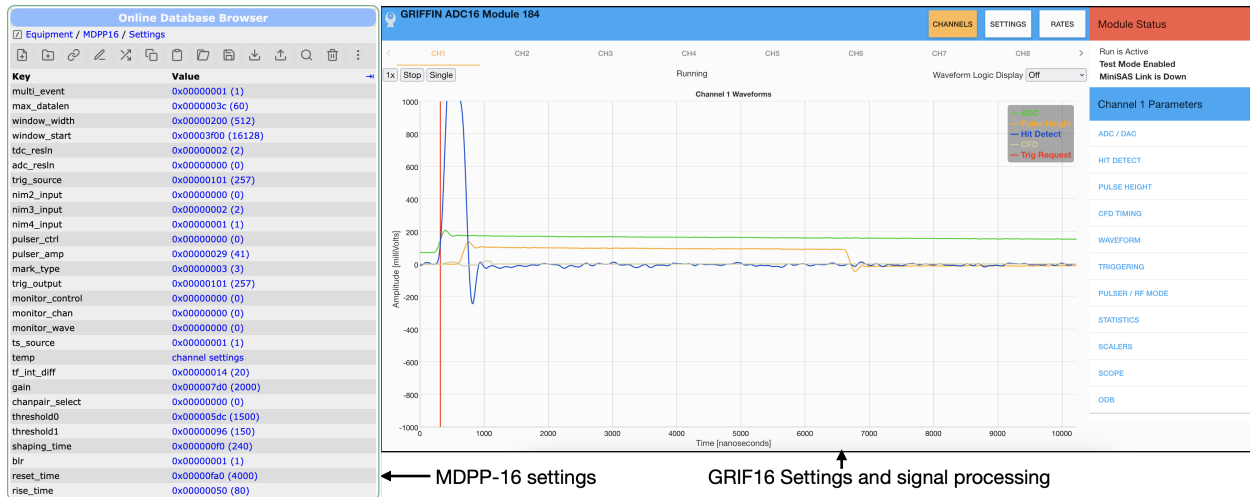


Figure 6.19: (left) The Online Database Browser (ODB) is used to change run settings for the MDPP-16. (right) The GRIF16 hosts a web interface where run settings can be changed and real-time signal digitization can be monitored.

developed in-house by the GRIFFIN Collaboration [221]. This digitizer provides 14-bits of amplitude resolution at 100 MHz with an internal clock oscillator that can be configured to run at up to 105 MHz.

Both devices are housed within and powered by a Versa Module Eurocard (VME) crate shown in Figure 6.18. With the MDPP-16, all communication and data forwarding is performed through the VME bus interface using an onboard VME computer (lxebit2). The GRIF16 has a front panel ethernet port, so all communications and data forwarding are performed over the TRIUMF network.

Both digitizers have their own internal clock oscillators that can be used to timestamp the photon data. However, it is ideal to synchronize the timestamping between the two data sets for post-experiment data analysis. To do this, the GRIF16 was flashed with a firmware upgrade that allows it to output a 50 MHz clock using a high-frequency UMC (ultra-miniature coaxial) connection. This clock signal is sent to the NIM3 input of the

MDPP-16. To synchronize the timing schemes between the EBIT and the X-ray detectors, the EBIT PPG is used to signal the MDPP-16 via the NIM2 input. This allows for an alignment between the photon timestamps and the timestamps of various EBIT actions such as opening/closing the trap or changing the voltage of a specific electrode. This is relevant for the measurement that is performed in Section 6.6.3.

Both digitizers have a signal processing stage where the signal is shaped before digitization. This is used to improve the signal-to-noise ratio and filter out any unwanted backgrounds that might interfere with the accuracy of the digitization process. To see how these settings are affecting digitization, one can monitor the photopeak histograms or look at real-time signal digitization if the digitizer allows it. To modify these parameters and monitor the real-time signal digitization, the GRIF16 hosts the web-interface shown on the right side of Figure 6.19. Modification of the MDPP-16 parameters is through the Online Database Browser (ODB) which is hosted by MIDAS (more about this in the next section). To view real-time signal digitization by the MDPP-16, an oscilloscope has to be hooked up to NIM connectors on the front panel and the MDPP-16 must be switched into an “oscilloscope” mode.

6.5.6 Data Acquisition

The setup of the DAQ system is outlined in Figure 6.20. For each digitizer, a separate frontend program is used to communicate run settings and to facilitate event data transfer. For the MDPP-16 this program is femdpp and it is installed on the VME computer lxebit2. For the GRIF16 this program is fegrif16 and it is installed in a computer called titan05. Titan05 is the decay spectroscopy computer used for DAQ control.

Management of raw data during the DAQ runs is performed using the Maximum

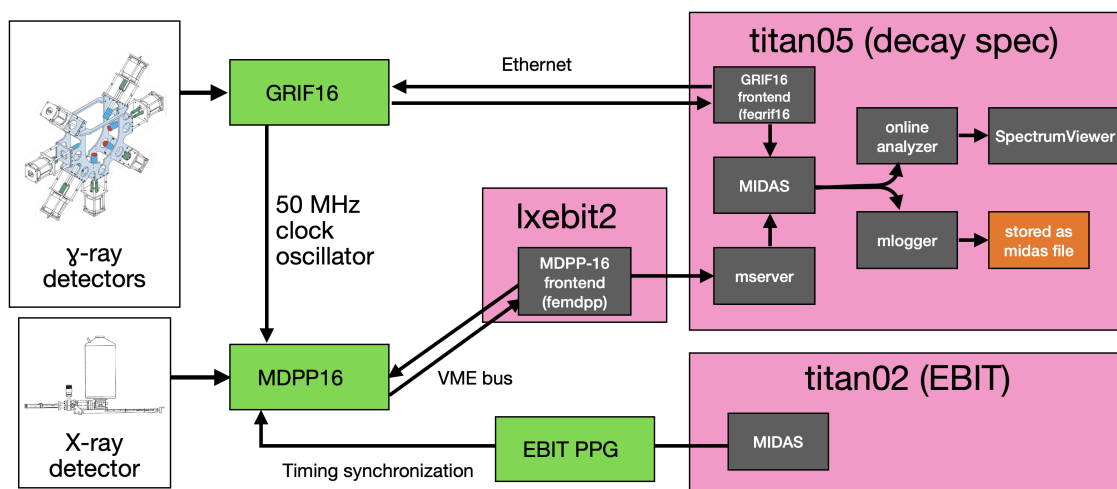


Figure 6.20: An illustration showing the setup of the DAQ system for decay spectroscopy at the EBIT.

Integrated Data Acquisition System (MIDAS) [222], which allows users to perform basic functions like starting/stopping DAQ runs, modifying digitizer run settings, facilitating data transfer, decoding and saving data from the digitizers, and on-line analysis with basic histograms. This is achieved with a suite of programs that run in the background to communicate with the digitizers, receive and decode the raw data, and log and save the data using the MIDAS encoding format. Interaction with MIDAS is performed through a web interface which is hosted by the midas program mhttpd. MSERVER is used to communicate with femdpp because it is installed on lxebit2 instead of titan05. The data from both front end programs is managed by the main MIDAS program which distributes to both MLOGGER and the online analyzer. MLOGGER compresses the data into a midas format for storage and the online analyzer decodes the data so that histograms can be built and viewed in real time. Spectrum Viewer allows experimenters to build and monitor histograms during the experiments. For a more detailed breakdown of the DAQ software, see [223].

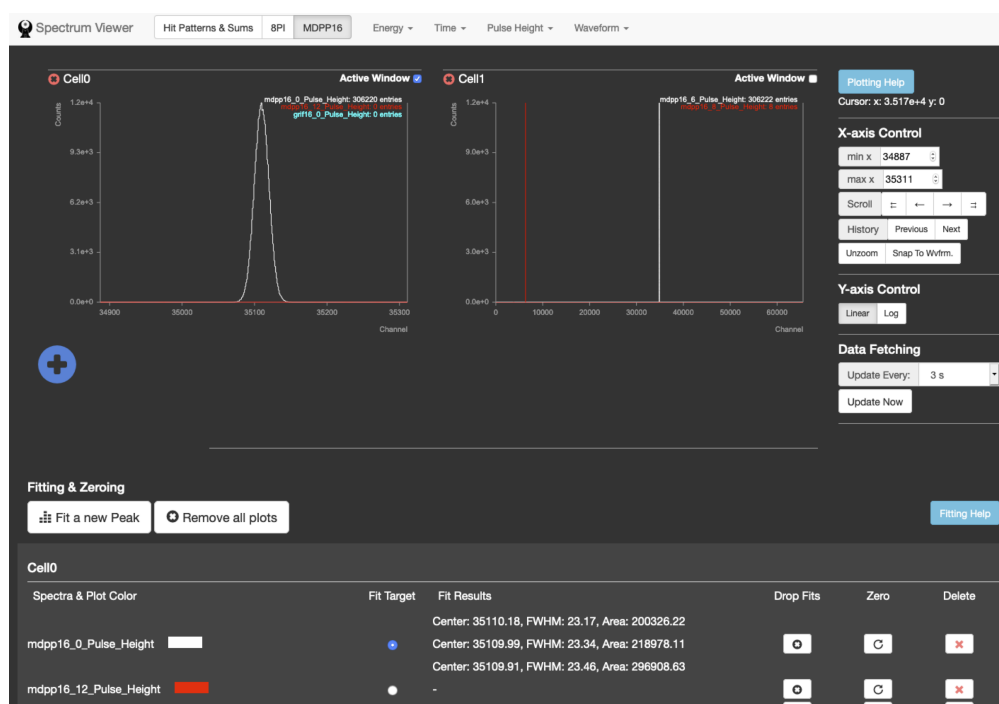


Figure 6.21: The Spectrum Viewer for viewing online data is shown. Spectrum Viewer can plot various histograms from multiple detector channels and perform basic Gaussian fitting of photopeaks.

6.6 Detector tests

The EBIT has not yet run a RIB experiment since the HPGe spectroscopy array was commissioned. However, the decay spectroscopy experiments that are planned at TITAN place a number of requirements on the EBIT and the spectroscopy setup. This section contains some tests that were carried out towards performing these RIB experiments. During the time of these tests, only two of the γ -ray detectors from SFU were available for testing.

6.6.1 Detector resolution

The most basic tests verified that the resolution of the detectors met the specifications stated by the manufacturers. The recorded spectra and the test results are summarized below.

γ -ray detectors

The energy resolution of two γ -ray detectors (S/N 25-N50RB and 25-N1370B⁵) was determined using a ^{60}Co calibration source. ^{60}Co is a well-known calibration source for γ -ray detectors because it features two strong γ -rays at 1137 keV and 1332 keV. This calibration source was placed approximately 25 cm from each detector window. Each detector gathered data for approximately 15 minutes and accumulated a total of $\sim 10,000$ counts in the spectrum.

Figure 6.22 shows the raw spectra for each detector. In both spectra, the ^{60}Co 1172 keV and 1332 keV photopeaks are well-resolved and identifiable. There is also a peak at 1460 keV visible that was identified to be radioactive ^{40}K which is present in small amounts

⁵The S/N of each detector is labelled on the preamplifiers and the detector dewars

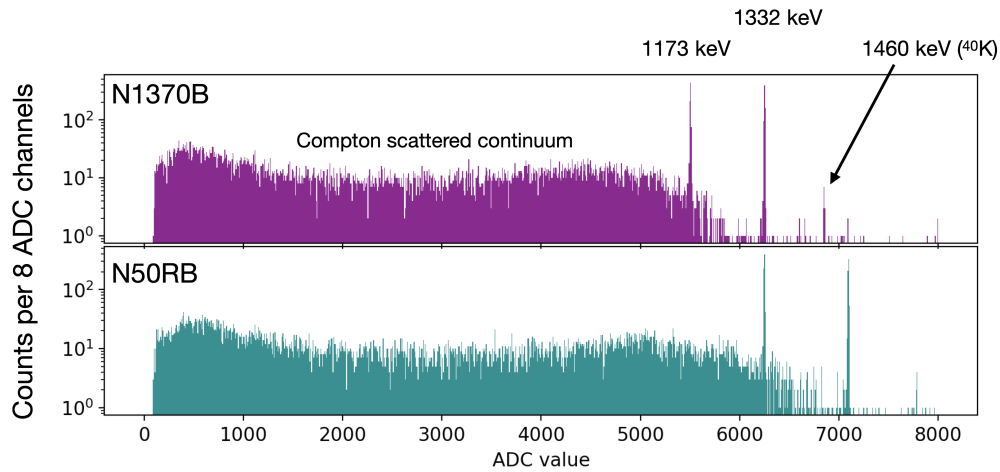


Figure 6.22: Two separate calibration spectra are shown recorded with two different γ -ray detectors using the same ^{60}Co calibration source.

in concrete⁶. We also see a strong continuum which is due to Compton scattering of the photons out of the detector volume such that they only deposit a fraction of their energy [155].

Most notable in this figure is the shift in where these photopeaks arrive on the ADC value for each detector. The most likely explanation for this is a difference in the charge carrier mobilities in each detector [155]. To match the photopeaks in each spectrum, small changes to the bias voltage of each detector can be performed until they are coarsely aligned. While we have not performed this operation yet, we have confirmed that the neighboring GRIFFIN spectrometer performs this operation on their HPGe detectors before they run an experiment. Therefore in the future, it would be good for TITAN to follow a procedure with each γ -ray detector to make sure the photopeaks of a given calibration spectrum are coarsely aligned before a RIB experiment. Fine adjustments would occur later during post-

⁶The neighboring GRIFFIN spectrometer verified that they also regularly observe this photopeak during calibrations.

	Resolution [keV FWHM]	
	@1173	@1332
Ortec [224]	–	≤ 2.0
25-N50RB	1.95(0.03)	2.03(0.05)
25-N50RB (on EBIT)	3.33(0.07)	3.70(0.08)
25-N1370B	2.22(0.04)	2.42(0.05)

Table 6.1: The photopeak resolution of detectors N50RB and N1370B at the two ^{60}Co photopeak energies measured with the detectors in a test stand. When installed on the EBIT, the resolution degrades due to vibrations. Uncertainties are shown as one standard deviation in parentheses.

experiment calibration of the data.

Table 6.1 shows the resolution of each detector at the ^{60}Co photopeaks in comparison to what is stated in the manual by Ortec. The photopeaks were fit using least-squares minimization of a Gaussian distribution with the lmfit Python package. 25-N50RB performs marginally better than 25-N1370Rb. This is likely due to a difference in the vacuum of each detector cryostat which needs to be refreshed every ~ 6 months. TITAN has a setup for performing vacuum refreshing on these detectors and the procedure is documented on our wiki⁷.

We also studied the vibration-induced noise in the ^{60}Co spectrum by mounting detector 25-N50RB onto the EBIT using the mechanism explained in Section 6.5.3. The EBIT does not currently provide a method for placing a calibration source in the trap center. Therefore, for detectors that are mounted onto one of the EBIT viewports, the opposite viewport should be unobstructed so that the calibration source can be installed there. In this case, the opposite viewport on the EBIT was not available for a calibration source, so we placed the calibration source near the detector cryostat. Note that this is not optimal because the

⁷<https://titan.wiki.triumf.ca>

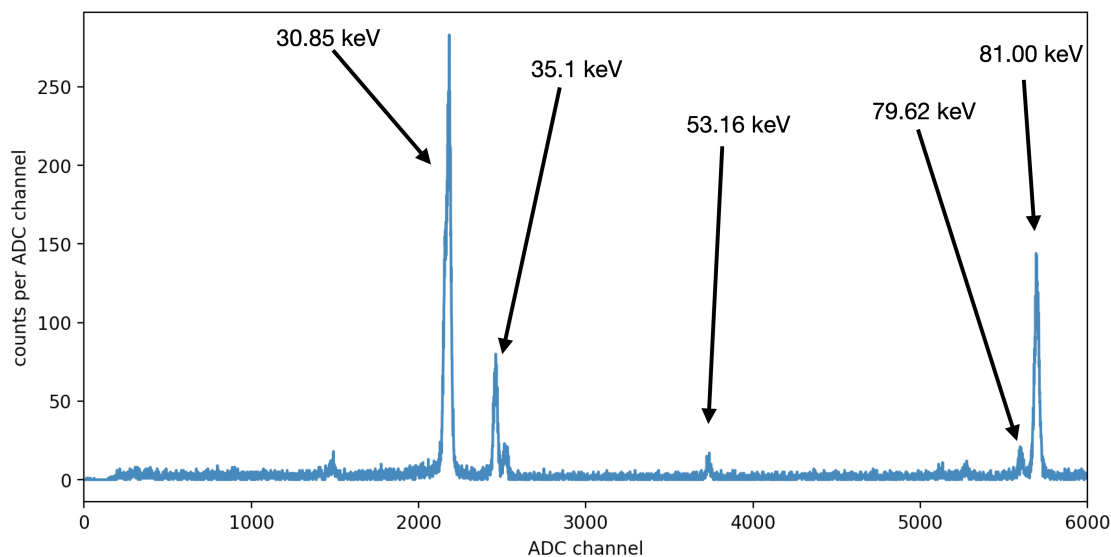


Figure 6.23: A calibration spectrum of ^{133}Ba using the X-ray detector.

geometry between the source and HPGe crystal is changed, but it does give an idea of the performance. The resulting resolution is also listed in Table 6.1.

X-ray detectors

A calibration spectrum with the X-ray detector was taken while it was mounted onto the EBIT. In this case, the opposite viewport was available for the calibration source to be mounted. The manual provided by Canberra specifies the resolution at two photopeak energies of the calibration sources, ^{57}Co (122 keV) and ^{55}Fe (5.9 keV). However, as neither of these calibration sources were available at TRIUMF at the time, a ^{133}Ba calibration source was used instead. The photopeak histogram is shown in Figure 6.23, where the dominant photopeaks are labelled. While we cannot make direct comparisons, the detector resolution falls reasonably within the specifications given by Canberra.

	Resolution [keV FWHM]						
	@5.9	@30.85	@35.81	@53.16	@79.62	@81	@122
Canberra Spec sheet	0.123						0.522
GUL0110P		0.59(0.01)	0.35(0.01)	0.38(0.01)	0.44(0.01)	0.46(0.01)	

Table 6.2: The photopeak resolution of our GUL0110P determined with a ^{133}Ba calibration source. Uncertainties are shown as one standard deviation in parentheses.

6.6.2 Ambient background in the EBIT

With the EBIT electron beam turned on and no ions or gas being injected, we used the X-ray detector to take a ~ 24 hour background spectrum. A 2D histogram of the background spectrum is shown in Figure 6.24. During the acquisition of the spectrum, the LN2 fill sequence ran two times, which are highlighted by the red lines. This plot suggests that vibrations from the LN2 fill sequence do not significantly contribute to noise in the spectrum. Also shown in the spectrum are two points where an increase in the 511 keV annihilation peak was observed. During the time that this background spectrum was recorded, the MR-ToF-MS was taking radioactive beam for an experiment. The increase in the 511 keV annihilation peak coincided with timestamps when MR-ToF-MS was receiving isotopes on the proton-rich side of stability.

6.6.3 Studying the space charge of the electron beam

This final section presents the preliminary results of an ongoing test using the X-ray detector to characterize the space charge effects of the electron beam. This is not only necessary to better understand charge breeding dynamics within the EBIT, but also to better predict experimental outcomes for decay spectroscopy experiments with the EBIT.

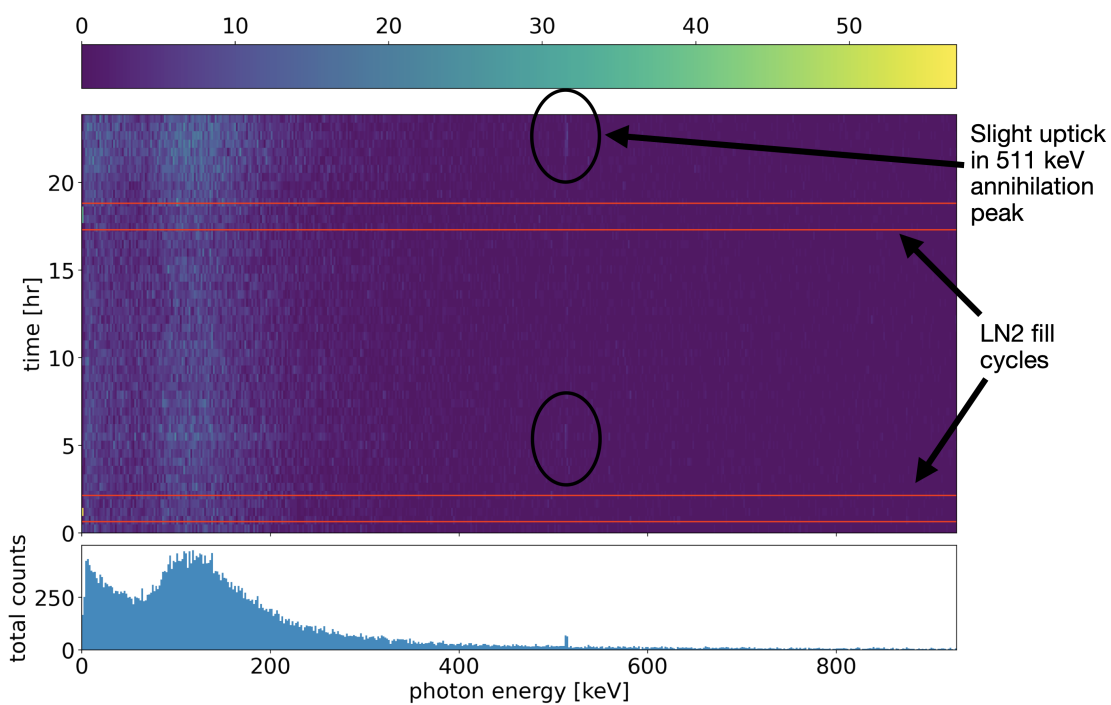


Figure 6.24: A 2D histogram of a 24 hour background spectrum recorded with the X-ray detector.

To first order, the EBIT electron beam energy is determined by the difference in electric potential between the cathode and the central drift tube. However, the presence of the electron beam itself will actually affect the beam energy. This is called a space charge effect and can shift the beam energy by as much as ~ 300 eV depending on beam current and energy. From here on I will refer to an electron beam energy that is “uncorrected” for space charge effects, and one that is “corrected”. One way to study the space charge effect in EBIT and EBIS devices is to use the electron-ion interaction called dielectronic recombination (DR) [225]. During DR, a free electron from the continuum is captured into a bound atomic state. The energy released is used to excite a bound electron to a higher level, which subsequently decays and releases an X-ray. Because the sum of the continuum electron energy and the bound state energy must equal the excitation energy of the promoted electron, this is a resonant process.

The notation used for DR is KLN, where a free electron is captured into the N shell, and the other electron is excited from the K to the L shell. Figure 6.25 schematically illustrates a KLL DR process. The uniqueness of DR is that it is a resonant process and in the reference frame of the bound electron, DR will only occur if the continuum electron matches the resonance energy. Using this fact, we can use DR lines as a probe to determine the correct electron beam energy in the EBIT.

In this experiment, we injected low pressure argon gas into the ion trap using the gas injection system mentioned in Section 6.3.2. Using a 50 mA electron beam, a 250 V trap was defined in the EBIT using the drift tubes to allow for the collection and charge breeding of the argon gas. The argon gas was accumulated for 19 seconds and then the trap was inverted to remove the HCI for 1 second. Simultaneously, we scanned the energy of the electron beam by changing the potential of the central and trap drift tubes with respect to the potential of

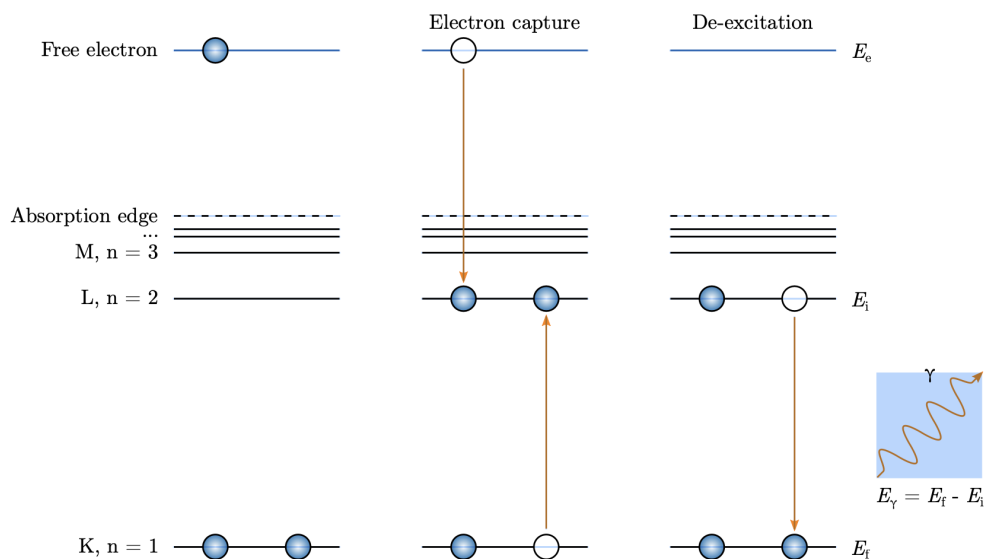


Figure 6.25: A schematic of KLL dielectronic recombination. The free electron is captured into the L shell, promoting an electron from the K shell into the L shell. The excited electron subsequently decays to the ground state through the emission of a photon. Figure from [225].

the cathode. The energy range of the scan was from 2125 eV to 2825 eV. Figure 6.26 shows a 2D histogram of the X-ray energy against the uncorrected energy of the electron beam. DR into the 16^+ and 15^+ charge states is strongly visible while DR into the 14^+ and 13^+ charge states is less visible. The uncorrected electron beam energy where these DR lines show up is a function of how much the ion cloud has compensated the space charge of the electron beam.

Figure 6.27 is a 2D histogram showing the time dependence of the argon KLL DR lines as the trap fills up. On the x-axis is the uncorrected energy range that the electron beam is scanned over and on the y-axis is the time after after the trap has been closed at $t = 0$. During the first ~ 7 seconds of ion accumulation in the trap, the DR lines show a tailing effect which is due to the positive ions compensating for the electron beam space charge. The DR lines eventually reach a steady-state line which is when the compensation between the

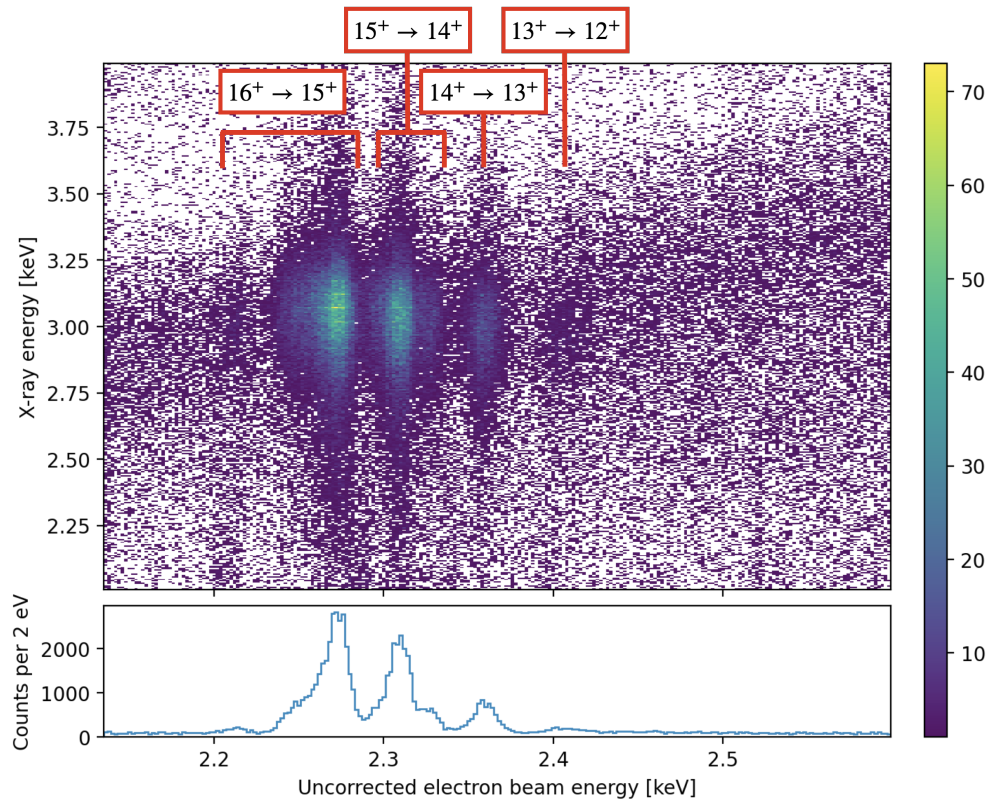


Figure 6.26: The top panel shows A 2D spectrum of KLL dielectronic recombination into highly-charged argon ions stored in the EBIT. The strongest transitions are recombination into the 16^+ and 15^+ charge states. The bottom panel shows a 1D histogram with counts summed between X-ray energies ranging from 2.75 keV to 3.25 keV.

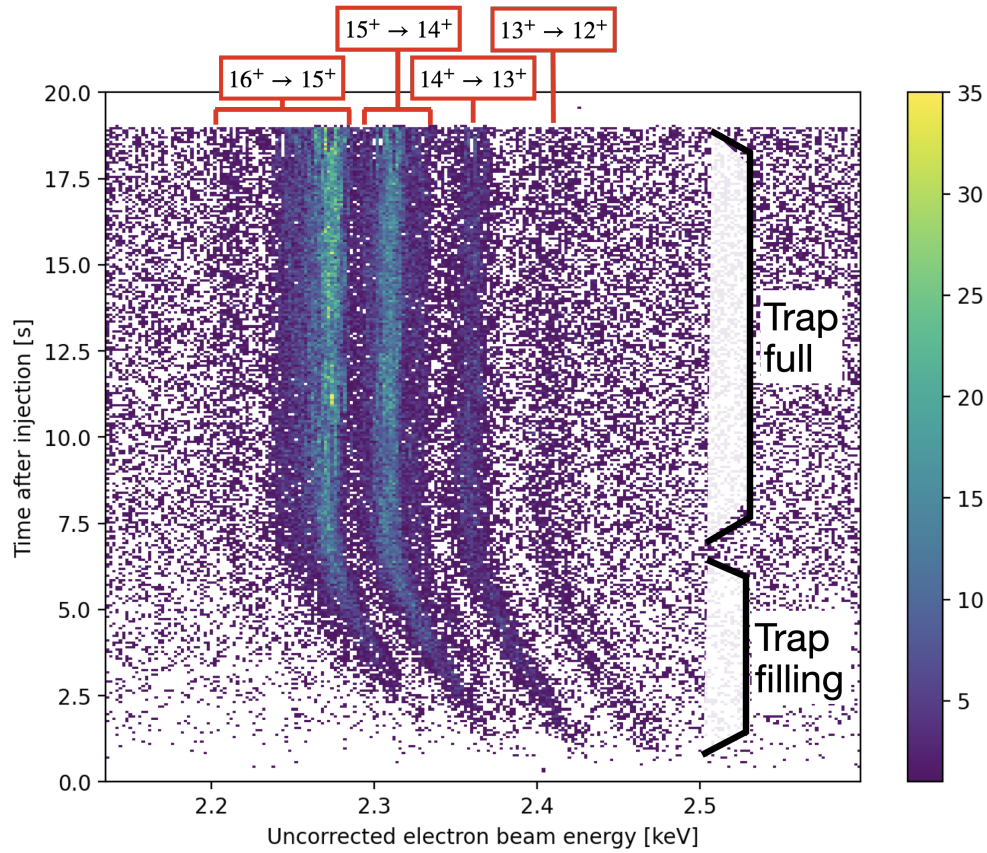


Figure 6.27: A plot showing the time dependence of argon KLL DR lines as the trap is filled up. As the positively charged argon fills the trap, it compensates the electron beam space charge. The resonant DR lines shift as the continuum electron energy shifts until a steady state is reached after ~ 7 seconds.

ion cloud and the electron beam has stopped, i.e. when the trap is full. If we extrapolate the tails to $t = 0$, we can determine at what uncorrected beam energy the DR line would be if the electron beam were completely uncompensated by the ion cloud (i.e. when no ions are in the trap). For KLL DR into Ar^{14+} this is roughly 2440 eV. Multi-Configuration Dirac-Fock (MCDF) calculations of Ar^{14+} predict that the KLL DR resonance energy is 2303 eV [225], therefore the difference of 137 eV must account for the space charge of the electron beam. MCDF calculations have been shown to estimate these DR resonance strengths with an accuracy to within a few percent [226]. These results are still preliminary and the TITAN team is working to refine them and investigate if DR lines can be used to determine the space charge corrected electron beam energy during radioactive HCI decay spectroscopy experiments.

Chapter 7

Conclusion

Some of the most intriguing questions in contemporary nuclear physics arise at the boundaries of nuclear stability. These questions pertain not only to our understanding of fundamental physics and the structure of exotic nuclei, but also far away astrophysical phenomena such as X-ray bursts. Our ability to answer these questions requires a strong interdisciplinary and collaborative effort between scientists around the world. Experimental efforts to study these nuclei rely on both terrestrial-based experiments to produce and study radioactive nuclei as well as space-based experiments to observe them in their naturally-produced habitat. Radioactive ion beam facilities continue to expand the boundaries of radioactive nuclei production, allowing unprecedented access to rare and short-lived nuclei for specialized experimental setups [199]. Astronomers continue to develop new space-based telescope observatories which provide astronomical data with unprecedented resolution [28, 30, 188]. At the same time, theoretical physicists are leveraging new breakthroughs in computing power to provide increasingly complex models which allow us to interpret these experimental observations in terms of their underlying nuclear structure and mechanisms. In this thesis we presented two physics motivations which require the study of these rare and short-lived nuclei that exist near the proton drip line.

The first of these utilizes the simplicity of the isospin framework to study nuclear structure near $N = Z$ via the Isobaric Multiplet Mass Equation (IMME) [15, 49, 63]. The extraction of IMME coefficients using available data on atomic mass and nuclear level structure provides a convenient way to study the differences that proton and neutron content in the nucleus have on nuclear structure. However, in most cases this requires detailed nuclear level structure that is not always available for rare short-lived isotopes. Mass measurements in these difficult-to-reach regions of the nuclear chart can provide a first foray into extending the IMME

coefficients into higher masses to study nuclear structure.

The second motivation pertains to the astrophysical rp-process which climbs the neutron-deficient side of stability with a sequence of fast proton captures and slow β -decays. Due to the difficulty of obtaining empirical reaction rate data for this process, an important input for theoretical models is the atomic masses of the nuclei involved in the rp-process. However, because of the difficulty of measuring the atomic masses of short-lived isotopes near the proton drip line, many of the nuclei involved in the rp-process are not measured to the required ~ 10 keV precision [42, 112]. Due to the involvement of the rp-process in thermonuclear X-ray bursts, constraining the rp-process reaction flow path is important for determining the underlying properties of the neutron star [34], the accretion and burst mechanism [33], and possibly nucleosynthesis [14].

To address these physics motivations, this thesis presented mass measurements of $^{74-76}\text{Sr}$ at the TRIUMF RIB ISOL laboratory using the TITAN MR-ToF-MS [46]. Additional mass measurements of ^{145}Tb , ^{146}Tb , and ^{148}Ho were presented. This highlights the unique benefits of using MR-ToF-MS at a RIB ISOL facility to achieve high resolving powers while maintaining fast measurement cycles and a high efficiency for small signal-to-background ratios.

The new measurements of $^{74-75}\text{Sr}$ provide the mass data required to complete the $T = 1$ triplet at $A = 74$ and the $T = 1/2$ doublet at $A = 75$. When combined with a recent measurement of ^{71}Kr [159], the new doublet b coefficients resolve a staggering anomaly that was first mentioned by Kaneko *et al.* in 2014 [74] and later studied by Tu *et al.* [77]. The newly completed triplet at $A = 74$ is now the heaviest triplet that has been measured by 8 mass units. The triplet b and c coefficients were compared with a homogeneously charged sphere model from MacCormick *et al.* [49] and a VS-IMSRG calculation by Martin *et al.*

[178]. The triplet b and c coefficients demonstrated good agreement with the homogeneously charged sphere model and reasonably good agreement with the VS-IMSRG calculations. The utility of these coefficients for theoretical extraction of isospin symmetry breaking corrections was highlighted because these corrections are a central focus of tests to constrain top-row unitarity of the CKM matrix [51–53].

A single-zone X-ray burst simulation was performed using the new strontium mass data to investigate its effect on rp-process flow path and burst ashes. The new masses help to better pin down the reaction flow path between the ^{72}Kr and ^{76}Sr waiting points. This results in increased production of stable $A = 74$ ashes due to an increased strength of the ^{74}Rb β -decay branch and a decrease in the amount of mass flow beyond the ^{76}Sr waiting point. Along with previous studies by Hoff *et al.* [182] and Rodriguez *et al.* [115], this helps to solidify ^{72}Kr as a waiting point nucleus.

A hand full of nuclear decays proceed through an interaction with the atomic orbital. The effect of the ionic charge state on these radioactive decays has been shown to modify decay half-lives by orders of magnitude and in some cases completely block the decay channel [192, 193, 195, 227]. This effect is highly relevant in astrophysical environments which are hot enough to fully ionize an atom [194]. However, terrestrial experiments to study the nuclear decays of radioactive highly-charged ions are difficult to perform because of the high degree of technical expertise required for producing radioactive beams, highly charged ions, and performing decay spectroscopy. The second topic of this thesis work covered the installation and commissioning of a HPGe detector array at the TITAN EBIT for decay spectroscopy of radioactive highly charged ions. The work that was undertaken to install this array involved testing and mounting the detectors, setting up a liquid nitrogen auto-filling system, and configuration of the electronics and software required to

maintain and operate the array. The first operation of these detectors on the EBIT was demonstrated with tests of the detector resolution, the ambient background in the EBIT and an estimation of the electron beam space charge using dielectronic recombination in highly charged argon. Two RIB proposals to observe Nuclear Excitation via Electron Capture (S2128) and Nuclear Two-photon Emission (S2175) in the TITAN EBIT were submitted to TRIUMF's Experiment Evaluation Committee and approved with high priority. The presented experimental work was a step towards demonstrating readiness of TITAN's EBIT and the in-trap decay spectroscopy setup to perform these measurements.

A new generation of RIB facilities including ARIEL at TRIUMF, FRIB at Michigan State University, and FAIR at GSI will soon be pushing the boundaries of RIB production even further than is currently achievable. The unique experimental techniques demonstrated in this thesis will be invaluable tools to help us refine our understanding of nuclear structure, astrophysics, and fundamental physics.

Bibliography

- [1] G. J. Maclay, “History and some aspects of the Lamb shift,” *Physics*, vol. 2, no. 2, pp. 105–149, 2020.
- [2] R. H. Parker, C. Yu, W. Zhong, B. Estey, and H. Müller, “Measurement of the fine-structure constant as a test of The Standard Model,” *Science*, vol. 360, no. 6385, pp. 191–195, 2018.
- [3] S. Sturm, F. Köhler, J. Zatorski, A. Wagner, Z. Harman, G. Werth, W. Quint, C. H. Keitel, and K. Blaum, “High-precision measurement of the atomic mass of the electron,” *Nature*, vol. 506, no. 7489, pp. 467–470, 2014.
- [4] E. Rutherford, “LXXIX. The scattering of α and β particles by matter and the structure of the atom,” *The London, Edinburgh, and Dublin Philosophical Magazine and Journal of Science*, vol. 21, no. 125, pp. 669–688, 1911.
- [5] H. Yukawa, “On the interaction of elementary particles. I,” *Proceedings of the Physico-Mathematical Society of Japan. 3rd Series*, vol. 17, pp. 48–57, 1935.
- [6] W. Weise, “Yukawa’s pion, low-energy QCD and nuclear chiral dynamics,” *Progress of Theoretical Physics Supplement*, vol. 170, pp. 161–184, 2007.

- [7] E. D. Bloom, D. H. Coward, H. DeStaebler, J. Drees, G. Miller, L. W. Mo, R. E. Taylor, M. Breidenbach, J. I. Friedman, G. C. Hartmann, and H. W. Kendall, “High-energy inelastic $e - p$ scattering at 6° and 10° ,” *Physical Review Letters*, vol. 23, pp. 930–934, Oct 1969.
- [8] S. Bethke, “Experimental tests of asymptotic freedom,” *Progress in particle and Nuclear Physics*, vol. 58, no. 2, pp. 351–386, 2007.
- [9] R. Machleidt and D. R. Entem, “Chiral effective field theory and nuclear forces,” *Physics Reports*, vol. 503, no. 1, pp. 1–75, 2011.
- [10] O. Kofoed-Hansen and K. Nielsen, “Short-lived krypton isotopes and their daughter substances,” *Physical Review*, vol. 82, no. 1, p. 96, 1951.
- [11] E. Kugler, “The ISOLDE facility,” *Hyperfine interactions*, vol. 129, no. 1-4, pp. 23–42, 2000.
- [12] I. Tanihata, “Radioactive beam science, past, present and future,” *Nuclear Instruments and Methods in Physics Research Section B: Beam Interactions with Materials and Atoms*, vol. 266, no. 19-20, pp. 4067–4073, 2008.
- [13] Y. Blumenfeld, T. Nilsson, and P. V. Duppen, “Facilities and methods for radioactive ion beam production,” *Physica Scripta*, vol. T152, p. 014023, jan 2013.
- [14] H. Schatz, A. Aprahamian, J. Görres, M. Wiescher, T. Rauscher, J. Rembges, F.-K. Thielemann, B. Pfeiffer, P. Möller, K.-L. Kratz, *et al.*, “rp-process nucleosynthesis at extreme temperature and density conditions,” *Physics Reports*, vol. 294, no. 4, pp. 167–263, 1998.

- [15] M. Bentley and S. Lenzi, “Coulomb energy differences between high-spin states in isobaric multiplets,” *Progress in Particle and Nuclear Physics*, vol. 59, no. 2, pp. 497–561, 2007.
- [16] M. Thoennessen, “Reaching the limits of nuclear stability,” *Reports on Progress in Physics*, vol. 67, no. 7, p. 1187, 2004.
- [17] K. Blaum, J. Dilling, and W. Nörtershäuser, “Precision atomic physics techniques for nuclear physics with radioactive beams,” *Physica Scripta*, vol. T152, p. 014017, jan 2013.
- [18] W. Heisenberg, “Über den Bau der Atomkerne. I,” *Zeitschrift für Physik*, vol. 77, no. 1, pp. 1–11, 1932.
- [19] J. Nolen Jr and J. Schiffer, “Coulomb energies,” *Annual Review of Nuclear Science*, vol. 19, no. 1, pp. 471–526, 1969.
- [20] N. Auerbach, V. Bernard, and N. Van Giai, “ ^{41}Sc - ^{41}Ca Coulomb displacement energy,” *Physical Review C*, vol. 21, pp. 744–751, Feb 1980.
- [21] N. Auerbach, V. Bernard, and N. Van Giai, “Coulomb displacement energies in nuclei: A new approach,” *Nuclear Physics A*, vol. 337, no. 1, pp. 143–156, 1980.
- [22] N. Auerbach, “Coulomb effects in nuclear structure,” *Physics Reports*, vol. 98, no. 5, pp. 273–341, 1983.
- [23] W. Ormand and B. Brown, “Empirical isospin-nonconserving hamiltonians for shell-model calculations,” *Nuclear Physics A*, vol. 491, no. 1, pp. 1–23, 1989.

- [24] Y. H. Lam, N. A. Smirnova, and E. Caurier, “Isospin nonconservation in *sd*-shell nuclei,” *Physical Review C*, vol. 87, p. 054304, May 2013.
- [25] R. Wallace and S. E. Woosley, “Explosive hydrogen burning,” *The Astrophysical Journal Supplement Series*, vol. 45, pp. 389–420, 1981.
- [26] D. K. Galloway and L. Keek, “Thermonuclear X-ray bursts,” in *Timing Neutron Stars: Pulsations, Oscillations and Explosions*, pp. 209–262, Springer, 2021.
- [27] Jean in ’t Zand, “List of 118 Galactic Type-I X-ray bursters.” <https://personal.sron.nl/~jeanz/bursterlist.html>, 2022. Accessed: 2022-10-18.
- [28] F. A. Harrison, W. W. Craig, F. E. Christensen, C. J. Hailey, W. W. Zhang, S. E. Boggs, D. Stern, W. R. Cook, K. Forster, P. Giommi, *et al.*, “The nuclear spectroscopic telescope array (NuSTAR) high-energy X-ray mission,” *The Astrophysical Journal*, vol. 770, no. 2, p. 103, 2013.
- [29] K. C. Gendreau, Z. Arzoumanian, and T. Okajima, “The Neutron star Interior Composition ExploreR (NICER): an explorer mission of opportunity for soft X-ray timing spectroscopy,” in *Space Telescopes and Instrumentation 2012: Ultraviolet to Gamma Ray*, vol. 8443, pp. 322–329, SPIE, 2012.
- [30] P. Agrawal, “AstroSat: From inception to realization and launch,” *Journal of Astrophysics and Astronomy*, vol. 38, pp. 1–8, 2017.
- [31] N. N. Weinberg, L. Bildsten, and H. Schatz, “Exposing the nuclear burning ashes of radius expansion type I X-ray bursts,” *The Astrophysical Journal*, vol. 639, no. 2, p. 1018, 2006.

- [32] T. Rauscher, N. Dauphas, I. Dillmann, C. Fröhlich, Z. Fülöp, and G. Gyürky, “Constraining the astrophysical origin of the p-nuclei through nuclear physics and meteoritic data,” *Reports on Progress in Physics*, vol. 76, no. 6, p. 066201, 2013.
- [33] Z. Meisel, “Consistent modeling of GS 1826-24 X-ray bursts for multiple accretion rates demonstrates the possibility of constraining rp-process reaction rates,” *The Astrophysical Journal*, vol. 860, no. 2, p. 147, 2018.
- [34] Z. Meisel, A. Deibel, L. Keek, P. Shternin, and J. Elfritz, “Nuclear physics of the outer layers of accreting neutron stars,” *Journal of Physics G: Nuclear and Particle Physics*, vol. 45, no. 9, p. 093001, 2018.
- [35] R. Lau, M. Beard, S. S. Gupta, H. Schatz, A. Afanasjev, E. F. Brown, A. Deibel, L. R. Gasques, G. W. Hitt, W. R. Hix, *et al.*, “Nuclear reactions in the crusts of accreting neutron stars,” *The Astrophysical Journal*, vol. 859, no. 1, p. 62, 2018.
- [36] A. Parikh, J. José, G. Sala, and C. Iliadis, “Nucleosynthesis in type I X-ray bursts,” *Progress in Particle and Nuclear Physics*, vol. 69, pp. 225–253, 2013.
- [37] H. Schatz, A. Aprahamian, V. Barnard, L. Bildsten, A. Cumming, M. Ouellette, T. Rauscher, F.-K. Thielemann, and M. Wiescher, “End point of the *rp* process on accreting neutron stars,” *Physical Review Letters*, vol. 86, pp. 3471–3474, Apr 2001.
- [38] O. Koike, M. Hashimoto, K. Arai, and S. Wanajo, “Rapid proton capture on accreting neutron stars-effects of uncertainty in the nuclear process,” *Astronomy and Astrophysics, v. 342, p. 464-473 (1999)*, vol. 342, pp. 464–473, 1999.

- [39] B. A. Brown, R. R. C. Clement, H. Schatz, A. Volya, and W. A. Richter, “Proton drip-line calculations and the rp process,” *Physical Review C*, vol. 65, p. 045802, Mar 2002.
- [40] R. Cyburt, A. Amthor, A. Heger, E. Johnson, L. Keek, Z. Meisel, H. Schatz, and K. Smith, “Dependence of X-ray burst models on nuclear reaction rates,” *The Astrophysical Journal*, vol. 830, no. 2, p. 55, 2016.
- [41] H. Schatz and W.-J. Ong, “Dependence of X-ray burst models on nuclear masses,” *The Astrophysical Journal*, vol. 844, p. 139, aug 2017.
- [42] N. N. Duy, P.-T. Ho, and N. K. Uyen, “Examination of the astrophysical-rate variations of the key reactions in the rp-process due to mass uncertainties,” *Journal of the Korean Physical Society*, vol. 76, no. 10, pp. 881–888, 2020.
- [43] A. Parikh, J. José, F. Moreno, and C. Iliadis, “The effects of variations in nuclear processes on type I X-ray burst nucleosynthesis,” *The Astrophysical Journal Supplement Series*, vol. 178, no. 1, p. 110, 2008.
- [44] A. A. Kwiatkowski, C. Andreoiu, J. C. Bale, T. Brunner, A. Chaudhuri, U. Chowdhury, P. Delheij, S. Ettenauer, D. Frekers, A. T. Gallant, A. Grossheim, G. Gwinner, F. Jang, A. Lennarz, T. Ma, E. Mané, M. R. Pearson, B. E. Schultz, M. C. Simon, V. V. Simon, and J. Dilling, “TITAN: An ion trap facility for on-line mass measurement experiments,” *Hyperfine Interactions*, vol. 225, pp. 143–153, oct 2014.
- [45] D. Lascar, A. Kwiatkowski, M. Alanssari, U. Chowdhury, J. Even, A. Finlay, A. Gallant, M. Good, R. Klawitter, B. Kootte, T. Li, K. Leach, A. Lennarz, E. Leistenschneider, A. Mayer, B. Schultz, R. Schupp, D. Short, C. Andreoiu,

- J. Dilling, and G. Gwinner, “Improvements to TITAN’s mass measurement and decay spectroscopy capabilities,” *Nuclear Instruments and Methods in Physics Research Section B: Beam Interactions with Materials and Atoms*, vol. 376, pp. 292–297, 2016. Proceedings of the XVIIth International Conference on Electromagnetic Isotope Separators and Related Topics (EMIS2015), Grand Rapids, MI, U.S.A., 11-15 May 2015.
- [46] C. Jesch, T. Dickel, and W. R. Plasß, “The MR-ToF-MS isobar separator for the TITAN facility at TRIUMF,” *Hyperfine Interactions*, vol. 235, pp. 97–106, 2015.
- [47] M. Reiter, S. A. S. Andrés, J. Bergmann, T. Dickel, J. Dilling, A. Jacobs, A. Kwiatkowski, W. Plaß, C. Scheidenberger, D. Short, C. Will, C. Babcock, E. Dunling, A. Finlay, C. Hornung, C. Jesch, R. Klawitter, B. Kootte, D. Lascar, E. Leistenschneider, T. Murböck, S. Paul, and M. Yavor, “Commissioning and performance of TITAN’s Multiple-Reflection Time-of-Flight Mass-Spectrometer and isobar separator,” *Nuclear Instruments and Methods in Physics Research Section A: Accelerators, Spectrometers, Detectors and Associated Equipment*, vol. 1018, p. 165823, 2021.
- [48] E. Tiesinga, P. Mohr, D. Newell, and B. Taylor, “CODATA Recommended Values of the Fundamental Physical Constants: 2018,” 2021-06-30 04:06:00 2021.
- [49] M. MacCormick and G. Audi, “Evaluated experimental isobaric analogue states from $T = 1/2$ to $T = 3$ and associated IMME coefficients,” *Nuclear Physics A*, vol. 925, pp. 61–95, 2014.

- [50] M. Chadwick, P. Obložinský, M. Herman, *et al.*, “ENDF/B-VII.0: Next generation evaluated nuclear data library for nuclear science and technology,” *Nuclear Data Sheets*, vol. 107, pp. 2931–3118, December 2006.
- [51] J. C. Hardy and I. S. Towner, “Superaligned $0^+ \rightarrow 0^+$ nuclear β decays: 2020 critical survey, with implications for V_{ud} and CKM unitarity,” *Physical Review C*, vol. 102, p. 045501, Oct 2020.
- [52] I. S. Towner and J. C. Hardy, “Comparative tests of isospin-symmetry-breaking corrections to superallowed $0^+ \rightarrow 0^+$ nuclear β decay,” *Physical Review C*, vol. 82, p. 065501, Dec 2010.
- [53] I. S. Towner and J. C. Hardy, “Improved calculation of the isospin-symmetry-breaking corrections to superallowed Fermi β decay,” *Physical Review C*, vol. 77, p. 025501, Feb 2008.
- [54] C.-Y. Seng, M. Gorchtein, H. H. Patel, and M. J. Ramsey-Musolf, “Reduced Hadronic Uncertainty in the Determination of V_{ud} ,” *Physical Review Letters*, vol. 121, p. 241804, Dec 2018.
- [55] C.-Y. Seng, M. Gorchtein, and M. J. Ramsey-Musolf, “Dispersive evaluation of the inner radiative correction in neutron and nuclear β decay,” *Physical Review D*, vol. 100, p. 013001, Jul 2019.
- [56] A. Czarnecki, W. J. Marciano, and A. Sirlin, “Radiative corrections to neutron and nuclear beta decays revisited,” *Physical Review D*, vol. 100, p. 073008, Oct 2019.

- [57] B. Blank and M. Borge, “Nuclear structure at the proton drip line: Advances with nuclear decay studies,” *Progress in Particle and Nuclear Physics*, vol. 60, no. 2, pp. 403–483, 2008.
- [58] W.-J. Ong, C. Langer, F. Montes, A. Aprahamian, D. W. Bardayan, D. Bazin, B. A. Brown, J. Browne, H. Crawford, R. Cyburt, E. B. Deleeuw, C. Domingo-Pardo, A. Gade, S. George, *et al.*, “Low-lying level structure of ^{56}Cu and its implications for the *rp* process,” *Physical Review C*, vol. 95, p. 055806, May 2017.
- [59] M. Saxena, W.-J. Ong, Z. Meisel, D. Hoff, N. Smirnova, P. Bender, S. Burcher, M. Carpenter, J. Carroll, A. Chester, *et al.*, “ ^{57}Zn β -delayed proton emission establishes the ^{56}Ni *rp*-process waiting point bypass,” *Physics Letters B*, vol. 829, p. 137059, 2022.
- [60] O. Klochko and N. A. Smirnova, “Isobaric-multiplet mass equation in a macroscopic-microscopic approach,” *Physical Review C*, vol. 103, p. 024316, Feb 2021.
- [61] J. J. Sakurai, *Modern quantum mechanics; rev. ed.* Reading, MA: Addison-Wesley, 1994.
- [62] B. Brown and R. Sherr, “Charge-dependent two-body interactions deduced from displacement energies in the $1f_{7/2}$ shell,” *Nuclear Physics A*, vol. 322, no. 1, pp. 61–91, 1979.
- [63] Y. H. Lam, B. Blank, N. A. Smirnova, J. B. Bueb, and M. S. Antony, “The isobaric multiplet mass equation for $A \leq 71$ revisited,” *Atomic Data and Nuclear Data Tables*, vol. 99, no. 6, pp. 680–703, 2013.
- [64] M. Kamil, S. Triambak, A. Magilligan, A. García, B. Brown, P. Adsley, V. Bildstein, C. Burbadge, A. D. Varela, T. Faestermann, *et al.*, “Isospin mixing and the cubic

- isobaric multiplet mass equation in the lowest $T = 2$, $A = 32$ quintet,” *Physical Review C*, vol. 104, no. 6, p. L061303, 2021.
- [65] H. A. Bethe and R. F. Bacher, “Nuclear physics A. Stationary states of nuclei,” *Reviews of Modern Physics*, vol. 8, no. 2, p. 82, 1936.
- [66] B. C. Carlson and I. Talmi, “Pairing Effects in Coulomb Energies and the Radii of Mirror Nuclei,” *Physical Review*, vol. 96, pp. 436–444, Oct 1954.
- [67] S. Sengupta, “Coulomb energies of mirror nuclei,” *Nuclear Physics*, vol. 21, pp. 542–554, 1960.
- [68] J. Henderson, D. Jenkins, K. Kaneko, P. Ruotsalainen, P. Sarriguren, K. Auranen, M. Bentley, P. Davies, A. Gorgen, T. Grahn, *et al.*, “Spectroscopy on the proton drip-line: Probing the structure dependence of isospin nonconserving interactions,” *Physical Review C*, vol. 90, no. 5, p. 051303, 2014.
- [69] W. Huang, M. Wang, F. G. Kondev, G. Audi, and S. Naimi, “The AME 2020 atomic mass evaluation (I). Evaluation of input data, and adjustment procedures,” *Chinese Physics C*, vol. 45, no. 3, p. 030002, 2021.
- [70] National Nuclear Data Center at Brookhaven National Laboratory, “Evaluated Nuclear Structure Data File.” <https://www.nndc.bnl.gov/ensdf/>, 2023. Accessed: August 2023.
- [71] E. Feenberg and G. Goertzel, “Theory of Nuclear Coulomb Energy,” *Physical Review*, vol. 70, pp. 597–602, Nov 1946.
- [72] J. Janecke, “Vector and Tensor Coulomb Energies,” *Physical Review*, vol. 147, pp. 735–742, Jul 1966.

- [73] K. T. Hecht, “Simple shell-model expressions for Coulomb energies,” *Nuclear Physics A*, vol. 114, no. 2, pp. 280–288, 1968.
- [74] K. Kaneko, Y. Sun, T. Mizusaki, and S. Tazaki, “Variation in Displacement Energies Due to Isospin-Nonconserving Forces,” *Physical Review Letters*, vol. 110, p. 172505, Apr 2013.
- [75] P. Baczyk, J. Dobaczewski, M. Konieczka, W. Satuła, T. Nakatsukasa, and K. Sato, “Isospin-symmetry breaking in masses of $N \approx Z$ nuclei,” *Physics Letters B*, vol. 778, pp. 178–183, Jan 2018.
- [76] H. H. Li, Q. Yuan, J. G. Li, M. R. Xie, S. Zhang, Y. H. Zhang, X. X. Xu, N. Michel, F. R. Xu, and W. Zuo, “Investigation of isospin-symmetry breaking in mirror energy difference and nuclear mass with ab initio calculations,” *Physical Review C*, vol. 107, p. 014302, Jan 2023.
- [77] X. Tu, Y. Sun, Y. Zhang, H. Xu, K. Kaneko, Y. A. Litvinov, and M. Wang, “A survey of Coulomb displacement energies and questions on the anomalous behavior in the upper fp -shell,” *Journal of Physics G: Nuclear and Particle Physics*, vol. 41, no. 2, p. 025104, 2014.
- [78] D. G. Jenkins, “Waiting points in the astrophysical rp -process: How unbound are ^{69}Br and ^{73}Rb ?,” *Physical Review C*, vol. 78, p. 012801, Jul 2008.
- [79] A. M. Rogers, M. A. Famiano, W. G. Lynch, M. S. Wallace, F. Amorini, D. Bazin, R. J. Charity, F. Delaunay, R. T. de Souza, J. Elson, A. Gade, D. Galaviz, M.-J. van Goethem, S. Hudan, J. Lee, and more, “Ground-State Proton Decay of ^{69}Br and

- Implications for the ^{68}Se Astrophysical Rapid Proton-Capture Process Waiting Point,” *Physical Review Lett.*, vol. 106, p. 252503, Jun 2011.
- [80] D. E. M. Hoff, A. M. Rogers, Z. Meisel, P. C. Bender, K. Brandenburg, K. Childers, J. A. Clark, A. C. Dombos, E. R. Doucet, S. Jin, R. Lewis, S. N. Liddick, C. J. Lister, C. Morse, H. Schatz, K. Schmidt, D. Soltesz, S. K. Subedi, S. M. Wang, and S. Waniganeththi, “Influence of ^{73}Rb on the ashes of accreting neutron stars,” *Physical Review C*, vol. 102, p. 045810, Oct 2020.
- [81] D. Hoff, A. Rogers, S. Wang, P. Bender, K. Brandenburg, K. Childers, J. Clark, A. Dombos, E. Doucet, S. Jin, *et al.*, “Mirror-symmetry violation in bound nuclear ground states,” *Nature*, vol. 580, no. 7801, pp. 52–55, 2020.
- [82] N. Michel, W. Nazarewicz, and M. Płoszajczak, “Isospin mixing and the continuum coupling in weakly bound nuclei,” *Physical Review C*, vol. 82, no. 4, p. 044315, 2010.
- [83] R. G. Thomas, “An analysis of the energy levels of the mirror nuclei, C^{13} and N^{13} ,” *Phys. Rev.*, vol. 88, pp. 1109–1125, Dec 1952.
- [84] J. B. Ehrman, “On the Displacement of Corresponding Energy Levels of C^{13} and N^{13} ,” *Phys. Rev.*, vol. 81, pp. 412–416, Feb 1951.
- [85] E. Comay, I. Kelson, and A. Zidon, “The Thomas-Ehrman shift across the proton dripline,” *Physics Letters B*, vol. 210, no. 1-2, pp. 31–34, 1988.
- [86] A. Wapstra and G. Audi, “Present knowledge of atomic masses,” in *Exotic Nuclei and Atomic Masses: Proceedings of the Third International Conference on Exotic Nuclei and Atomic Masses ENAM 2001 Hämeenlinna, Finland, 2–7 July 2001*, pp. 3–7, Springer, 2003.

- [87] S. Paul, J. Bergmann, J. Cardona, K. Dietrich, E. Dunling, Z. Hockenbery, C. Hornung, C. Izzo, A. Jacobs, A. Javaji, *et al.*, “Mass measurements of Ga 60–63 reduce X-ray burst model uncertainties and extend the evaluated $T = 1$ isobaric multiplet mass equation,” *Physical Review C*, vol. 104, no. 6, p. 065803, 2021.
- [88] X. Zhou, M. Wang, Y. Zhang, Y. A. Litvinov, Z. Meisel, K. Blaum, X. Zhou, S. Hou, K. Li, H. Xu, *et al.*, “Mass measurements show slowdown of rapid proton capture process at waiting-point nucleus ^{64}Ge ,” *Nature Physics*, pp. 1–7, 2023.
- [89] P. Baczyk, W. Satuła, J. Dobaczewski, and M. Konieczka, “Isobaric multiplet mass equation within nuclear density functional theory,” *Journal of Physics G: Nuclear and Particle Physics*, vol. 46, no. 3, p. 03LT01, 2019.
- [90] C. Hansen and H. Van Horn, “Steady-state nuclear fusion in accreting neutron-star envelopes,” *Astrophysical Journal*, vol. 195, Feb. 1, 1975, pt. 1, p. 735–741., vol. 195, pp. 735–741, 1975.
- [91] M. Schwarzschild and R. Härm, “Thermal instability in non-degenerate stars.,” *Astrophysical Journal*, vol. 142, p. 855, vol. 142, p. 855, 1965.
- [92] S. W. Kieffer, “Blast dynamics at mount St. Helens on 18 May 1980,” *Nature*, vol. 291, no. 5816, pp. 568–570, 1981.
- [93] E. F. Brown and L. Bildsten, “The ocean and crust of a rapidly accreting neutron star: implications for magnetic field evolution and thermonuclear flashes,” *The Astrophysical Journal*, vol. 496, no. 2, p. 915, 1998.

- [94] R. Wijnands, M. Nowak, J. M. Miller, J. Homan, S. Wachter, and W. H. Lewin, “A Chandra observation of the neutron star X-ray transient and eclipsing binary MXB 1659–29 in quiescence,” *The Astrophysical Journal*, vol. 594, no. 2, p. 952, 2003.
- [95] P. Ubertini, A. Bazzano, M. Cocchi, L. Natalucci, J. Heise, J. Muller, *et al.*, “Bursts from GS 1826–238: A Clocked Thermonuclear Flashes Generator,” *The Astrophysical Journal*, vol. 514, no. 1, p. L27, 1999.
- [96] D. K. Galloway, A. J. Goodwin, and L. Keek, “Thermonuclear burst observations for model comparisons: a reference sample,” *Publications of the Astronomical Society of Australia*, vol. 34, p. e019, 2017.
- [97] A. Heger, A. Cumming, D. K. Galloway, and S. E. Woosley, “Models of type I X-ray bursts from GS 1826–24: A probe of rp-process hydrogen burning,” *The Astrophysical Journal*, vol. 671, no. 2, p. L141, 2007.
- [98] N. Gehrels, G. Chincarini, P. e. Giommi, K. Mason, J. Nousek, A. Wells, N. White, S. Barthelmy, D. Burrows, L. Cominsky, *et al.*, “The Swift gamma-ray burst mission,” *The Astrophysical Journal*, vol. 611, no. 2, p. 1005, 2004.
- [99] J. Grindlay and H. Gursky, “UHURU observations of the Norma X-ray burster,” *Astrophysical Journal*, vol. 209, Oct. 15, 1976, pt. 2, p. L61-L64., vol. 209, pp. L61–L64, 1976.
- [100] W. Evans, R. Belian, and J. Conner, “Observations of intense cosmic X-ray bursts,” *Astrophysical Journal*, vol. 207, July 15, 1976, pt. 2, p. L91-L94. *DOD-ERDA-supported research.*, vol. 207, pp. L91–L94, 1976.

- [101] H. Tananbaum, L. J. Chaisson, W. Forman, C. Jones, and T. Matilsky, “UHURU observations of 4U 1608-52-The steady X-ray source associated with the X-ray burst source in Norma,” *Astrophysical Journal*, vol. 209, Nov. 1, 1976, pt. 2, p. L125-L130., vol. 209, pp. L125–L130, 1976.
- [102] J. A. Hoffman, H. L. Marshall, and W. H. Lewin, “Dual character of the rapid burster and a classification of X-ray bursts,” *Nature*, vol. 271, no. 5646, pp. 630–633, 1978.
- [103] C. Iliadis, P. M. Endt, N. Prantzos, and W. J. Thompson, “Explosive hydrogen burning of ^{27}Si , ^{31}S , ^{35}Ar , and ^{39}Ca in novae and X-ray bursts,” *The Astrophysical Journal*, vol. 524, no. 1, p. 434, 1999.
- [104] J. José, F. Moreno, A. Parikh, and C. Iliadis, “Hydrodynamic models of type I X-ray bursts: metallicity effects,” *The Astrophysical Journal Supplement Series*, vol. 189, no. 1, p. 204, 2010.
- [105] J. He, P. Woods, T. Davinson, M. Aliotta, J. Büscher, E. Clement, P. Delahaye, M. Hass, D. Jenkins, V. Kumar, *et al.*, “Measurement of the inelastic branch of the $^{14}\text{O}(\alpha, p)^{17}\text{F}$ reaction: Implications for explosive burning in novae and X-ray bursters,” *Physical Review C*, vol. 80, no. 4, p. 042801, 2009.
- [106] W. Tan, J. Fisker, J. Görres, M. Couder, and M. Wiescher, “ $^{15}\text{O}(\alpha, \gamma)^{19}\text{Ne}$ Breakout Reaction and Impact on X-ray Bursts,” *Physical Review Letters*, vol. 98, no. 24, p. 242503, 2007.
- [107] P. Salter, M. Aliotta, T. Davinson, H. Al Falou, A. Chen, B. Davids, B. Fulton, N. Galinski, D. Howell, G. Lotay, *et al.*, “Measurement of the $^{18}\text{Ne}(\alpha, p_0)^{21}\text{Na}$ Reaction

- Cross Section in the Burning Energy Region for X-ray Bursts,” *Physical Review Letters*, vol. 108, no. 24, p. 242701, 2012.
- [108] K. Setoodehnia, A. A. Chen, T. Komatsubara, S. Kubono, D. N. Binh, J. F. Carpino, J. Chen, T. Hashimoto, T. Hayakawa, Y. Ishibashi, Y. Ito, D. Kahl, T. Moriguchi, H. Ooishi, A. Ozawa, T. Shizuma, Y. Sugiyama, and H. Yamaguchi, “Spins and parities of astrophysically important ^{30}S states from $^{28}\text{Si}(^3\text{He}, n\gamma)^{30}\text{S}$,” *Physical Review C*, vol. 83, p. 018803, Jan 2011.
- [109] C. Deibel, K. Rehm, J. M. Figueira, J. Greene, C. Jiang, B. Kay, H. Lee, J. Lighthall, S. Marley, R. Pardo, *et al.*, “First measurement of the $^{33}\text{Cl}(p, \alpha)^{30}\text{S}$ reaction,” *Physical Review C*, vol. 84, no. 4, p. 045802, 2011.
- [110] S. Goriely, S. Hilaire, and A. J. Koning, “Improved predictions of nuclear reaction rates with the TALYS reaction code for astrophysical applications,” *arXiv preprint arXiv:0806.2239*, 2008.
- [111] R. Clement, D. Bazin, W. Benenson, B. Brown, A. Cole, M. Cooper, P. DeYoung, A. Estrade, M. Famiano, N. Frank, *et al.*, “New approach for measuring properties of rp-process nuclei,” *Physical review letters*, vol. 92, no. 17, p. 172502, 2004.
- [112] H. Schatz, “Nuclear masses in astrophysics,” *International Journal of Mass Spectrometry*, vol. 349, pp. 181–186, 2013.
- [113] P. Schury, C. Bachelet, M. Block, G. Bollen, D. A. Davies, M. Facina, C. M. Folden III, C. Guénaut, J. Huikari, E. Kwan, A. Kwiatkowski, D. J. Morrissey, R. Ringle, G. K. Pang, A. Prinke, J. Savory, H. Schatz, S. Schwarz, C. S. Sumithrarachchi, and T. Sun,

- “Precision mass measurements of rare isotopes near $N = Z = 33$ produced by fast beam fragmentation,” *Physical Review C*, vol. 75, p. 055801, May 2007.
- [114] X. L. Tu, H. S. Xu, M. Wang, Y. H. Zhang, Y. A. Litvinov, Y. Sun, H. Schatz, X. H. Zhou, Y. J. Yuan, J. W. Xia, G. Audi, K. Blaum, C. M. Du, P. Geng, Z. G. Hu, W. X. Huang, S. L. Jin, L. X. Liu, Y. Liu, X. Ma, R. S. Mao, B. Mei, P. Shuai, Z. Y. Sun, H. Suzuki, S. W. Tang, J. S. Wang, S. T. Wang, G. Q. Xiao, X. Xu, T. Yamaguchi, Y. Yamaguchi, X. L. Yan, J. C. Yang, R. P. Ye, Y. D. Zang, H. W. Zhao, T. C. Zhao, X. Y. Zhang, and W. L. Zhan, “Direct Mass Measurements of Short-Lived $A = 2Z - 1$ Nuclides ^{63}Ge , ^{65}As , ^{67}Se , and ^{71}Kr and Their Impact on Nucleosynthesis in the rp Process,” *Physical Review Letters*, vol. 106, p. 112501, Mar 2011.
- [115] D. Rodrigues, V. S. Kolhinen, G. Audi, J. Äyöstö, D. Beck, K. Blaum, G. Bollen, F. Herfurth, A. Jokinen, A. Kellerbauer, H. J. Kluge, H. Schatz, E. Sauvan, and S. Schwarz, “Mass Measurement on the rp -process waiting point ^{72}Kr ,” *European Physical Journal A*, vol. 25 (Suppl 1), pp. 41–43, September 2005.
- [116] M. Brodeur, V. Ryjkov, T. Brunner, S. Ettenauer, A. Gallant, V. Simon, M. Smith, A. Lapierre, R. Ringle, P. Delheij, M. Good, D. Lunney, and J. Dilling, “Verifying the accuracy of the TITAN Penning-trap mass spectrometer,” *International Journal of Mass Spectrometry*, vol. 310, pp. 20–31, 2012.
- [117] E. Leistenschneider, A. Kwiatkowski, and J. Dilling, “Vacuum requirements for Penning trap mass spectrometry with highly charged ions,” *Nuclear Instruments and Methods in Physics Research Section B: Beam Interactions with Materials and Atoms*, vol. 463, pp. 496–498, 2020.

- [118] M. Yavor, “Time-of-Flight Mass Analyzers,” *Advances in Imaging and Electron Physics*, vol. 157, pp. 283–316, 2009.
- [119] W. R. Plaß, T. Dickel, and C. Scheidenberger, “Multiple-reflection time-of-flight mass spectrometry,” *International Journal of Mass Spectrometry*, vol. 349, pp. 134–144, 2013.
- [120] S. Ayet San Andrés, C. Hornung, J. Ebert, W. R. Plaß, T. Dickel, H. Geissel, C. Scheidenberger, J. Bergmann, F. Greiner, E. Haettner, C. Jesch, W. Lippert, I. Mardor, I. Miskun, Z. Patyk, S. Pietri, A. Pihktelev, S. Purushothaman, M. P. Reiter, A.-K. Rink, H. Weick, M. I. Yavor, S. Bagchi, V. Charviakova, P. Constantin, M. Diwisch, A. Finlay, S. Kaur, R. Knöbel, J. Lang, B. Mei, I. D. Moore, J.-H. Otto, I. Pohjalainen, A. Prochazka, C. Rappold, M. Takechi, Y. K. Tanaka, J. S. Winfield, and X. Xu, “High-resolution, accurate multiple-reflection time-of-flight mass spectrometry for short-lived, exotic nuclei of a few events in their ground and low-lying isomeric states,” *Physical Review C*, vol. 99, p. 064313, Jun 2019.
- [121] T. Dickel, W. Plaß, A. Becker, U. Czok, H. Geissel, E. Haettner, C. Jesch, W. Kinsel, M. Petrick, C. Scheidenberger, A. Simon, and M. Yavor, “A high-performance multiple-reflection time-of-flight mass spectrometer and isobar separator for the research with exotic nuclei,” *Nuclear Instruments and Methods in Physics Research Section A: Accelerators, Spectrometers, Detectors and Associated Equipment*, vol. 777, pp. 172–188, 2015.
- [122] B. Mamyrin, “Time-of-flight mass spectrometry (concepts, achievements, and prospects),” *International Journal of Mass Spectrometry*, vol. 206, no. 3, pp. 251–266, 2001.

-
- [123] C. Jesch, *The Multiple-Reflection Time-of-Flight Isobar Separator for TITAN and Direct Mass Measurements at the FRS Ion Catcher*. PhD thesis, Justus-Liebig-Universität Gießen, 2016.
- [124] M. I. Yavor, W. R. Plaß, T. Dickel, H. Geissel, and C. Scheidenberger, “Ion-optical design of a high-performance multiple-reflection time-of-flight mass spectrometer and isobar separator,” *International Journal of Mass Spectrometry*, vol. 381, pp. 1–9, 2015.
- [125] G. C. Ball, G. Hackman, and R. Krücken, “The TRIUMF-ISAC facility: two decades of discovery with rare isotope beams,” *Physica Scripta*, vol. 91, p. 093002, jul 2016.
- [126] I. Bylinskii and M. K. Craddock, “The TRIUMF 500 MeV Cyclotron: The Driver Accelerator,” *Hyperfine Interactions*, vol. 225, pp. 9–16, oct 2014.
- [127] M. Dombisky and P. Kunz, “ISAC Targets,” *Hyperfine Interactions*, vol. 225, pp. 17–23, oct 2014.
- [128] P. G. Bricault, F. Ames, M. Dombisky, P. Kunz, and J. Lassen, “Rare isotope beams at ISAC – target ion source systems,” *Hyperfine Interactions*, vol. 225, pp. 25–47, oct 2014.
- [129] A. Gottberg, “Target materials for exotic ISOL beams,” *Nuclear Instruments and Methods in Physics Research Section B: Beam Interactions with Materials and Atoms*, vol. 376, pp. 8–15, 2016. Proceedings of the XVIIth International Conference on Electromagnetic Isotope Separators and Related Topics (EMIS2015), Grand Rapids, MI, U.S.A., 11-15 May 2015.

- [130] F. A. M. Millán, *Comprehensive Ionization Model Development for the FEBIAD Ion Source and Its Application for TRIUMF's Radioactive Ion Beam Program*. PhD thesis, University of Victoria, 2022.
- [131] J. Lassen, P. Bricault, M. Dombisky, J. Lavoie, M. Gillner, T. Gottwald, F. Hellbusch, A. Teigelhöfer, A. Voss, and K. Wendt, "Laser ion source operation at the TRIUMF radioactive ion beam facility," in *AIP Conference Proceedings*, vol. 1104, pp. 9–15, American Institute of Physics, 2009.
- [132] S. Raeder, H. Heggen, J. Lassen, F. Ames, D. Bishop, P. Bricault, P. Kunz, A. Mjøs, and A. Teigelhöfer, "An ion guide laser ion source for isobar-suppressed rare isotope beams," *Review of Scientific Instruments*, vol. 85, no. 3, p. 033309, 2014.
- [133] C. S. of Mines, "Triumf-ISAC," n.d. Accessed January 19th, 2023. <https://electroweak.mines.edu/triumf-ISAC/>.
- [134] J. e. a. Dilling, P. Bricault, M. Smith, H.-J. Kluge, T. Collaboration, *et al.*, "The proposed TITAN facility at ISAC for very precise mass measurements on highly charged short-lived isotopes," *Nuclear Instruments and Methods in Physics Research Section B: Beam Interactions with Materials and Atoms*, vol. 204, pp. 492–496, 2003.
- [135] T. Brunner, M. Smith, M. Brodeur, S. Ettenauer, A. Gallant, V. Simon, A. Chaudhuri, A. Lapierre, E. Mané, R. Ringle, M. Simon, J. Vaz, P. Delheij, M. Good, M. Pearson, and J. Dilling, "TITAN's digital RFQ ion beam cooler and buncher, operation and performance," *Nuclear Instruments and Methods in Physics Research Section A: Accelerators, Spectrometers, Detectors and Associated Equipment*, vol. 676, pp. 32–43, 2012.

- [136] A. Lapiere, M. Brodeur, T. Brunner, S. Ettenauer, A. Gallant, V. Simon, M. Good, M. Froese, J. Crespo López-Urrutia, P. Delheij, S. Epp, R. Ringle, S. Schwarz, J. Ullrich, and J. Dilling, “The TITAN EBIT charge breeder for mass measurements on highly charged short-lived isotopes—First online operation,” *Nuclear Instruments and Methods in Physics Research Section A: Accelerators, Spectrometers, Detectors and Associated Equipment*, vol. 624, no. 1, pp. 54–64, 2010.
- [137] Y. Zhang, Y. A. Litvinov, T. Uesaka, and H. Xu, “Storage ring mass spectrometry for nuclear structure and astrophysics research,” *Physica Scripta*, vol. 91, no. 7, p. 073002, 2016.
- [138] W. R. Plaß, T. Dickel, U. Czok, H. Geissel, M. Petrick, K. Reinheimer, C. Scheidenberger, and M. I. Yavor, “Isobar separation by time-of-flight mass spectrometry for low-energy radioactive ion beam facilities,” *Nuclear Instruments and Methods in Physics Research Section B: Beam Interactions with Materials and Atoms*, vol. 266, no. 19-20, pp. 4560–4564, 2008.
- [139] P. Schury, K. Okada, S. Shchepunov, T. Sonoda, A. Takamine, M. Wada, H. Wollnik, and Y. Yamazaki, “Multi-reflection time-of-flight mass spectrograph for short-lived radioactive ions,” *The European Physical Journal A*, vol. 42, pp. 343–349, 2009.
- [140] R. N. Wolf, M. Eritt, G. Marx, and L. Schweikhard, “A multi-reflection time-of-flight mass separator for isobaric purification of radioactive ion beams,” *Hyperfine Interactions*, vol. 199, no. 1-3, pp. 115–122, 2011.
- [141] C. Izzo, J. Bergmann, K. Dietrich, E. Dunling, D. Fusco, A. Jacobs, B. Kootte, G. Kripkó-Koncz, Y. Lan, E. Leistenschneider, *et al.*, “Mass measurements of neutron-

- rich indium isotopes for r-process studies,” *Physical Review C*, vol. 103, no. 2, p. 025811, 2021.
- [142] W. Porter, B. Ashrafxhani, J. Bergmann, C. Brown, T. Brunner, J. Cardona, D. Curien, I. Dedes, T. Dickel, J. Dudek, *et al.*, “Mapping the N= 40 island of inversion: Precision mass measurements of neutron-rich Fe isotopes,” *Physical Review C*, vol. 105, no. 4, p. L041301, 2022.
- [143] M. Reiter, F. Ames, C. Andreoiu, S. A. San Andrés, C. Babcock, B. Barquest, J. Bergmann, J. Bollig, T. Brunner, T. Dickel, *et al.*, “Improved beam diagnostics and optimization at ISAC via TITAN’s MR-ToF-MS,” *Nuclear Instruments and Methods in Physics Research Section B: Beam Interactions with Materials and Atoms*, vol. 463, pp. 431–436, 2020.
- [144] D. Short, *Nuclear Isobar Separation for Penning Trap Mass Measurements at TRIUMF*. PhD thesis, Simon Fraser University, 2018.
- [145] W. R. Plaß, T. Dickel, S. A. San Andres, J. Ebert, F. Greiner, C. Hornung, C. Jesch, J. Lang, W. Lippert, T. Majoros, *et al.*, “High-performance multiple-reflection time-of-flight mass spectrometers for research with exotic nuclei and for analytical mass spectrometry,” *Physica Scripta*, vol. 2015, no. T166, p. 014069, 2015.
- [146] T. Dickel, M. I. Yavor, J. Lang, W. R. Plaß, W. Lippert, H. Geissel, and C. Scheidenberger, “Dynamical time focus shift in multiple-reflection time-of-flight mass spectrometers,” *International Journal of Mass Spectrometry*, vol. 412, pp. 1–7, 2017.

- [147] T. Dickel, W. R. Plaß, W. Lippert, J. Lang, M. I. Yavor, H. Geissel, and C. Scheidenberger, “Isobar separation in a multiple-reflection time-of-flight mass spectrometer by mass-selective re-trapping,” *Journal of The American Society for Mass Spectrometry*, vol. 28, no. 6, pp. 1079–1090, 2017.
- [148] M. Baig, M. Yaseen, R. Ali, A. Nadeem, and S. Bhatti, “Near-threshold photoionization spectra of strontium,” *Chemical physics letters*, vol. 296, no. 3-4, pp. 403–407, 1998.
- [149] J. Lassen, “Resonance ionization schemes for TITAN,”
- [150] J. Bergmann, “Entwicklung und Anwendung einer integrierten Systemsteuerung und Datenaufnahme für Flugzeitmassenspektrometer,” Master’s thesis, Justus-Liebig Universität Gießen, 2015.
- [151] S. F. Paul, “emgfit - Fitting of time-of-flight mass spectra with hyper-EMG models,” May 2022.
- [152] S. Purushothaman, S. A. San Andrés, J. Bergmann, T. Dickel, J. Ebert, H. Geissel, C. Hornung, W. Plaß, C. Rappold, C. Scheidenberger, *et al.*, “Hyper-EMG: A new probability distribution function composed of Exponentially Modified Gaussian distributions to analyze asymmetric peak shapes in high-resolution time-of-flight mass spectrometry,” *International journal of mass spectrometry*, vol. 421, pp. 245–254, 2017.
- [153] S. Purushothaman, S. A. San Andrés, J. Bergmann, T. Dickel, J. Ebert, H. Geissel, C. Hornung, W. Plaß, C. Rappold, C. Scheidenberger, *et al.*, “Hyper-EMG: A new probability distribution function composed of Exponentially Modified Gaussian distributions to analyze asymmetric peak shapes in high-resolution time-of-flight mass spectrometry,” *International journal of mass spectrometry*, vol. 421, pp. 245–254, 2017.

- [154] S. Baker and R. D. Cousins, “Clarification of the use of chi-square and likelihood functions in fits to histograms,” *Nuclear Instruments and Methods in Physics Research*, vol. 221, no. 2, pp. 437–442, 1984.
- [155] G. F. Knoll, *Radiation detection and measurement*. John Wiley & Sons, 2010.
- [156] A. Jacobs, *Refinement of the first r-process abundance peak via high-precision mass measurements*. PhD thesis, The University of British Columbia, 2023.
- [157] S. F. Paul, *Precision mass measurements for the astrophysical rp-process and electron cooling of trapped ions*. PhD thesis, Heidelberg University, 2023.
- [158] M. Wang, W. Huang, F. G. Kondev, G. Audi, and S. Naimi, “The AME 2020 atomic mass evaluation (II). Tables, graphs and references,” *Chinese Physics C*, vol. 45, no. 3, p. 030003, 2021.
- [159] M. Wang, Y. H. Zhang, X. Zhou, X. H. Zhou, H. S. Xu, M. L. Liu, J. G. Li, Y. F. Niu, W. J. Huang, Q. Yuan, S. Zhang, F. R. Xu, Y. A. Litvinov, K. Blaum, *et al.*, “Mass measurement of upper fp -Shell $N = Z - 2$ and $N = Z - 1$ nuclei and the importance of three-nucleon force along the $N = Z$ line,” *Physical Review Letters*, vol. 130, p. 192501, May 2023.
- [160] G. Sikler, G. Audi, D. Beck, K. Blaum, G. Bollen, F. Herfurth, A. Kellerbauer, H.-J. Kluge, D. Lunney, M. Oinonen, *et al.*, “Mass measurements on neutron-deficient Sr and neutron-rich Sn isotopes with the ISOLTRAP mass spectrometer,” *Nuclear Physics A*, vol. 763, pp. 45–58, 2005.

- [161] J. Huikari, M. Oinonen, A. Algora, J. Cederkäll, S. Courtin, P. Dessagne, L. Fraile, S. Franchoo, H. Fynbo, W. Huang, *et al.*, “Mirror decay of ^{75}Sr ,” *The European Physical Journal A-Hadrons and Nuclei*, vol. 16, no. 3, pp. 359–363, 2003.
- [162] Y. A. Litvinov, H. Geissel, T. Radon, F. Attallah, G. Audi, K. Beckert, F. Bosch, M. Falch, B. Franzke, M. Hausmann, *et al.*, “Mass measurement of cooled neutron-deficient bismuth projectile fragments with time-resolved Schottky mass spectrometry at the FRS-ESR facility,” *Nuclear Physics A*, vol. 756, no. 1-2, pp. 3–38, 2005.
- [163] C. Rauth, D. Ackermann, G. Audi, M. Block, A. Chaudhuri, S. Eliseev, F. Herfurth, F. Hessberger, S. Hofmann, H.-J. Kluge, *et al.*, “Direct mass measurements around $A = 146$ at SHIPTRAP,” *The European Physical Journal Special Topics*, vol. 150, no. 1, pp. 329–335, 2007.
- [164] K. S. Toth, D. C. Sousa, J. M. Nitschke, K. S. Vierinen, and P. A. Wilmarth, “Identification of the $s_{1/2}$ ^{145}Dy ground state,” *Physical Review C*, vol. 48, pp. 436–438, Jul 1993.
- [165] G. Alkhazov, K. Mezilev, Y. N. Novikov, V. Panteleyev, A. Polyakov, V. Afanasyev, N. Ganbaatar, K. Y. Gromov, V. Kalinnikov, J. Kormicki, *et al.*, “New neutron deficient isotopes with mass numbers $a = 136$ and 145,” *Zeitschrift für Physik A Atoms and Nuclei*, vol. 305, no. 2, pp. 185–186, 1982.
- [166] E. Nolte, S. Gui, G. Colombo, G. Korschinek, and K. Eskola, “Very proton rich nuclei with $N \approx 82$,” *Zeitschrift für Physik A Atoms and Nuclei*, vol. 306, no. 3, pp. 223–234, 1982.

- [167] F. Kondev, M. Wang, W. Huang, S. Naimi, and G. Audi, “The NUBASE2020 evaluation of nuclear physics properties,” *Chinese Physics C*, vol. 45, no. 3, p. 030001, 2021.
- [168] G. Audi, O. Bersillon, J. Blachot, and A. H. Wapstra, “The NUBASE evaluation of nuclear and decay properties,” *Nuclear physics A*, vol. 729, no. 1, pp. 3–128, 2003.
- [169] A. E. Barzakh, D. V. Fedorov, A. M. Ionan, V. S. Ivanov, F. V. Moroz, K. A. Mezilev, S. Y. Orlov, V. N. Panteleev, and Y. M. Volkov, “Laser spectroscopic studies of ^{145}Gd , $^{145}\text{Gd}^m$, and $^{143}\text{Gd}^m$,” *Physical Review C*, vol. 72, p. 017301, Jul 2005.
- [170] R. Broda, Y. Chung, P. Daly, Z. Grabowski, J. McNeill, R. Janssens, and D. Radford, “ $(\pi h_{11/2} \nu h_{11/2}^{-1})10^+$ isomers in $N = 81$ nuclei ^{146}Tb , ^{148}Ho , and ^{150}Tm ,” *Zeitschrift für Physik A Atoms and Nuclei*, vol. 316, no. 1, pp. 125–126, 1984.
- [171] R. Broda, P. Daly, J. McNeill, Z. Grabowski, R. Janssens, R. Lawson, and D. Radford, “Decays of millisecond isomers in odd-odd $N = 81$ nuclei ^{146}Tb , ^{148}Ho and ^{150}Tm ,” *Zeitschrift für Physik A Atomic Nuclei*, vol. 334, no. 1, pp. 11–17, 1989.
- [172] J. Kownacki, C. Droste, T. Morek, E. Ruchowska, R. M. Lieder, M. Kisieliński, M. Kowalczyk, J. Andrzejewski, J. Perkowski, P. J. Napiorkowski, K. Wrzosek-Lipska, M. Zielińska, A. Kordyasz, A. Korman, K. Hadyńska-Klek, E. Grodner, J. Mierzejewski, and J. Srebrny, “Decay properties of long-lived isomers in the odd-odd $N = 81$ nucleus ^{146}Tb compared to the ^{148}Ho and ^{150}Tm nuclei,” *Physical Review C*, vol. 83, p. 027301, Feb 2011.

- [173] C. Xie, X. Zhou, Y. Zheng, Y. Zhang, Z. Liu, Z. Gan, T. Hayakawa, M. Oshima, T. Toh, T. Shizuma, *et al.*, “Level structure of ^{146}Tb ,” *The European Physical Journal A-Hadrons and Nuclei*, vol. 19, no. 1, pp. 7–9, 2004.
- [174] R. Collatz, N. Amzal, Z. Meliani, C. Schück, C. Vieu, J. Dionisio, P. Kleinheinz, and J. Blomqvist, “Yrast states in the π -particle ν -hole nucleus $^{146}_{65}\text{Tb}_{81}$,” *Zeitschrift für Physik A Hadrons and Nuclei*, vol. 359, no. 2, pp. 113–114, 1997.
- [175] G. Audi, F. Kondev, M. Wang, B. Pfeiffer, X. Sun, J. Blachot, and M. MacCormick, “The NUBASE2012 evaluation of nuclear properties,” *Chinese Physics C*, vol. 36, no. 12, p. 1157, 2012.
- [176] M. Newville, R. Otten, A. Nelson, T. Stensitzki, A. Ingargiola, D. Allan, A. Fox, F. Carter, Michał, R. Osborn, D. Pustakhod, Ineuhaus, S. Weigand, A. Aristov, Glenn, C. Deil, mgunyho, Mark, A. L. R. Hansen, G. Pasquevich, L. Foks, N. Zobrist, O. Frost, Stuermer, azelcer, A. Polloreno, A. Persaud, J. H. Nielsen, M. Pompili, and P. Eendebak, “lmfit/lmfit-py: 1.2.2,” July 2023.
- [177] W. Satuła, P. Baczyk, J. Dobaczewski, and M. Konieczka, “No-core configuration-interaction model for the isospin-and angular-momentum-projected states,” *Physical Review C*, vol. 94, no. 2, p. 024306, 2016.
- [178] M. S. Martin, S. R. Stroberg, J. D. Holt, and K. G. Leach, “Testing isospin symmetry breaking in ab initio nuclear theory,” *Phys. Rev. C*, vol. 104, p. 014324, Jul 2021.
- [179] J. Simonis, S. R. Stroberg, K. Hebeler, J. D. Holt, and A. Schwenk, “Saturation with chiral interactions and consequences for finite nuclei,” *Physical Review C*, vol. 96, no. 1, p. 014303, 2017.

- [180] A. Ekström, G. R. Jansen, K. A. Wendt, G. Hagen, T. Papenbrock, B. D. Carlsson, C. Forssén, M. Hjorth-Jensen, P. Navrátil, and W. Nazarewicz, “Accurate nuclear radii and binding energies from a chiral interaction,” *Physical Review C*, vol. 91, p. 051301(R), 2015.
- [181] A. J. Koning, S. Hilaire, and M. C. Duijvestijn, “TALYS-1.0,” in *International Conference on Nuclear Data for Science and Technology*, pp. 211–214, EDP Sciences, 2007.
- [182] D. E. M. Hoff, A. M. Rogers, Z. Meisel, P. C. Bender, K. Brandenburg, K. Childers, J. A. Clark, A. C. Dombos, E. R. Doucet, S. Jin, R. Lewis, S. N. Liddick, C. J. Lister, C. Morse, H. Schatz, K. Schmidt, D. Soltesz, S. K. Subedi, S. M. Wang, and S. Waniganeththi, “Influence of ^{73}Rb on the ashes of accreting neutron stars,” *Physical Review C*, vol. 102, p. 045810, Oct 2020.
- [183] A. S. Hamaker, *Mass measurement of the lightweight self-conjugate nucleus zirconium-80 and the development of the single ion penning trap*. PhD thesis, Michigan State University, 2021.
- [184] K. Blaum, S. Eliseev, and S. Sturm, “Perspectives on testing fundamental physics with highly charged ions in Penning traps,” *Quantum Science and Technology*, vol. 6, no. 1, p. 014002, 2020.
- [185] J. D. Gillaspay, “Highly charged ions,” *Journal of Physics B: Atomic, Molecular and Optical Physics*, vol. 34, no. 19, p. R93, 2001.

- [186] M. Safronova, D. Budker, D. DeMille, D. F. J. Kimball, A. Derevianko, and C. W. Clark, “Search for new physics with atoms and molecules,” *Reviews of Modern Physics*, vol. 90, no. 2, p. 025008, 2018.
- [187] S. A. King, L. J. Spieß, P. Micke, A. Wilzewski, T. Leopold, E. Benkler, R. Lange, N. Huntemann, A. Surzhykov, V. A. Yerokhin, *et al.*, “An optical atomic clock based on a highly charged ion,” *Nature*, vol. 611, no. 7934, pp. 43–47, 2022.
- [188] F. S. Porter, G. V. Brown, K. R. Boyce, R. L. Kelley, C. A. Kilbourne, P. Beiersdorfer, H. Chen, S. Terracol, S. M. Kahn, and A. E. Szymkowiak, “The Astro-E2 X-ray spectrometer/EBIT microcalorimeter X-ray spectrometer,” *Review of Scientific Instruments*, vol. 75, no. 10, pp. 3772–3774, 2004.
- [189] S. Bernitt, G. Brown, J. K. Rudolph, R. Steinbrügge, A. Graf, M. Leutenegger, S. Epp, S. Eberle, K. Kubiček, V. Mäckel, *et al.*, “An unexpectedly low oscillator strength as the origin of the Fe XVII emission problem,” *Nature*, vol. 492, no. 7428, pp. 225–228, 2012.
- [190] I. Bergström, C. Carlberg, T. Fritioff, G. Douysset, J. Schönfelder, and R. Schuch, “SMILETRAP—A Penning trap facility for precision mass measurements using highly charged ions,” *Nuclear Instruments and Methods in Physics Research Section A: Accelerators, Spectrometers, Detectors and Associated Equipment*, vol. 487, no. 3, pp. 618–651, 2002.
- [191] S. Ettenauer, M. Simon, A. Gallant, T. Brunner, U. Chowdhury, V. Simon, M. Brodeur, A. Chaudhuri, E. Mané, C. Andreoiu, *et al.*, “First use of high charge states for mass measurements of short-lived nuclides in a Penning trap,” *Physical Review Letters*, vol. 107, no. 27, p. 272501, 2011.

- [192] Y. A. Litvinov, F. Bosch, H. Geissel, J. Kurcewicz, Z. Patyk, N. Winckler, L. Batist, K. Beckert, D. Boutin, C. Brandau, *et al.*, “Measurement of the $\beta+$ and Orbital Electron-Capture Decay Rates in Fully Ionized, Hydrogen-like, and Helium-like ^{140}Pr Ions,” *Physical Review Letters*, vol. 99, no. 26, p. 262501, 2007.
- [193] F. Bosch, “Beta decay of highly charged ions,” in *TCP 2006: Proceedings of the 4th International Conference on Trapped Charged Particles and Fundamental Physics (TCP 2006) held in Parksville, Canada, 3–8 September, 2006*, pp. 157–167, Springer, 2007.
- [194] A. V. Gruzinov and J. N. Bahcall, “The ^7Be electron capture rate in the sun,” *The Astrophysical Journal*, vol. 490, no. 1, p. 437, 1997.
- [195] D. Atanasov, K. Blaum, F. Bosch, C. Brandau, P. Bühler, X. Chen, I. Dillmann, T. Faestermann, B. Gao, H. Geissel, R. Gernhäuser, S. Hagmann, T. Izumikawa, P.-M. Hillenbrand, C. Kozhuharov, J. Kurcewicz, S. A. Litvinov, Y. A. Litvinov, X. Ma, G. Münzenberg, M. A. Najafi, F. Nolden, T. Ohtsubo, A. Ozawa, F. C. Ozturk, Z. Patyk, M. Reed, R. Reifarth, M. S. Sanjari, D. Schneider, M. Steck, T. Stöhlker, B. Sun, F. Suzaki, T. Suzuki, C. Trageser, X. Tu, T. Uesaka, P. Walker, M. Wang, H. Weick, N. Winckler, P. Woods, H. Xu, T. Yamaguchi, X. Yan, Y. Zhang, S. for the FRS-ESR, ILIMA, and T. Collaborations, “Between atomic and nuclear physics: radioactive decays of highly-charged ions,” *Journal of Physics B: Atomic, Molecular and Optical Physics*, vol. 48, p. 144024, may 2015.
- [196] F. Wenander, “Charge breeding of radioactive ions with EBIS and EBIT,” *Journal of Instrumentation*, vol. 5, no. 10, p. C10004, 2010.

- [197] W. Lotz, “An empirical formula for the electron-impact ionization cross-section,” *Zeitschrift für Physik*, vol. 206, no. 2, pp. 205–211, 1967.
- [198] E. Donets, “The electron beam method of production of highly charged ions and its applications,” *Physica Scripta*, vol. 1983, no. T3, p. 11, 1983.
- [199] L. M. J. Dilling, R. Krücken, *ISAC and ARIEL: The TRIUMF Radioactive Beam Facilities and the Scientific Program*. Springer Dordrecht, 1 ed., 2014.
- [200] A. Lapierre, “Electron-beam ion source/trap charge breeders at rare-isotope beam facilities,” *Review of Scientific Instruments*, vol. 90, no. 10, 2019.
- [201] F. Wenander, “Charge breeding techniques,” *Nuclear Physics A*, vol. 746, pp. 40–46, 2004.
- [202] R. Marrs, “Milestones in EBIT spectroscopy and why it almost did not work,” *Canadian Journal of Physics*, vol. 86, no. 1, pp. 11–18, 2008.
- [203] J. C. López-Urrutia, J. Braun, G. Brenner, H. Bruhns, C. Dimopoulou, I. Draganić, D. Fischer, A. G. Martínez, A. Lapierre, V. Mironov, *et al.*, “Progress at the Heidelberg EBIT,” in *Journal of Physics: Conference Series*, vol. 2, p. 006, IOP Publishing, 2004.
- [204] A. G. Martínez, J. C. López-Urrutia, D. Fischer, R. S. Orts, and J. Ullrich, “The Heidelberg EBIT: Present results and future perspectives,” in *Journal of Physics: Conference Series*, vol. 72, p. 012001, IOP Publishing, 2007.
- [205] M. Froese, C. Champagne, J. Crespo López-Urrutia, S. Epp, G. Gwinner, A. Lapierre, J. Pfister, G. Sikler, J. Ullrich, and J. Dilling, “A high-current electron beam ion trap as an on-line charge breeder for the high precision mass measurement TITAN experiment,” *Hyperfine Interactions*, vol. 173, pp. 85–92, 2006.

- [206] X. Lu and F. Currell, “Numerical simulation of the charge balance and temperature evolution in an electron beam ion trap,” *Physical Review Special Topics-Accelerators and Beams*, vol. 12, no. 1, p. 014401, 2009.
- [207] J. Pierce, “Rectilinear electron flow in beams,” *Journal of applied physics*, vol. 11, no. 8, pp. 548–554, 1940.
- [208] G. Herrmann, “Optical theory of thermal velocity effects in cylindrical electron beams,” *Journal of Applied Physics*, vol. 29, no. 2, pp. 127–136, 1958.
- [209] A. Lennarz, *In-trap decay spectroscopy on highly-charged radioactive ions towards measurements on intermediate nuclei in $\beta\beta$ decay*. PhD thesis, Westfälischen Wilhelms-Universität Münster, 2015.
- [210] K. G. Leach, I. Dillmann, R. Klawitter, E. Leistenschneider, A. Lennarz, T. Brunner, D. Frekers, C. Andreoiu, A. A. Kwiatkowski, and J. Dilling, “Electroweak decay studies of highly charged radioactive ions with TITAN at TRIUMF,” *Atoms*, vol. 5, no. 1, p. 14, 2017.
- [211] F. Currell and G. Fussmann, “Physics of electron beam ion traps and sources,” *IEEE Transactions on Plasma Science*, vol. 33, no. 6, pp. 1763–1777, 2005.
- [212] Z. Ke, W. Shi, G. Gwinner, K. Sharma, S. Toews, J. Dilling, and V. Ryjkov, “A cooler ion trap for the TITAN on-line trapping facility at TRIUMF,” in *TCP 2006: Proceedings of the 4th International Conference on Trapped Charged Particles and Fundamental Physics (TCP 2006) held in Parksville, Canada, 3–8 September, 2006*, pp. 259–267, Springer, 2007.

- [213] T. Brunner, M. Brodeur, S. Ettenauer, A. Gallant, R. Gernhäuser, A. Lapierre, R. Ringle, S. Sjøe, P. Delheij, D. Frekers, *et al.*, “Design of a β -detector for TITAN-EC and the first electron-capture branching ratio measurement in a Penning trap,” in *Journal of Physics: Conference Series*, vol. 312, p. 072006, IOP Publishing, 2011.
- [214] A. Lennarz, A. Grossheim, K. Leach, M. Alanssari, T. Brunner, A. Chaudhuri, U. Chowdhury, J. C. López-Urrutia, A. Gallant, M. Holl, *et al.*, “In-trap spectroscopy of charge-bred radioactive ions,” *Physical Review Letters*, vol. 113, no. 8, p. 082502, 2014.
- [215] T. Brunner, M. Brodeur, C. Champagne, D. Frekers, R. Krücken, A. Lapierre, P. Delheij, R. Ringle, V. Ryjkov, M. Smith, *et al.*, “Electron capture branching ratio measurements in an ion trap for double beta decay experiments at TITAN,” *Nuclear Instruments and Methods in Physics Research Section B: Beam Interactions with Materials and Atoms*, vol. 266, no. 19-20, pp. 4643–4646, 2008.
- [216] K. Leach, A. Grossheim, A. Lennarz, T. Brunner, J. Crespo López-Urrutia, A. Gallant, M. Good, R. Klawitter, A. Kwiatkowski, T. Ma, T. Macdonald, S. Seeraji, M. Simon, C. Andreoiu, J. Dilling, and D. Frekers, “The TITAN in-trap decay spectroscopy facility at TRIUMF,” *Nuclear Instruments and Methods in Physics Research Section A: Accelerators, Spectrometers, Detectors and Associated Equipment*, vol. 780, pp. 91–99, 2015.
- [217] M. Rosenbusch, D. Atanasov, K. Blaum, C. Borgmann, S. Kreim, D. Lunney, V. Manea, L. Schweikhard, F. Wienholtz, and R. N. Wolf, “Ion bunch stacking in a Penning trap after purification in an electrostatic mirror trap,” *Applied Physics B*, vol. 114, pp. 147–155, 2014.

- [218] A. Garnsworthy, “Exotic nuclei studied with the 8pi spectrometer at TRIUMF,” in *EPJ Web of Conferences*, vol. 93, p. 01032, EDP Sciences, 2015.
- [219] “Experimental Physics and Industrial Control System,” 2023.
- [220] Mesytec, *MDPP-16 SCP/RCP Datasheet*. Mesytec GmbH Co. KG.
- [221] A. Garnsworthy, C. Pearson, D. Bishop, B. Shaw, J. Smith, M. Bowry, V. Bildstein, G. Hackman, P. Garrett, Y. Linn, *et al.*, “The GRIFFIN data acquisition system,” *Nuclear Instruments and Methods in Physics Research Section A: Accelerators, Spectrometers, Detectors and Associated Equipment*, vol. 853, pp. 85–104, 2017.
- [222] S. Ritt, P. Amaudruz, and K. Olchanski, “The MIDAS data acquisition system,” in *Proc. ieee 10th real time conf*, pp. 309–312, 1997.
- [223] J. Ringuette, *Towards nuclear excitation via electron capture in an electron beam ion trap*. PhD thesis, Colorado School of Mines, 2022.
- [224] Ortec, *GMX Series Coaxial HPGe Detector Product Configuration Guide*. Ortec.
- [225] M. Blessenohl, S. Dobrodey, C. Warnecke, M. Rosner, L. Graham, S. Paul, T. Baumann, Z. Hockenbery, R. Hubele, T. Pfeifer, *et al.*, “An electron beam ion trap and source for re-acceleration of rare-isotope ion beams at TRIUMF,” *Review of Scientific Instruments*, vol. 89, no. 5, 2018.
- [226] A. J. Smith, P. Beiersdorfer, K. Widmann, M. H. Chen, and J. H. Scofield, “Measurement of resonant strengths for dielectronic recombination in heliumlike Ar^{16+} ,” *Phys. Rev. A*, vol. 62, p. 052717, Oct 2000.

-
- [227] M. Antony and J.-B. Bueb, “Mass excess of ^{69}Br and the rp process,” *Chinese Physics C*, vol. 39, no. 9, p. 094103, 2015.